Modeling of radiative transfer through a spherical planetary atmosphere:

Application to atmospheric trace gases retrieval from occultation- and limb-measurements in UV–Vis–NIR

Dissertation
zur Erlangung des Grades Dr. rer. nat.
am Fachbereich Physik der Universität Bremen

vorgelegt von

Dipl. Phys. Alexei Rozanov

Institut für Umweltphysik
Universität Bremen

Tag des öffentlichen Kolloquiums	28. August 2001
Gutachter der Dissertation	Prof. Dr. J. P. Burrows Prof. Dr. J. Bleck-Neuhaus
weitere Prüfer	Prof. Dr. K. F. Künzi Prof. Dr. P. Richter

Contents

Objectives

During the last years and decades issues related to the physics and chemistry of the Earth's atmosphere have attracted much scientific and public interest. The most important problems are (i) stratospheric ozone loss and the "ozone hole" above Antarctica, (ii) global warming and climate change, and (iii) tropospheric air pollution.

The understanding of the impact of human activities on the Earth's atmosphere requires measurements on a global scale. These enable the spatial and temporal variability of the atmospheric constituents to be investigated.

Recently efforts have been made to establish a global observation system comprising satellite instruments and ground-based networks. In order to process data supplied by the instruments which belong to the global observation system, the development of radiative transfer models and retrieval algorithms is essential.

This thesis contributes to the development of the radiative transfer models and retrieval algorithms intended to interprete measurements of the spectral radiance scattered in the atmosphere or transmitted through the atmosphere in the ultra-violet, visible, and near-infrared spectral regions performed by a new-generation remote sensing satellite spectrometer SCIAMACHY. The objectives of this study are

- the investigation of radiative transfer through a spherical planetary atmosphere,
- the development and following validation of an efficient spherical radiative transfer model intended to simulate SCIAMACHY limb measurements,
- the development of an approximate approach allowing the simulation of limb measurements to be substantially accelerated and the investigation of the accuracy of this approach,
- the development of a numerical radiative transfer model intended to simulate SCIAMACHY occultation measurements,
- the development of a retrieval code (software package) for the interpretation of SCIAMACHY occultation measurements coupling the radiative transfer model with an appropriate selected inverse technique.

Introduction

In recent years, significant changes in the composition and behavior of the Earth's atmosphere have been reported. Most important of these are the stratospheric ozone loss in Arctic and Antarctic regions [*WMO*, 1995; *Newman et al.*, 1997; *Müller et al.*, 1997], the global increase of the tropospheric ozone [*WMO*, 1995], and the increase of tropospheric "greenhouse gases" such as CO_2, CH_4, and N_2O [*IPCC*, 1996]. In order to study these changes, systematic information on the global distribution of atmospheric constituents and its seasonal variations is required. Such information also enables the potential coupling between polar stratospheric ozone loss and increasing greenhouse gas concentrations reported by *Shindell et al.* [1998] to be investigated.

Remote sensing of the Earth's atmosphere in the UV–Vis–NIR spectral region by means of ground-based and space-borne instruments can yield important information on the temporal and spatial behavior of several atmospheric constituents (trace gases, aerosol, clouds) on a global scale. The abundance of atmospheric trace gases in the stratosphere and the troposphere as well as the stratospheric-tropospheric exchange can be investigated using such measurements. Over the past two decades pioneering efforts have been made by the scientific community to establish both ground-based networks and satellite projects that will eventually result in an adequate global observation system.

The Solar Backscatter Ultraviolet (SBUV) [*Heath et al.*, 1975; *Fleig et al.*, 1990] and Total Ozone Mapping Spectrometer (TOMS) [*Heath et al.*, 1975; *McPeters et al.*, 1996] were launched on board NASA's Nimbus-7 satellite in October 1978. SBUV observed in the nadir direction with a field of view of $11.3° \times 11.3°$ and measured the backscattered ultraviolet solar radiation either in 12 wavelength channels with center wavelengths in spectral range 255.65 – 339.89 nm or scanned continuously from 160 nm to 400 nm, whereas TOMS measured the backscattered ultraviolet solar radiation in 6 wavelength channels, namely, 312.51, 317.51, 331.25, 339.86, 359.96, and 380.01 nm, scanning in 3° steps from nadir to 51° on each side of the sub-satellite point in a direction perpendicular to the orbital plane.

The Stratospheric Aerosol and Gas Experiment (SAGE) [*McCormick et al.*, 1979, 1984] launched on board the Applications Explorer Mission-2 (AEM-2) satellite and SAGE-II [*Mauldin et al.*, 1985] launched on board the Earth Radiation Budget Satellite (ERBS) (both NASA's satellites) were designed to monitor globally the vertical distribution of stratospheric aerosols, ozone, water vapor (SAGE-II only), and nitrogen dioxide by measuring the solar radiation transmitted through the Earth's atmosphere during the solar occultations. SAGE is a four-channel instrument with center wavelengths at 1000 nm, 600

nm, 450 nm, and 385 nm. SAGE-II is a seven-channel instrument with center wavelengths at 1020, 940, 600, 525, 453, 448, and 385 nm.

NASA's Solar Mesosphere Explorer (SME) [*Mount et al.*, 1984] satellite was launched in October 1981. One of the instruments on board SME was a visible spectrometer that observed the solar radiance scattered in the Earth's atmosphere in limb viewing geometry. The measurements were performed in a spectral range from 312.6 to 647.2 nm. One of the most important products deduced from the SME observations was NO_2 vertical distribution in the altitude range from 24 to 40 km.

The Global Ozone Monitoring Experiment (GOME) [*Burrows et al.*, 1999] was launched on board the European Space Agency's (ESA) Second European Remote Sensing (ERS-2) satellite in April 1995. The main scientific objective of the GOME mission is to determine the global distribution of ozone and several other trace gases which play an important role in the ozone chemistry of the Earth's stratosphere and troposphere such as NO_2, BrO, ClO, SO_2, and OClO. The GOME instrument measures the sunlight scattered in the Earth's atmosphere and reflected by the surface in nadir viewing mode in the spectral region 240–790 nm.

In the near future, several new missions will be launched which will contribute significantly to research in the fields of atmospheric chemistry and physics. Some examples of such missions and a short description of their capabilities follow.

The Global Ozone Monitoring by Occultation of Stars (GOMOS) instrument [*Popescu and Paulsen*, 1999] and the Scanning Imaging Absorption Spectrometer for Atmospheric Chartography (SCIAMACHY) are parts of the atmospheric chemistry payload on board ESA's Environmental Satellite (ENVISAT) which is planned to be launched in 2001. The GOMOS instrument is designed to monitor trends in the stratospheric ozone with very high accuracy and to observe several other atmospheric trace gases using the star occultation technique. The GOMOS instrument will measure the stellar light transmitted through the atmosphere in the spectral range 250–952 nm. During the day-side observations, measurements of the solar radiation scattered in the atmosphere in limb viewing geometry will also be performed in order to remove the background term from the stellar occultation signal. The SCIAMACHY instrument is designed to measure the sunlight which is transmitted, reflected and scattered by the Earth's atmosphere or surface in the wavelength region from 240 to 2380 nm. Limb, nadir, and occultation measurements are planned to be made during every orbit. The instrument is discussed in detail in Chapter 2.

Similar to the SCIAMACHY instrument, the Optical Spectrograph and InfraRed Imaging System (OSIRIS) [*Llewellyn et al.*, 1997], which was launched on board the Swedish satellite ODIN in February 2001, measures scattered solar radiance in limb viewing geometry in the spectral region from 280 nm to 800 nm. In addition, the atmospheric emission features (airglow) in the wavelength range 280 – 800 nm and at particular wavelengths near 1270 nm and 1520 nm are intended to be measured by the OSIRIS instrument.

Another important component of the global observation system is its network of ground-based instruments. The data supplied by these instruments are of great importance for the investigation of the diurnal and seasonal variations in atmospheric trace gas abundances as well as for the validation of the satellite measurements. The commonly used technique to

obtain the total column abundances of the atmospheric trace gases, such as O_3, NO_2, BrO, OClO, etc., from ground-based measurements are the twilight observations of the zenith-sky radiance. Examples of such observations and details on the measurement technique can be found in [*Noxon*, 1975; *Harrison*, 1979; *Mount et al.*, 1987; *Sanders et al.*, 1989; *Johnson et al.*, 1992; *Muthama et al.*, 1995; *Richter et al.*, 1999]. Recently near simultaneous zenith-sky and off-axis measurements, see, for example, [*Wittrock et al.*, 1999], have also been carried out in order to obtain information about the tropospheric abundances of atmospheric trace gases. Performing such observations, the instrument line-of-sight points several degrees above the horizon and the light scattered in the atmosphere is measured. This method will be discussed in more detail in Section 8.2.

For the interpretation of satellite and ground-based measurements, complex and precise radiation transfer models and retrieval algorithms are required. The simplest to interprete are the occultation measurements as performed by SAGE, SAGE-II, GOMOS (stellar occultation mode) and SCIAMACHY (solar/lunar occultation mode). Radiative transfer models for the occultation geometry are based on the Lambert-Beer law and the weighting functions can be analytically derived, see, for example, [*Chu and McCormic*, 1979]. A detailed discussion of such a model can be found in Section 5.1 where a radiative transfer model and a retrieval algorithm developed to retrieve the vertical distributions of the atmospheric trace gases from SCIAMACHY occultation measurements are discussed.

As shown in [*Klenk et al.*, 1982; *McPeters et al.*, 1996; *Hoogen et al.*, 1999], satellite measurements of the backscattered solar radiation in nadir viewing geometry, as performed by SBUV, GOME, and SCIAMACHY (nadir mode), can be accurately simulated using a pseudo-spherical radiative transfer model such as DISORT [*Stamnes et al.*, 1988] and SCIATRAN [*Rozanov et al.*, 2000b]. However, the pseudo-spherical approximation is not accurate enough for large viewing and solar zenith angles [*Caudill et al.*, 1997], as occurs, for example, in a TOMS scan. In limb viewing geometry, as shown in [*Rozanov et al.*, 1999a], pseudo-spherical radiative transfer models produce absolutely wrong results. Thus, they are not appropriate to simulate limb measurements, as performed by SME, GOMOS (background term), SCIAMACHY (limb mode), and OSIRIS. The radiative transfer models commonly used for the interpretation of such measurements require an accurate calculation of the single scattering term and any approximation for the multiple scattering term, see, for example, [*Naudet and Thomas*, 1987; *Anderson and Lloyd*, 1990; *McLinden et al.*, 1999; *Abreu et al.*, 1989]. However, the accuracies of the radiative transfer models used in these studies have not been investigated and reported. Another example of such an approximative model and the investigation of its accuracy in limb viewing geometry is found in Section 7.5.

In order to obtain the total column abundances of the atmospheric constituents from ground-based zenith-sky measurements, air mass factors have to be calculated using an appropriate radiative transfer model, see, for example, [*Solomon et al.*, 1987]. Air mass factors are commonly calculated using either a single scattering [*Mount et al.*, 1987] or a pseudo-spherical radiative transfer model [*Ridley et al.*, 1984]. However, under certain conditions, see, for example, Section 8.3 or [*Slusser et al.*, 1996], a spherical radiative

transfer model is required to derive the trace gas vertical column abundances accurately enough.

Thus, for the interpretation of the off-nadir, limb, and ground-based measurements, an accurate radiative transfer model is required, which takes into account the spherical shape of the atmosphere both for single and multiple scattering. A newly developed spherical radiative transfer model which meets these requirements is described in Section 7. Although the model was developed to simulate SCIAMACHY limb measurements, it can also be used for the interpretation of measurements performed by GOMOS and OSIRIS as well as to compute air mass factors for ground-based measurements.

The main objectives of this study can be summarized as follows. A radiative transfer model and a retrieval algorithm intended to interprete SCIAMACHY occultation measurements has been developed. The radiative transfer model is able to simulate solar radiation transmitted through the atmosphere in the entire spectral range covered by the SCIAMACHY instrument (240 – 2380 nm). Due to an appropriate selection of the retrieval algorithm, a series of occultation measurements at various tangent heights in various spectral windows can be interpreted simultaneously. Furthermore, an appropriate method to solve the radiative transfer equation in a spherical planetary atmosphere has been selected. Based on this method, a fully spherical radiative transfer model to simulate SCIAMACHY limb measurements has been developed. The model has been validated and improved to achieve maximum computational efficiency. Possible approximations which can be employed to accelerate forward modeling in a spherical planetary atmosphere have been analyzed.

Part I

General considerations

Chapter 1

Relevant aspects of the atmospheric physics and chemistry

1.1 Stratospheric ozone

1.1.1 The role of ozone in the atmosphere

Ozone plays an extremely important role in the Earth's atmosphere absorbing virtually all solar ultraviolet radiation in the spectral range 240 - 290 nm, which damages simple unicellural organisms and surface cells of higher plants and animals. Of prime scientific importance too is the fact that upper atmospheric meteorology is greatly influenced by the heating that results from absorption by ozone of UV, visible, and thermal radiation. The stratosphere is a consequence of this heating and the height of the tropopause plays an important role in determining the weather and climate of the troposphere.

The scientific interest to the identification of the factors that control ozone concentrations was stimulated by the recognition of declining amounts of the stratospheric ozone over past decades and the dramatic depletions of ozone over the Antarctic as well as concern that a variety of human influences might lead to detectable changes in the abundance of stratospheric ozone.

1.1.2 Oxygen-only chemistry

A photo-chemical theory for formation and destruction of ozone based on an oxygen-only chemical scheme was first proposed by *Chapman* [1930]. The reactions in the Chapman's scheme were

$$O_2 + h\nu \xrightarrow{\lambda < 214 \text{ nm}} 2O \tag{1.1}$$

$$O + O_2 + M \longrightarrow O_3 + M \tag{1.2}$$

$$O_3 + h\nu \xrightarrow{\lambda < 310 \text{ nm}} O + O_2 \tag{1.3}$$

$$O + O_3 \longrightarrow 2O_2 \tag{1.4}$$

$$O + O + M \longrightarrow O_2 + M \tag{1.5}$$

In the intervening years reaction (1.5) was shown to be too slow for it to play a part in stratospheric chemistry. Both photolytic reactions (1.1) and (1.3) can also yield exited fragments, but collisional deactivation to $O(^3P)$ is the almost exclusive fate of any $O(^1D)$ formed in the upper atmosphere.

Ozone photolysis below $\sim$ 50 km (reaction (1.3)) represents a gross but not net loss process over timescales of the order of minutes of more, since nearly all of the atomic oxygen thus produced reforms ozone through the reaction (1.2) in a few seconds or less. Ozone and atomic oxygen thereby cycle very rapidly between one another in the stratosphere. A small fraction of the oxygen atoms produced from ozone photolysis can react with ozone (reaction (1.4)) yielding a net loss of the sum of the two over extended timescales. Hence it is conceptually useful to consider atomic oxygen and ozone together as an "odd oxygen" family distinct from the much longer-lived form of "even oxygen", O_2.

1.1.3 Catalytic cycles

At first sight, no trace component in the stratosphere could be responsible for loss of odd oxygen, since the species involved would be rapidly consumed. This objection is removed if the trace constituent participates in a catalytic process that removes odd oxygen. In the 40 years following Chapman's groundbreaking work it has become clear that stratospheric ozone is chemically destroyed not solely by reaction with atomic oxygen but also by hydrogen and nitrogen oxide chemistry [*Bates and Nicolet*, 1984; *Crutzen*, 1970]. Each of these species may also be considered in terms of its own odd hydrogen and odd nitrogen families, the members of which can interchange chemically with one another. The following reaction cycles illustrate the fact that hydrogen and nitrogen oxides can destroy odd oxygen in a catalytic fashion wherein the initiating active species are regenerated, so that even small amounts of these gases can influence the much greater ozone abundances.

$$\left.\begin{array}{l} O + OH \rightarrow O_2 + H \\ H + O_2 + M \rightarrow HO_2 + M \\ O + HO_2 \rightarrow O_2 + OH \end{array}\right\} \quad \text{Net Cycle:} \quad O + O + M \rightarrow O_2 + M \tag{1.6}$$

$$\left.\begin{array}{l} OH + O_3 \rightarrow HO_2 + O_2 \\ HO_2 + O_3 \rightarrow OH + 2O_2 \end{array}\right\} \quad \text{Net Cycle:} \quad 2O_3 \rightarrow 3O_2 \tag{1.7}$$

$$\left.\begin{array}{l} NO + O_3 \rightarrow NO_2 + O_2 \\ O + NO_2 \rightarrow NO + O_2 \end{array}\right\} \quad \text{Net Cycle:} \quad O + O_3 \rightarrow 2O_2 \tag{1.8}$$

Perturbations to the natural abundances of odd hydrogen may arise through human modifications of source gases such as H_2O and CH_4, while natural odd nitrogen can be perturbed

through direct emissions of aircrafts flying at high altitudes, by nuclear explosions, or by changes of its primary source gas, N_2O. Measurements from the Halogen Occultation Experiment (HALOE) performed in the last decade have shown an increase in stratospheric water vapor across the globe and this trend was found to be greater than expected [*Evans et al.*, 1998].

In 1974 it was shown that chlorine could also engage in a catalytic cycle resulting in ozone destruction [*Stolarski and Cicerone*, 1974]. The main reactions forming chlorine catalytic cycles are

$$\left.\begin{array}{l} Cl + O_3 \rightarrow ClO + O_2 \\ ClO + O \rightarrow Cl + O_2 \end{array}\right\} \quad \text{Net Cycle:} \quad O + O_3 \rightarrow 2O_2 \tag{1.9}$$

$$\left.\begin{array}{l} Cl + O_3 \rightarrow ClO + O_2 \\ ClO + ClO + M \rightarrow Cl_2O_2 + M \\ Cl_2O_2 + h\nu \rightarrow Cl + ClO_2 \\ ClO_2 + M \rightarrow Cl + O_2 + M \end{array}\right\} \quad \text{Net Cycle:} \quad 2O_3 \rightarrow 3O_2 \tag{1.10}$$

As was shown by *Wofsy et al.* [1975]; *Yung et al* [1980] and *McElroy* [1986], bromocarbons could also contribute to ozone depletion, particularly through the coupling of bromine and chlorine chemistry. The following reactions illustrate the chlorine-bromine catalytic cycle:

$$\left.\begin{array}{l} Cl + O_3 \rightarrow ClO + O_2 \\ Br + O_3 \rightarrow BrO + O_2 \\ BrO + ClO \rightarrow Br + ClO_2 \\ ClO_2 + M \rightarrow Cl + O_2 + M \end{array}\right\} \quad \text{Net Cycle:} \quad 2O_3 \rightarrow 3O_2 \tag{1.11}$$

Collectively, the depletion of ozone by chlorine, bromine, and the interactions between them are referred to as halogen chemistry. Although natural sources of chlorine and bromine exist, the main source of halogen compounds in the stratosphere is found to be halocarbons (see next Section) transported from the troposphere.

1.1.4 Halocarbons

Fluorinated chlorocarbons (CFCs) were developed in 1930 as a non-toxic non-flammable refrigerant. Dichlorodifluoromethan, CF_2Cl_2, is a typical member of this class of compounds. Chemical inertness has made the CFCs valuable as aerosol propellants, as boiling agents for plastic form production, and as solvents, in addition to their use as refrigerants. Other members of the halocarbon family are hydrogynated and brominated halocarbons, i.e., CHF_2Cl and CF_2BrCl, respectively.

In 1973, the presence of halogenated hydrocarbons in the troposphere was reported by *Lovelock et al.* [1973]. The CFCs was found to have solely anthropogenic origin and their lifetimes to be of up to hundreds of years. As was emphasized by *Molina and Rowland* [1974], the chlorofluorocarbons are not significantly soluble in water, nor do they react

with ocean or soil surfaces or with any chemical species present in the lower atmosphere. Their chemical destruction depends upon the ultraviolet light found in the stratosphere. This radiation breaks up the chlorofluorocarbon molecules, yielding Cl atoms that can go on to destroy ozone in catalytic cycles such as (1.9) and (1.10) as they move through the stratosphere.

1.1.5 The antarctic ozone hole

Measurable ozone depletion was first documented in the Antarctic spring at the British Antarctic Survey station at Halley [*Farman et al.*, 1985]. It was shown that the ozone hole is confined to particular seasons (spring) and to south polar latitudes. As the satellite measurements confirmed that the depletion extended over roughly the entire continent, the phenomenon became known as the Antarctic ozone hole.

As was noted by *Dobson* [1968], there is less ozone naturally present over Antarctica than over the Arctic in winter and spring, but this climatological difference between the natural ozone levels over the poles of the two hemispheres should not be confused with the abrupt decline near the mid-1970s. Analyzing historical measurements of total ozone, *Newman* [1994] shows that the ozone hole began in the last few decades.

There are two features of polar stratospheric meteorology and dynamics that appear to have a close bearing on the interpretation of the ozone depletion. The very low temperatures lead to the formation of high-altitude clouds: the so-called polar stratospheric clouds which are considered to be involved in polar ozone destruction. They are much more common in colder Antarctic than in Arctic regions. The second, and related, feature of polar meteorology is that a vortex forms as air cools and descends during the winter. The vortex develops a core of very cold air, and it is these low temperatures that allow the polar stratospheric clouds to form in the lower stratosphere. During the winter and early spring the air at polar latitudes is almost sealed off from that at lower latitudes due to the vortex. There is a small downward circulation which drives the polar air through the cold core of the vortex that contains the polar stratospheric clouds. As these clouds are involved in heterogeneous chemistry, the downward circulation allows the core region to act as a "chemical processor".

The central feature of the perturbed chemistry of the polar stratosphere is the conversion of reservoir compounds to catalytically active species (or their precursors) on the surface of the polar stratospheric clouds. Most of the chlorine in the stratosphere is usually bound up in the reservoir molecules hydrogen chloride and chloride nitrate, as a result of the reactions

$$\mathrm{Cl} + \mathrm{CH_4} \rightarrow \mathrm{HCl} + \mathrm{CH_3} \tag{1.12}$$

$$\mathrm{ClO} + \mathrm{NO_2} + \mathrm{M} \rightarrow \mathrm{ClONO_2} + \mathrm{M} \tag{1.13}$$

Liberation of the active chlorine from the reservoirs is normally rather slow. But it turns out that two reservoir molecules can react together in the presence of ice particles, such as those that make up the polar stratospheric clouds, for example,

$$\mathrm{ClONO_2} + \mathrm{HCl} \rightarrow \mathrm{Cl_2} + \mathrm{HNO_3} \tag{1.14}$$

The outcome is that molecular chlorine is released as a gas, and the nitric acid remains in the ice particles, which can ultimately transport water and nitric acid out of vortex. The molecular chlorine is photodissociated to atoms

$$Cl_2 + h\nu \rightarrow Cl + Cl \tag{1.15}$$

if sunlight is present. Thus, PSCs disturb the ballance between active and reservoir chlorine in two related ways. Namely, they provide surfaces on which unusual chemical change can occur and they transport active nitrogen out of the stratosphere in the form of HNO_3 reducing the amounts of $ClONO_2$ reservoir that can be formed in the first place.

1.2 Climate change

Although already discussed over a century ago by *Arrhenius* [1896] and others, the issue of global warming caused by the injection of the so-called greenhouse gases such as CO_2 into the atmosphere has become prominent in recent years. This is because of the rapid increase of the atmospheric CO_2 associated with the combustion of fossil fuels in the second half of the twentieth century. The recognition that other species can behave in a similar manner but often more effectively than CO_2 has resulted in the definition of the "global warming potential" of trace gases. The list of greenhouse gases now comprises many species, including CO_2, CH_4, nitrous oxide (N_2O), CFCs and tropospheric ozone.

Concern about increasing CO_2 levels is directed first towards possible consequences for out climate that would follow increased radiation trapping. Progressively more sophisticated and complete models of the climate system have shown that mean surface temperatures rise by approximately 3°C for a doubling in CO_2 concentration. Positive feedbacks, such as decreased albedo because of shrinkage of the polar snow caps, can amplify small temperature changes.

Similar to CO_2, the atmospheric methane levels have been rapidly increasing during the last few decades due to human activities. Atmospheric methane has largely biogenic sources, arising from bacterial fermentation in swamplands, tropical rain forests, and the intestinal tracts of livestock and termites. The growth in rice paddy cultivation and in cattle farming, which are a response to a population growth, could account for increased methane production.

Input of nitrogen into cropland is an additional way in which average world temperatures might be raised in the future. Commercial fertilizers and nitrogen-fixing leguminous crops both have the potentiality of increasing emissions of N_2O from soils. The nitrogen fixed annually by combustion and in manufacturing fertilizers has now reached half of what plants produce naturally.

Concern also arises over the release by man of CFCs to the atmosphere. These compounds possess strong absorption bands in the infra-red region that, by chance, coincide with regions where CO_2 itself has relatively weak absorption. The CFCs thus have the potential of closing the atmospheric "windows" through which radiation could escape to space, and the contribution of such compounds to greenhouse warming may consequently

be much greater than the simple additive effect of the radiation trapped by the CFCs themselves.

A warmer Earth will have a smaller equator-to-pole temperature contrast, because the excess heating is concentrated in polar regions. Seasonal contrasts will become less pronounced. With less potential energy available in the system to convert to kinetic energy, the atmospheric heat engine will run more slowly. Large-scale circulation patterns will be influenced, and some regional climatic changes may be larger than the average. A warmer atmosphere and ocean will result in more evaporation and precipitation. Warming in the polar regions could approach as much as 10°C by the middle of the next century. Formation of sea-ice will be reduced in both polar regions, and climatologists are tantalized by the possibility that Arctic Ocean ice might disappear and not return. Modification of the entire climate of the Arctic Basin would ensue, with profound ecological consequences on land and in the sea, and with possible release of much CH_4 from methane hydrate which is known as the permafrost. The ice sheets of the Antarctic and Greenland are more likely geological formations than components of the hydrologic system. Since they rest on solid bedrock, their melting, or sliding into the ocean, would cause a rise in sea-level. Straightforward melting of the enormous masses of ice would probably take many thousands of years, but another mechanism could accelerate the process. Much of the West Antarctic ice sheet rests on bedrock that is below sea-level. Warmer ocean water would work its way under the ice sheet, separating it from the bedrock and causing it to slide towards the ocean. Disintegration and melting of the ice would then be relatively rapid because of the more intimate contact with the water and because of diminished thermal insulation. If the entire West Antarctic ice sheet were to disappear, a rise in sea-level of 5 to 7 m would result, with a serious impact on all the shorelines of the world. The best estimates given by *IPCC* [1990] for sea level rises are 0.2 m by 2020 and 0.4 m by 2070.

The governments of the world, concerned with the potentially negative consequences of global warming, have mandated that evaluations be made to provide national and international policy-makers with an accurate assessment of our current understanding of climate change. At the recent Earth Summit at Kyoto, one of the most important topics on the agenda was concerned with this issue. A number of international agreements resulted which intend to decrease the atmospheric loading of the greenhouse gases.

1.3 Stratosphere-troposphere exchange

Dynamical, chemical, and radiative coupling between the stratosphere and troposphere are among the many important processes that must be understood for prediction of global change. Of special significance is the transport of trace chemical species, natural and anthropogenic, between the stratosphere and troposphere. For instance, anthropogenic species transported from the troposphere into the stratosphere initiate much of the chemistry responsible for stratospheric ozone depletion [*WMO*, 1995]. Conversely, downward transport from the stratosphere not only constitutes the main removal mechanism for many stratospheric species, including those involved in ozone depletion, but also represents a sig-

nificant input of ozone and other reactive species into the tropospheric chemical system [*Levy et al.*, 1980]. Chemical effects from stratosphere-troposphere exchange can, in turn, influence the radiative flux balance in the troposphere and lower stratosphere [*Ramaswamy et al.*, 1992; *Toumi et al.*, 1994]. Stratosphere-troposphere exchange can therefore have a significant role in the radiative forcing of global climate change.

It is now widely appreciated that the dynamics of the troposphere and the stratosphere are, in principle, inseparable. However, there are strong reasons why the distinction between troposphere and stratosphere remains useful. One of them is that vertical transport of air and chemical species through the depth of the troposphere can occur on timescales as short as a few hours via moist convection and on timescales of days via baroclinic eddy motions in middle latitudes. By contrast, vertical transport through a similar altitude range in the stratosphere takes months, indeed a year or more in the lower stratosphere, and this vertical transport must be accompanied by radiative heating or cooling. There are important implications therefore both for chemistry and for radiative flux balances. The difference between the vertical transport time scales in the stratosphere and troposphere is a part of what lies behind, for instance, the rapid increase in ozone mixing ratio and the rapid decrease in water vapor mixing ratio with altitude observed just above the tropopause.

As pointed out by *Holton et al.* [1995], due to relatively long timescales for vertical transport within the stratosphere and the inhomogeneity of the stratospheric photochemical environment, as regards both actinic radiative fluxes and chemical tracer distributions, stratosphere-troposphere exchange cannot be thought of in terms of slow transport between two well-mixed boxes; single-number measures of exchange are therefore, by themselves, of limited utility. More useful measures of stratosphere-troposphere exchange must concern not only the transport across the tropopause but also the rate at which tropospheric material is supplied to and removed from the regions in the stratosphere in which there are chemical sources and sinks, for whichever chemical species are of interest. It is necessary therefore to take into account the species photochemical sensitivities at different altitudes and latitudes, and the global-scale circulation including the spatiotemporal structure of transport within the stratosphere.

1.4 International efforts to control substances responsible for ozone depletion and greenhouse constituents

1.4.1 Montreal Protocol

An important step to reduce the emission of ozone depleting substances was made in the "Montreal Protocol on Substances that Deplete the Ozone Layer" that was agreed in September 1987 at the Headquarters of the International Civil Aviation Organization in Montreal, and proved to be far tougher than anyone had thought possible only a few months before.

The Protocol came into force on January 1st, 1989, by which time 29 countries and the EEC representing approximately 82 percent of world consumption had ratified it. Since then several other countries have joined. 155 countries are now Parties to the Convention and the Protocol, of which well over 100 are developing countries. Each party of the Protocol was obliged to freeze, and then reduce according to an agreed timetable, its production and consumption of CFCs as well as to freeze consumption and production of halons and some other species contributing to ozone depletion. As "final objective" of the Montreal Protocol the "elimination" of ozone-depleting substances production was set.

Recently, reports have shown that, owing to the Montreal Protocol and its subsequent adjustments and amendments (the revised Montreal Protocol), growth rates and abundances of chlorine and bromine containing compounds have noticeablely decreased [*Elkins et al.*, 1993; *Montzka et al.*, 1996; *Anderson et al.*, 2000].

1.4.2 Kyoto Protocol

At a conference held December 1 - 11 1997, in Kyoto, Japan, the Parties to the UN Framework Convention on Climate Change agreed to an historic Protocol to reduce greenhouse gas emissions by harnessing the forces of the global marketplace to protect the environment. A central feature of the Kyoto Protocol is a set of binding emissions targets for developed nations. An entitlement was assigned to each country to emit not more than a fixed quantity of greenhouse gases (CO2, CH4, N2O, Hydrofluorocarbons, etc.) during a 5-year commitment period commencing in 2008. The specific limits vary from country to country, though those for the key industrial powers of the European Union, Japan, and the United States are similar – 8% below 1990 emissions levels for the EU, 7% for the U.S., 6% for Japan.

To show compliance with the agreed aims of the Kyoto Protocol and to establish the processes responsible for the changes in the abundance of other greenhouse gases the anthropogenic emissions of greenhouse gases from continents or countries have to be monitored. Therefore global measurements of these species, which can only be performed by means of space-borne instruments, are of great significance.

Chapter 2

The SCIAMACHY instrument

2.1 Scientific objectives and targeted constituents

The SCanning Imaging Absorption spectroMeter for Atmospheric CHartographY (SCIAMACHY) is a space-based spectrometer designed to measure the scattered and reflected solar radiation in nadir and limb viewing geometry as well as the radiation transmitted through the atmosphere in solar and lunar occultation geometry. Moreover, the extraterrestrial solar irradiance and the lunar radiance will be measured. The measurements will be performed in the ultraviolet, visible and near infrared spectral regions (240 – 2380 nm) at moderate spectral resolution (0.2 – 1.5 nm). As mentioned in the Introduction, the SCIAMACHY instrument is intended to be launched in 2001 on board the European Space Agency's Environmental Satellite. Details on the SCIAMACHY instrument concept and technical parameters can be found in [*Burrows and Chance*, 1991; *Goede*, 1994; *Mager*, 1997; *Goede*, 1999]. A small-scale version of SCIAMACHY, the Global Ozone Monitoring Experiment (GOME) [*Burrows et al.*, 1999], was successfully launched on board the ERS-2 satellite in April 1995.

The overall mission objective of the SCIAMACHY mission is to determine globally the amounts and distributions of atmospheric constituents and thereby improve our knowledge of global atmospheric change and related issues of importance to the chemistry and physics of our atmosphere. More specifically, main scientific studies and areas of applications to be pursued using SCIAMACHY data are as follows [*Bovensmann et al.*, 1999]:

- the impact of tropospheric pollution arising from industrial activity and biomass burning,
- exchange processes between the stratosphere and the troposphere,
- stratospheric chemistry in the polar regions, e.g., under "ozone hole" conditions, and at mid-latitudes,
- modulation of atmospheric composition resulting from natural phenomena such as volcanic eruptions, solar output variations, e.g., solar cycle, or solar proton events.

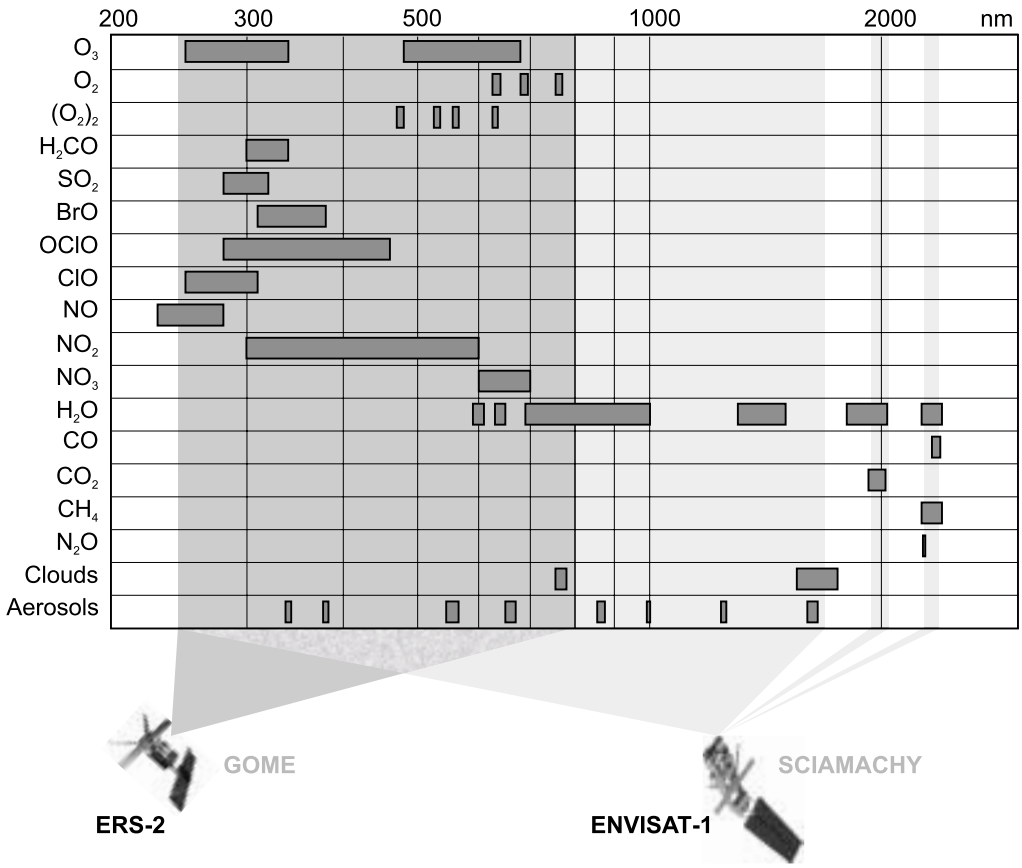

Figure 2.1: Spectral range covered by GOME and SCIAMACHY and spectral windows where atmospheric constituents are to be retrieved.

Figure 2.1 shows the wavelength range to be observed by the SCIAMACHY instrument in comparison to the spectral range covered by the GOME instrument as well as positions of spectral windows where atmospheric constituents are to be retrieved. Figure 2.2 depicts the altitude ranges where the measurements are to be made to retrieve the vertical distribution of the atmospheric constituents targeted by SCIAMACHY. Due to higher signal to noise ratio, the retrieval from the occultation measurements yields information over a wider altitude range then from the limb measurements. The combined use of nadir and limb measurements is assumed to yield tropospheric amounts of the trace gases down to the ground or the cloud top, depending on cloud cover.

The trace gases tropospheric amounts as well as surface spectral reflectance, aerosol and cloud parameters retrieved form the combined limb-nadir measurements can be used for studies of the oxidizing capacity of the troposphere, photochemical O_3 production and destruction, and tropospheric pollution. The measurements of the high-resolved profiles of the tracers O_3, H_2O, N_2O, CH_4, and aerosol performed by SCIAMACHY are of primary significance for the investigation of stratosphere-troposphere exchange [*Holton et al.*, 1995].

In general, SCIAMACHY measurements will yield detailed information about the de-

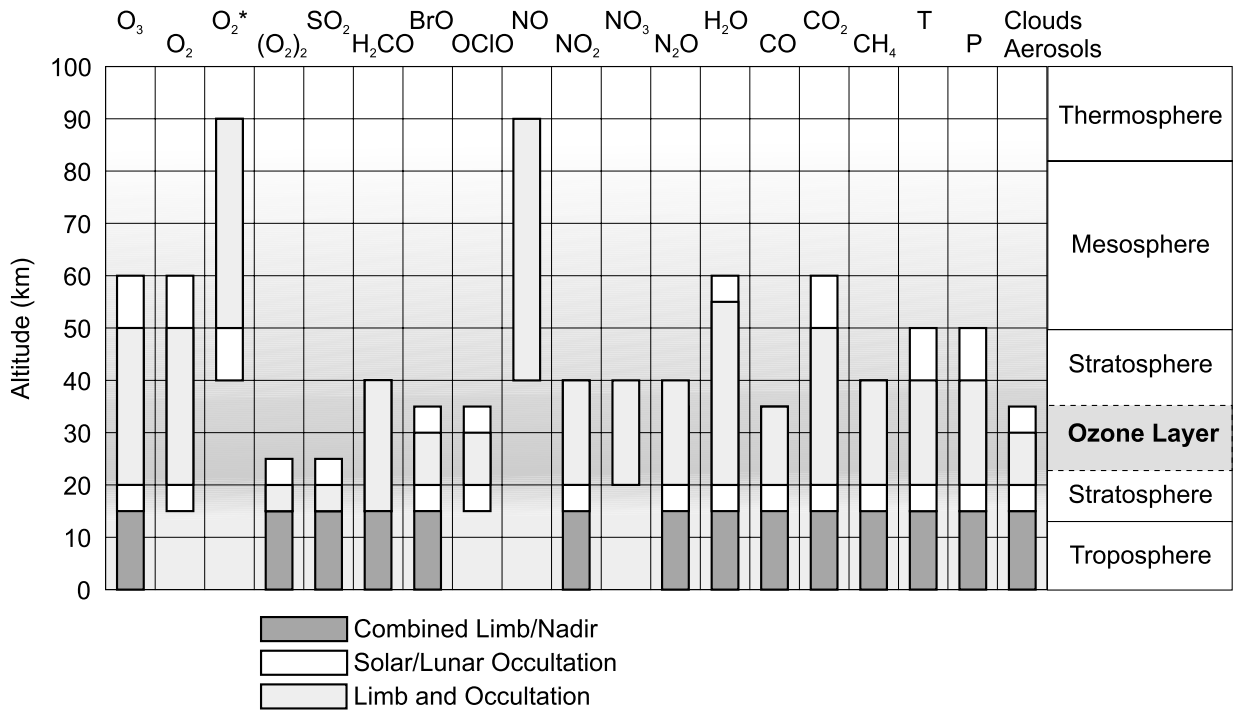

Figure 2.2: Altitude ranges of the atmospheric constituents targeted by SCIAMACHY.

velopment of stratospheric ozone above the Arctic and Antarctica, the global stratospheric active halogen species (BrO, ClO, OClO), and the global ozone budget as a function of the height in the atmosphere. The vertical distribution in the stratosphere of other tracers (NO_2, BrO, CH_4, N_2O, etc.) on a global scale will be obtained as well. These measurements will be of utmost significance to study the stratospheric chemistry and dynamics. This information is also required to test accuracy of current stratospheric photochemical models and their predictive capability.

The profiles of O_3, H_2O, N_2O, NO, O_2, and $O_2(^1\Delta)$ in the upper stratosphere and lower mesosphere retrieved from the SCIAMACHY measurements will be used to study an opportunity for the early detection of climate change [*Chandra et al.*, 1997] as well as the ozone destruction by the mesospheric and upper-stratospheric NO. Using these data, the mesospheric source of stratospheric NO_x will be quantified. Moreover, the combination of the height-resolved O_3, $O_2(^1\Delta)$, and UV radiance products from SCIAMACHY provides detailed information about the photolysis of O_3 in the upper stratosphere and mesosphere.

For use in climate research, SCIAMACHY measurements will provide the distributions of several important greenhouse gases (O_3, H_2O, CH_4, N_2O, and CO_2), aerosol and cloud data, surface reflectance, the incoming solar irradiance and the outgoing radiance, as well as profiles of pressure and temperature (via O_2 and CO_2). As it is intended that SCIAMACHY observations are to be made for many years, this long-term dataset will provide much unique information useful for the study of the earth-atmosphere system as well as variations of solar output and its impact on climate change.

2.2 Instrument design

The SCIAMACHY instrument is a passive remote sensing moderate-resolution spectrometer. It comprises a mirror system, a telescope, a spectrometer, and thermal and electronic subsystems. Except for scan mirrors, all spectrometer parts are fixed. The spectra are recorded simultaneously in the spectral range from 240 nm to 1750 nm and in two selected spectral windows in near infrared spectral region, namely, 1940 – 2040 nm and 2265 – 2380 nm. To suppress any stray light within the instrument the double spectrometer design was selected. Initially, light from the spectrometer slit is collimated and directed into a pre-dispersing prism. The light leaving the pre-dispersing prism is then separated into four parts using reflective optics. The shorter wavelengths of the spectrum are directed to channel 1 (240 – 314 nm) and channel 2 (314 – 405 nm) respectively. The majority of the light in the spectrum (405 – 1750 nm) passes without reflection to channels 3 – 6. The infrared part of the spectrum (1940 – 2380 nm) is reflected toward channels 7 and 8. Dichroic mirrors are used to select the wavelength ranges for channels 3, 4, 5, 6 and to sep-

Table 2.1: Spectral coverage and resolution of SCIAMACHY channels.

	Channel	Spectral Range [nm]	Spectral resolution [nm]
High Resolution Channels	1	240 - 314	0.24
	2	309 - 405	0.26
	3	394 - 620	0.44
	4	604 - 805	0.48
	5	785 - 1050	0.54
	6	1000 - 1750	1.48
	7	1940 - 2040	0.22
	8	2265 - 2380	0.26
Polarization Measurement Devices	PMD1	310 - 377	broadband
	PMD2	450 - 525	broadband
	PMD3	617 - 705	broadband
	PMD4	805 - 900	broadband
	PMD5	1508 - 1645	broadband
	PMD6	2265 - 2380	broadband
	45 deg	802 - 905	broadband

arate light for channel 7 from that for channel 8. Further, in each individual channel, the light is dispersed by the grating and focused then into linear 1024 pixel detector array. To minimize detector noise and dark current, the diode arrays are cooled. The SCIAMACHY instrument is also equipped with seven broadband detectors, polarization measurement devices (PMD), which will be used to determine the polarization characteristics of the incoming light. The spectral coverage of the SCIAMACHY channels and corresponding spectral resolutions are summarized in Table 2.1.

2.3 Observational modes

2.3.1 Nadir mode

In nadir mode (Fig. 2.3, upper plot) the solar radiation scattered in the atmosphere and reflected from the Earth's surface is collected by the detector. In this mode, the atmospheric volume beneath the spacecraft is observed. The radiation from the Earth's scene is directed by the nadir mirror into a telescope which focuses the beam onto the entrance slit of the spectrometer. During nadir measurement the scans across the satellite track will be performed. Each scan covers an area on the ground of approximately 30 km along track by 960 km across track. The spatial resolution in the nadir scan mode is determined by the combination of the scan speed and the integration time of the detectors. The scan speed along track is determined by the spacecraft speed and the across-track speed is determined by the nadir scan mirror rate. A typical spatial resolution in nadir mode is approximately 30 km along track by 240 km across track. To minimize the loss of spatial information, an alternative data processing can be used in selected spectral windows resulting in a higher spatial resolution for important constituents such as O_3, NO_2, H_2O, aerosols, and clouds of 30 km along track by 60 km across track.

2.3.2 Limb mode

In limb mode (Fig. 2.3, middle plot) the solar radiation scattered in the atmosphere is observed by the instrument. The incoming radiation is reflected by the limb mirror to the nadir mirror and then into the telescope which focuses the beam onto the entrance slit of the spectrometer. In this measurement mode the spectrometer slit is projected parallel to the horizon by a combination of the limb and nadir mirrors. Performing limb measurements, the limb mirror scans the atmosphere in horizontal (azimuth) direction, whereas appropriate movement of the nadir mirror results in a vertical (elevation) scan direction. A typical limb scan cycle comprises 34 horizontal scans at different tangent heights starting 3 km below the horizon. After each horizontal scan, which has a duration of 1.5 s, a step of 3 km in the tangent height is made by the evaluation mirror. Each horizontal scan of the atmosphere covers 960 km in the horizontal (across-track) direction. The vertical resolution is approximately 3 km. The latter is determined by the geometrical field of view and pointing stability of the instrument as well as by the multiple scattering in the atmosphere. The individual spatial resolution within a 960-km scan in the horizontal

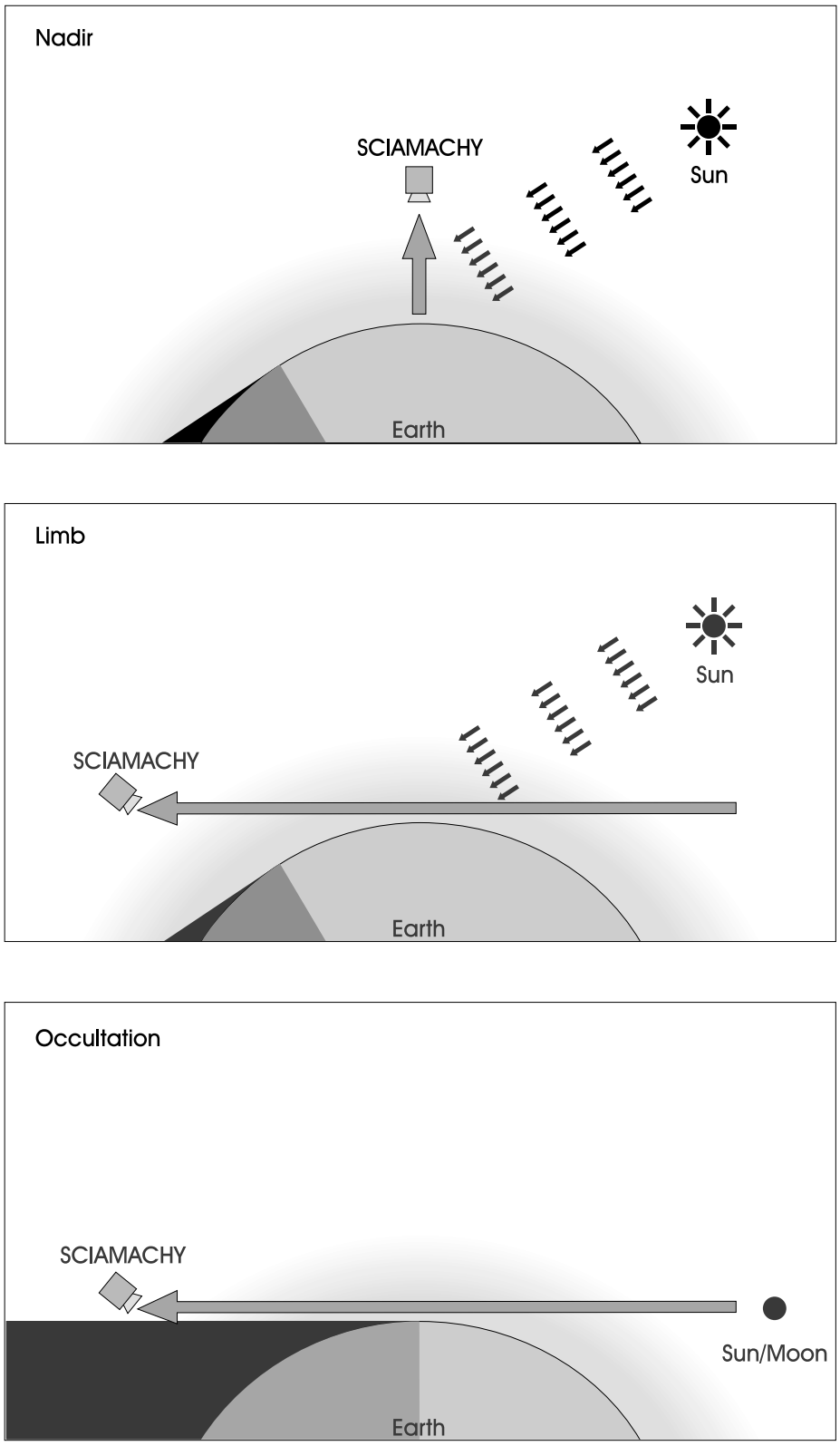

Figure 2.3: Observational geometries of the SCIAMACHY instrument.

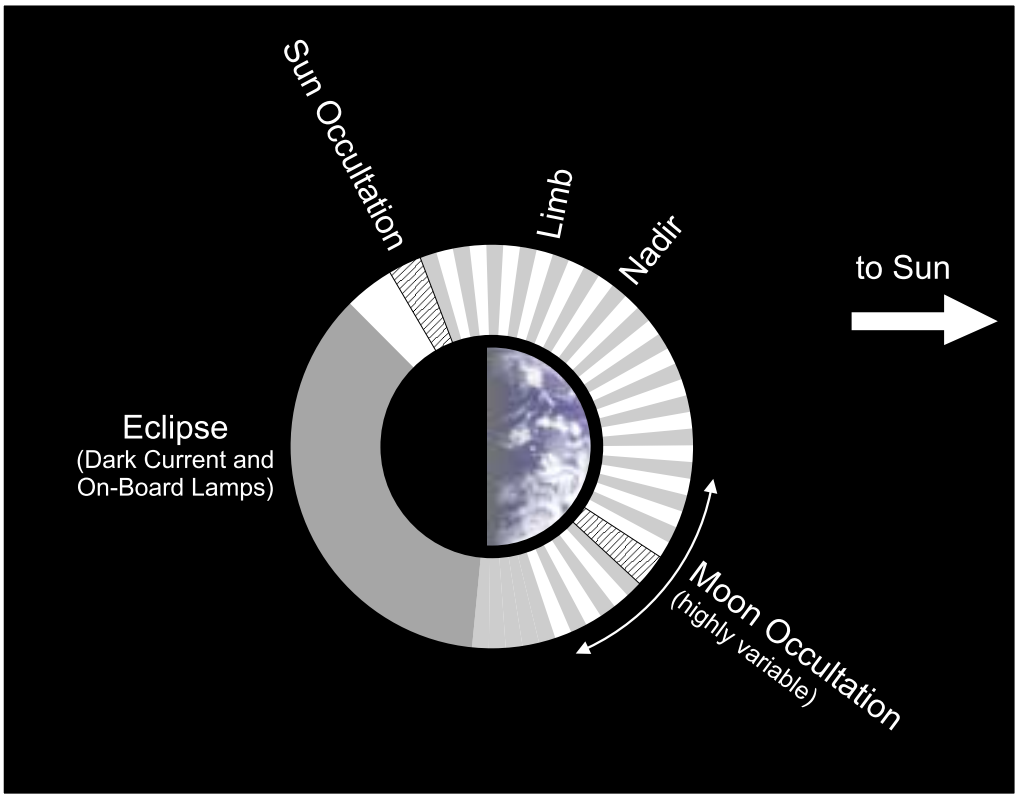

Figure 2.4: Typical sequence of SCIAMACHY measurements performed during one orbit of ENVISAT.

direction across track is typically 240 km, being determined by the integration time. The spatial resolution and the spatial coverage of the horizontal scan refer to the tangent point.

2.3.3 Occultation mode

Occultation measurements (Fig. 2.3, lower plot) are performed using the elevation and azimuth scan mirrors in a manner similar to that for the limb mode but with the Sun or Moon in the instrument's field of view. In this measurement mode the solar/lunar radiation transmitted through the atmosphere is collected by the detector. Solar occultation measurements are planned to be performed at each orbit during sunrise. For the ENVISAT orbit solar occultation is restricted to latitudes between 65° and 90°N. Lunar occultation will be performed from half Moon to full Moon. For periods of 5 – 8 days per month lunar occultation measurements will provide latitudinal coverage from 30° to 90°S. During the sunrise SCIAMACHY scans several times over the full solar disk, whereas for the lunar measurement longer integration times are necessary and a "stare" mode similar to that used on the Halogen Occultation Experiment (HALOE) [*Russel et al.*, 1993] is implemented. Due to the strong signal the integration time for solar occultation measurements can be substantially reduced allowing a horizontal resolution of 30 km and a vertical

resolution of 2.5 km to be achieved. Similar to the limb measurements, the resolution at tangent point is meant.

2.3.4 Sequence of measurements in orbit

ENVISAT will fly in a near polar (98.55° inclination) sun-synchronous orbit with an orbital period of about 100 min. A typical sequence of measurements which will be performed by SCIAMACHY during one orbit is shown in Figure 2.4. A typical orbit starts with a limb measurement of the twilight atmosphere followed by the solar occultation measurement during sunrise over the North Pole and an optimized limb-nadir sequence. If the Moon is visible, lunar occultation measurements will be performed in the Southern Hemisphere (30° – 90°S) every second orbit. All these measurements, with the exception of lunar occultation, will be performed every orbit, that is, 14 orbits per day. In addition to the above mentioned measurements, the solar irradiance measurements and a number of calibration measurements will be performed. Details on the calibration measurements can be found in [*Frerick et al.*, 1997]. Most of these calibration measurements will be performed during the eclipse part of the orbit.

Chapter 3

The radiative transfer theory

3.1 Radiative transfer equation

Intensity is the basic quantity characterizing the radiation field. In common with astrophysical usage the word *intensity* denotes *specific intensity of radiation*, i.e., the flux of energy in a given direction per second per unit wavelength range per unit solid angle per unit area perpendicular to the given direction [*Goody*, 1964]. According to *Sobolev* [1975], the intensity at a given place in space in a particular direction is defined in the following manner. If $d\sigma$ is an elementary area which is perpendicular to the chosen direction $\mathbf{e}_s$ and the radiation falls in the frequency interval from ν to $\nu + d\nu$ in the solid angle $d\omega$ in the time dt, then the amount of radiant energy $\mathcal{E}$ falling on the area from the given direction $\mathbf{e}_s$ will be proportional to $d\sigma\, d\nu\, d\omega\, dt$, i.e.,

$$\mathcal{E} = I\, d\sigma\, d\nu\, d\omega\, dt\ . \tag{3.1}$$

The proportionality coefficient I is called the *intensity* of radiation. Generally speaking, quantity I depends on the coordinates of the given point, on direction, on the frequency ν, and eventually on the time. Possible time dependence will not be considered below, i.e., the radiation field will always be considered to be stationary. For simplicity, dependence of the intensity as well as of all medium characteristics on the frequency will not be indicated below.

An important characteristic of radiation intensity is the fact that in empty space it does not change along a ray with distance from the source. The totality of interactions between radiation and medium is classed as either extinction or emission. The two processes are distinguished by the sign of the change of radiation intensity as a result of interaction.

Extinction refers to any process which reduces the intensity in the direction under consideration, and thus includes both scattering from the direction $\mathbf{e}_s$ into another directions as well as absorption. The fraction of the energy incident on the plane layer of infinitesimal thickness ds which is removed from the original beam can be written as a formal statement defining the *extinction coefficient* α in the following manner:

$$\mathcal{E}_{ext} = \alpha\, ds\, \mathcal{E}\ . \tag{3.2}$$

The extinction coefficient depends on the frequency of the radiation and coordinates of the given point. Thus, the energy removed in the volume element $dV = ds\,d\sigma$ from the ray falling on this volume element from the given direction in the solid angle $d\omega$ in the frequency interval from ν to $\nu + d\nu$ in the time period dt is given by

$$\mathcal{E}_{ext} = \alpha\, ds\, I\, d\sigma\, d\nu\, d\omega\, dt\ . \tag{3.3}$$

Emission refers to any process which increases the intensity in the direction under consideration, and thus includes both scattering into the beam from other directions, as well as thermal or other emission processes within the volume. The energy emitted by the volume element dV within the solid angle $d\omega$ in the frequency interval from ν to $\nu + d\nu$ in the time period dt can be written as a formal statement defining the *source function* J in the following manner:

$$\mathcal{E}_{emit} = \alpha\, J\, ds\, d\sigma\, d\nu\, d\omega\, dt\ . \tag{3.4}$$

Considering the radiation entering and leaving the volume element dV within a solid angle $d\omega$ in the frequency interval from ν to $\nu + d\nu$ in the time period dt, the following relation for the difference between energy leaving and entering the volume element is obtained:

$$d\mathcal{E} = dI\, d\sigma\, d\nu\, d\omega\, dt\ . \tag{3.5}$$

Here, I and $I + dI$ are assumed to be the intensity where the ray enters the volume element and the intensity leaving the volume element, respectively.

On the other hand, employing the energy conservation law, the difference between the energy leaving and entering the volume element can be written as

$$d\mathcal{E} = -\,\mathcal{E}_{ext} + \mathcal{E}_{emit}\ . \tag{3.6}$$

Substituting Eqns. (3.3)–(3.5) into Eq. (3.6) results in

$$dI\, d\sigma\, d\nu\, d\omega\, dt = -\,\alpha\, I\, ds\, d\sigma\, d\nu\, d\omega\, dt + \alpha\, ds\, J\, d\sigma\, d\nu\, d\omega\, dt\ . \tag{3.7}$$

It follows that

$$\frac{dI}{ds} = -\,\alpha\,(I - J)\ . \tag{3.8}$$

Equation (3.8) is the *radiative transfer equation* which determines changes in the intensity of radiation as it passes through an absorbing and emitting medium.

In UV–Visible–near IR spectral region the contribution of thermal emission processes to the source function is negligible and, thus, the source function comprise only scattering processes. However, in the case of a medium which scatters radiation, the quantity J depends on the intensity falling on the elementary volume from all directions.

Let an intensity I fall on an elementary volume with a cross section $d\sigma$ and a height dh within the solid angle $d\tilde{\omega}$ in the direction forming an angle $\tilde{\Theta}$ with the normal to the base, see Fig. 3.1. It is apparent that the energy falling on the volume per unit frequency interval is given by

$$\mathcal{E} = I\, d\tilde{\omega}\, d\sigma \cos\tilde{\Theta}\ . \tag{3.9}$$

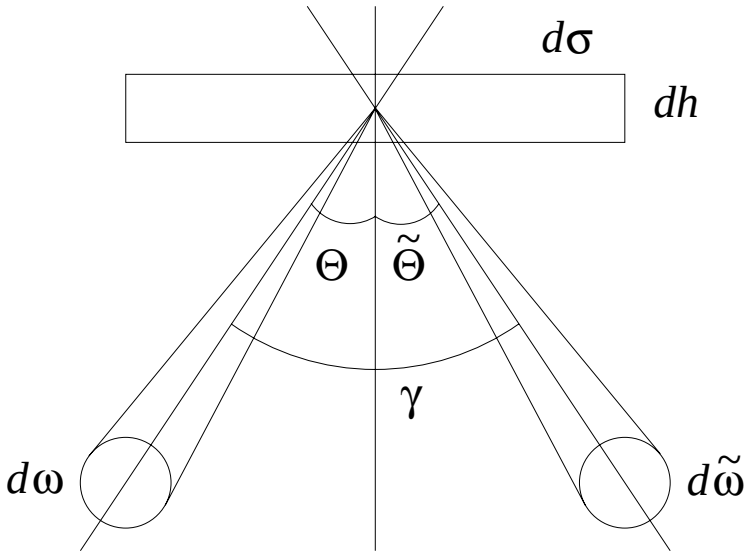

Figure 3.1: Interaction of a beam of light with an element of volume $dV = d\sigma\, dh$

Since the path traveled by the radiation in the volume is $dh \sec\tilde{\Theta}$, a fraction $\alpha dh \sec\tilde{\Theta}$ of the energy falling on the volume is absorbed by it, i.e., removed from the incident beam, so that the following relation for the absorbed energy is appropriate:

$$\mathcal{E}_{abs} = \alpha\, dh\, d\sigma\, I\, d\tilde{\omega}\ . \tag{3.10}$$

The energy scattered by the volume within the solid angle $d\omega$ in a given direction is found by multiplying the absorbed energy by the quantity $\varpi\, p(\gamma)\, d\omega/4\pi$, where γ is the angle between the directions of the incident and scattered radiation. The quantity ϖ represents the probability that a photon which interacts with an element of volume will be scattered rather then absorbed. It is called the *single scattering albedo*. The term $p(\gamma)\, d\omega/4\pi$ denotes the probability that the radiation is scattered into a solid angle $d\omega$ about a direction forming an angle γ with the direction of the incident radiation. The quantity $p(\gamma)$ is called the *phase function*. Clearly,

$$\int p(\gamma)\frac{d\omega}{4\pi} = 1\ , \tag{3.11}$$

where the integration is carried out over all directions. Taking into account that $d\omega = 2\pi \sin\gamma\, d\gamma$, Eq. 3.11 can be rewritten as follows:

$$\frac{1}{2}\int_0^\pi p(\gamma)\sin\gamma\, d\gamma = 1\ . \tag{3.12}$$

The quantities ϖ and $p(\gamma)$ depend on the frequency of the radiation and coordinates of the given point.

As a result, the following expression for the energy scattered within the solid angle $d\omega$ in a given direction, Θ, is obtained:

$$\mathcal{E}_{scat} = \varpi\, p(\gamma) \frac{d\omega}{4\pi}\, \alpha\, dh\, d\sigma\, I\, d\tilde{\omega}\ . \tag{3.13}$$

Since the radiation falls on the elementary volume from all sides, this expression has to be integrated over all directions of the incident radiation. It is evident that the result of this integration has to be equated to the total energy emitted within the solid angle $d\omega$ in the direction under consideration per unit frequency per unit time, i.e.,

$$\varpi\, \alpha\, dh\, d\sigma\, \frac{d\omega}{4\pi} \int p(\gamma)\, I\, d\tilde{\omega} = \frac{\mathcal{E}_{emit}}{d\nu\, dt}\ , \tag{3.14}$$

where $\mathcal{E}_{emit}$ is given by Eq. (3.4). Thus, combining Eqns. (3.4) and (3.14), the following equation for the scattering source function can be obtained:

$$J = \frac{\varpi}{4\pi} \int p(\gamma)\, I\, d\tilde{\omega}\ . \tag{3.15}$$

Substituting Eq. (3.15) for the scattering source function into Eq. (3.8) leads to the integro-differential radiative transfer equation in a medium that absorbs and scatters radiant energy:

$$\frac{dI}{ds} = -\,\alpha\, I + \alpha\, \frac{\varpi}{4\pi} \int p(\gamma)\, I\, d\tilde{\omega}\ . \tag{3.16}$$

Here, the thermal emission processes as well as the inelastic scattering were neglected.

In any planetary atmosphere the radiation field I can be split into two components: the direct radiation, which is never scattered in the atmosphere or reflected from the planetary surface, and the diffuse radiation, which is scattered or reflected at least once:

$$I = I_{dir} + I_{dif}\ . \tag{3.17}$$

Since there is no process in the atmosphere which increases the intensity of the direct solar radiation, the radiative transfer equation for the direct radiation leads to the homogeneous differential equation,

$$\frac{dI_{dir}(\mathbf{r}, \mathbf{e}_s)}{ds} = -\,\alpha(\mathbf{r})\, I_{dir}(\mathbf{r}, \mathbf{e}_s)\ , \tag{3.18}$$

having the following formal solution:

$$I_{dir}(\mathbf{r}, \mathbf{e}_{\rm o}) = C_0\, \exp\left(-\int_0^s \alpha(\hat{s})\, d\hat{s} \right)\ . \tag{3.19}$$

Here, the integration is performed from point $\mathbf{r}$ to the top of the atmosphere along the direction $\mathbf{e}_{\rm o}$, i.e., along the direct solar beam, s is the full path-length along the integration

line, and C_0 is an arbitrary constant. This constant can be determined using the following boundary condition at the top of the atmosphere:

$$I_{dir}(\mathbf{r}^{toa}, \mathbf{e}_o) = I_{irr} \ , \tag{3.20}$$

where I_{irr} is the solar irradiance at the top of the atmosphere traveling in the direction $\mathbf{e}_o$. Substituting Eq. (3.20) into Eq. (3.19), the following general expression for the direct radiation, which is known as Lambert–Beer law, can be obtained:

$$I_{dir}(\mathbf{r}, \mathbf{e}_s) = I_{irr} \, \exp\left(- \int_0^s \alpha(\hat{s}) \, d\hat{s} \right) \ , \tag{3.21}$$

If the Sun as a light source is assumed to have infinitesimal size, there is no direct radiation traveling in directions different from $\mathbf{e}_o$ and Eq. (3.21) can be rewritten as follows:

$$I_{dir}(\mathbf{r}, \mathbf{e}_s) = F_0 \, \delta(\mathbf{e}_s - \mathbf{e}_o) \, \exp\left(- \int_0^s \alpha(\hat{s}) \, d\hat{s} \right) \ , \tag{3.22}$$

where F_0 is the incident solar flux and $\delta(\mathbf{e}_s - \mathbf{e}_o)$ is the Dirac delta function.

Substituting Eq. (3.17) into Eq. (3.15), the following relation for the total source function, $J(\mathbf{r}, \mathbf{e}_s)$, can be obtained:

$$J(\mathbf{r}, \mathbf{e}_s) = \frac{\varpi}{4\pi} \int p(\mathbf{r}, \gamma) \, I_{dif}(\mathbf{r}, \mathbf{e}_s) \, d\tilde{\omega} + \frac{\varpi}{4\pi} \, F_0 \, p(\mathbf{r}, \gamma_o) \exp\left(- \int_0^s \alpha(\hat{s}) \, d\hat{s} \right) \ , \tag{3.23}$$

where γ_o is the angle between the directions of the incident direct solar beam and scattered radiation. Introducing the multiple scattering and the single scattering source functions as

$$J_{ms}(\mathbf{r}, \mathbf{e}_s) \equiv \frac{\varpi}{4\pi} \int p(\mathbf{r}, \gamma) \, I_{dif}(\mathbf{r}, \mathbf{e}_s) \, d\tilde{\omega} \tag{3.24}$$

and

$$J_{ss}(\mathbf{r}, \mathbf{e}_s) \equiv \frac{\varpi}{4\pi} \, F_0 \, p(\mathbf{r}, \gamma_o) \exp\left(- \int_0^s \alpha(\hat{s}) \, d\hat{s} \right) \ , \tag{3.25}$$

respectively, the following formal statement is obtained from Eq. (3.23):

$$J(\mathbf{r}, \mathbf{e}_s) = J_{ms}(\mathbf{r}, \mathbf{e}_s) + J_{ss}(\mathbf{r}, \mathbf{e}_s) \ . \tag{3.26}$$

Thus, the total source function is split into two terms: the multiple scattering and the single scattering source function.

Since direct radiance contains a delta function, it is more convenient to solve the radiative transfer equation, Eq. (3.8) or Eq. (3.16), only for diffuse radiance to avoid discontinuity, i.e., the following equation has to be solved to obtain the diffuse radiation field in the atmosphere:

$$\frac{dI_{dif}(\mathbf{r}, \mathbf{e}_s)}{ds} = - \alpha \left(I_{dif}(\mathbf{r}, \mathbf{e}_s) - J_{ms}(\mathbf{r}, \mathbf{e}_s) - J_{ss}(\mathbf{r}, \mathbf{e}_s) \right) \ . \tag{3.27}$$

3.2 Radiative transfer equation in orthogonal curvilinear coordinates

A numerical solution of the radiative transfer equation, Eq. (3.27), is only possible if a coordinate system is specified. The choice of the coordinate system depends on the medium curvature, the medium and the radiation field symmetry, and eventually several other conditions [*Jones and Bayazitoglu*, 1992]. In any coordinate system each point $\mathbf{r}$ is defined by three coordinates x_1, x_2, and x_3, and each direction $\mathbf{e}_s$ by two angles Θ and φ. Thus, the intensity in Eq. (3.27) is a function of five variables.

According to [*Korn and Korn*, 1968], the general expression for the path-length derivative along an arbitrary direction $\mathbf{e}_s$ is

$$\frac{d}{d\,s} = \mathbf{e}_s \cdot \nabla \; . \tag{3.28}$$

The nabla operator ∇ and the unit vector $\mathbf{e}_s$ are written in orthogonal curvilinear coordinates as follows:

$$\nabla = \sum_{i=1}^{3} \frac{1}{h_i}\,\mathbf{e}_i\,\frac{\partial}{\partial\,x_i} \; , \tag{3.29}$$

and

$$\mathbf{e}_s = \sum_{i=1}^{3} \xi_i\,\mathbf{e}_i \; , \tag{3.30}$$

where $\mathbf{e}_i$ are unit vectors tangential to the coordinate lines x_i, ξ_i are the direction cosines of the unit vector $\mathbf{e}_s$ in the selected curvilinear coordinate system, and h_i are metric coefficients given by

$$h_i = \sqrt{\left(\frac{\partial x}{\partial x_i}\right)^2 + \left(\frac{\partial y}{\partial x_i}\right)^2 + \left(\frac{\partial z}{\partial x_i}\right)^2} \; . \tag{3.31}$$

Here x, y, and z are the associated Cartesian coordinates. Thus, Eq. (3.28) for the path-length derivative along an arbitrary direction $\mathbf{e}_s$ in orthogonal curvilinear coordinates is written as follows:

$$\frac{d}{d\,s} = \sum_{i=1}^{3} \frac{\xi_i}{h_i}\,\frac{\partial}{\partial\,x_i} \tag{3.32}$$

Taking into account that the intensity is a function of five variables, i.e.,

$$I = I(x_1, x_2, x_3, \Theta(x_1, x_2, x_3), \varphi(x_1, x_2, x_3)) \; ,$$

each derivative in Eq. (3.32) may be split into

$$\frac{\partial}{\partial\,x_i} \equiv \frac{\partial}{\partial\,x_i^p} + \frac{\partial\,\Theta}{\partial\,x_i}\,\frac{\partial}{\partial\,\Theta} + \frac{\partial\,\varphi}{\partial\,x_i}\,\frac{\partial}{\partial\,\varphi} \; , \tag{3.33}$$

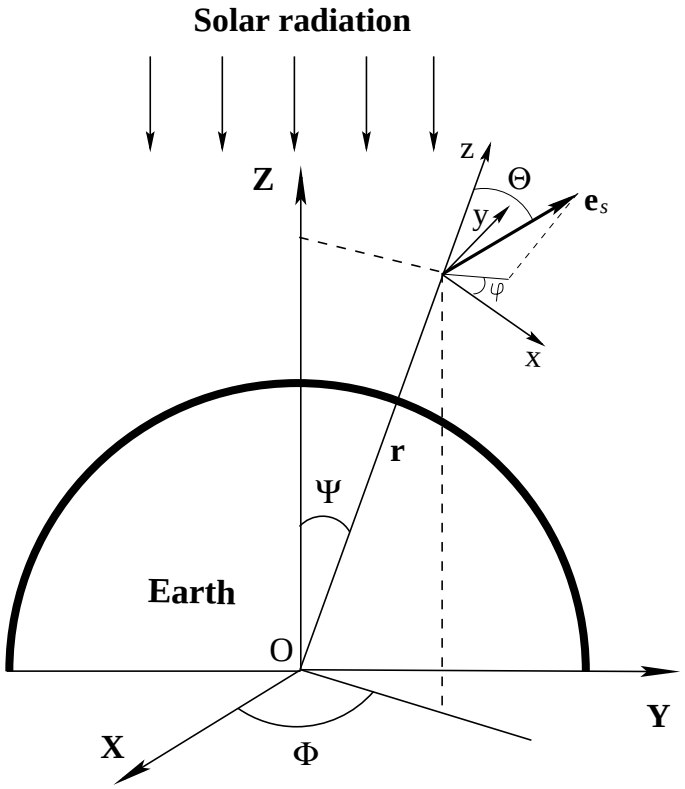

Figure 3.2: Definition of spherical coordinates.

where superscript p denotes a variation of x_i at Θ and φ constant. As a consequence, rewriting Eq. (3.32), the following general expression for the path-length derivative of the radiation intensity in an orthogonal curvilinear coordinate is obtained:

$$\frac{d\,I}{d\,s} = \sum_{i=1}^{3} \frac{\xi_i}{h_i} \frac{\partial\,I}{\partial\,x_i} + \sum_{i=1}^{3} \frac{\xi_i}{h_i} \left(\frac{\partial\,\Theta}{\partial\,x_i} \frac{\partial\,I}{\partial\,\Theta} + \frac{\partial\,\varphi}{\partial\,x_i} \frac{\partial\,I}{\partial\,\varphi} \right) . \tag{3.34}$$

The second two terms in Eq. (3.34) are commonly referred to as the angular redistribution terms.

3.3 Radiative transfer equation in spherical coordinates

In most publications on radiative transfer in a spherical atmosphere a spherical geocentric coordinate system depicted in Fig 3.2 is used to solve the radiative transfer equation, see, for example, [*Smokty*, 1967; *Germogenova et al.*, 1969; *Sobolev*, 1975; *Wilson and Sen*, 1980b; *Balluch*, 1996]. In this coordinate system, each point $\mathbf{r}$ is defined by the coordinates $x_1 = \Psi$, $x_2 = \Phi$ and $x_3 = r$ in the global (spatial) coordinate system (XYZ), and each direction $\mathbf{e}_s$ is defined by the angles Θ and φ in the local (directional) coordinate system.

In this case, the direction cosines of the unit vector $\mathbf{e}_s$ in the directional coordinate system are given by

$$\xi_\Psi \equiv \eta = \sin\Theta\,\cos\varphi\,, \tag{3.35}$$
$$\xi_\Phi \equiv \xi = \sin\Theta\,\sin\varphi\,, \tag{3.36}$$
$$\xi_r \equiv \zeta = \cos\Theta\,. \tag{3.37}$$

As discussed in Appendix A, if the direction cosines of the unit vector $\mathbf{e}_s$ in the global coordinate system (η_0, ξ_0, and ζ_0) are known the local direction cosines can be obtained as follows:

$$\eta = \cos\Psi\cos\Phi\,\eta_0 + \cos\Psi\sin\Phi\,\xi_0 - \sin\Psi\,\zeta_0\,, \tag{3.38}$$
$$\xi = -\sin\Phi\,\eta_0 + \cos\Phi\xi_{\,0}\,, \tag{3.39}$$
$$\zeta = \sin\Psi\cos\Phi\,\eta_0 + \sin\Psi\sin\Phi\,\xi_0 + \cos\Psi\,\zeta_0\,. \tag{3.40}$$

According to [*Vaillon et al.*, 1996], the derivatives $\partial\Theta/\partial x_i$ and $\partial\varphi/\partial x_i$ in Eq. (3.34) can be easily obtained from Eqns. (3.35)–(3.40) as discussed below.

Obviously, angles Θ and φ do not vary with the spatial variable $\mathbf{r}$, therefore,

$$\frac{\partial\Theta}{\partial r} = 0 \quad \text{and} \quad \frac{\partial\varphi}{\partial r} = 0. \tag{3.41}$$

Differentiating Eqns. (3.38) and (3.40) with respect to Ψ and taking into account that the direction cosines η_0, ξ_0, and ζ_0 do not depend on spatial coordinates, the following equations are obtained:

$$\frac{\partial\eta}{\partial\Psi} = -\sin\Psi\cos\Phi\,\eta_0 - \sin\Psi\sin\Phi\,\xi_0 - \cos\Psi\,\zeta_0\,, \tag{3.42}$$
$$\frac{\partial\zeta}{\partial\Psi} = \cos\Psi\cos\Phi\,\eta_0 + \cos\Psi\sin\Phi\,\xi_0 - \sin\Psi\,\zeta_0\,. \tag{3.43}$$

Comparing Eqns. (3.42) and (3.43) with Eqns. (3.40) and (3.38), respectively, and taking into account Eqns. (3.35) and (3.37) yields

$$\frac{\partial\eta}{\partial\Psi} = -\zeta = -\cos\Theta\,, \tag{3.44}$$
$$\frac{\partial\zeta}{\partial\Psi} = \eta = \sin\Theta\,\cos\varphi\,. \tag{3.45}$$

On the other hand, the derivatives given by Eqns. (3.44) and (3.45) can be obtained differentiating Eqns. (3.35) and (3.37) with respect to Ψ, i.e.,

$$\frac{\partial\eta}{\partial\Psi} = \cos\Theta\,\cos\varphi\,\frac{\partial\Theta}{\partial\Psi} - \sin\Theta\,\sin\varphi\,\frac{\partial\varphi}{\partial\Psi}\,, \tag{3.46}$$
$$\frac{\partial\zeta}{\partial\Psi} = -\sin\Theta\,\frac{\partial\Theta}{\partial\Psi}\,. \tag{3.47}$$

Combining Eqns. (3.44)–(3.47), the following expressions for the derivative $\partial\Theta/\partial\Psi$ and $\partial\varphi/\partial\Psi$ are obtained

$$\frac{\partial\Theta}{\partial\Psi} = -\cos\varphi \;, \tag{3.48}$$

$$\frac{\partial\varphi}{\partial\Psi} = \frac{\cos\Theta\,\sin\varphi}{\sin\Theta} \;. \tag{3.49}$$

Analogously, differentiating Eqns. (3.38) and (3.40) with respect to Φ, comparing the resulting equations with Eq. (3.39), and taking into account Eq. (3.36) leads to

$$\frac{\partial\eta}{\partial\Phi} = \xi\,\cos\Psi = \sin\Theta\,\sin\varphi\,\cos\Psi \;, \tag{3.50}$$

$$\frac{\partial\zeta}{\partial\Phi} = \xi\,\sin\Psi = \sin\Theta\,\sin\varphi\,\sin\Psi \;. \tag{3.51}$$

It follows from Eqns. (3.35) and (3.37) that

$$\frac{\partial\eta}{\partial\Phi} = \cos\Theta\,\cos\varphi\,\frac{\partial\Theta}{\partial\Phi} - \sin\Theta\,\sin\varphi\,\frac{\partial\varphi}{\partial\Psi} \;, \tag{3.52}$$

$$\frac{\partial\zeta}{\partial\Phi} = -\sin\Theta\,\frac{\partial\Theta}{\partial\Phi} \;. \tag{3.53}$$

Combining Eqns. (3.50)–(3.53), the following expressions for the derivatives $\partial\Theta/\partial\Psi$ and $\partial\varphi/\partial\Psi$ are obtained

$$\frac{\partial\Theta}{\partial\Phi} = -\sin\varphi\,\sin\Psi \;, \tag{3.54}$$

$$\frac{\partial\varphi}{\partial\Phi} = -\,\frac{\cos\Theta\,\cos\varphi\,\sin\Psi + \sin\Theta\,\cos\Psi}{\sin\Theta} \;. \tag{3.55}$$

The transformation of the spherical coordinates into Cartesian is performed as follows:

$$X = r\sin\Psi\,\cos\Phi \;, \tag{3.56}$$

$$Y = r\sin\Psi\,\sin\Phi \;, \tag{3.57}$$

$$Z = r\cos\Psi \;. \tag{3.58}$$

Therefore, using Eq. (3.31), the metric coefficients can be calculated in the following manner:

$$h_r = \sqrt{\sin^2\Psi\,\cos^2\Phi + \sin^2\Psi\,\sin^2\Phi + \cos^2\Psi} = 1 \;, \tag{3.59}$$

$$h_\Psi = \sqrt{r^2\,\cos^2\Psi\,\cos^2\Phi + r^2\,\cos^2\Psi\,\sin^2\Phi + r^2\,\sin^2\Psi} = r \;, \tag{3.60}$$

$$h_\Phi = \sqrt{r^2\,\sin^2\Psi\,\sin^2\Phi + r^2\,\sin^2\Psi\,\cos^2\Phi} = r\sin\Psi \;. \tag{3.61}$$

Substituting Eqns. (3.35)–(3.37), (3.48), (3.49), (3.54), (3.55), and (3.59)–(3.61) into Eq. (3.34), the following expression for the path-length derivative of the radiation intensity

in spherical coordinates is obtained:

$$\frac{d\,I}{d\,s} = \cos\Theta\,\frac{\partial\,I}{\partial\,r} + \frac{\sin\Theta\cos\varphi}{r}\,\frac{\partial\,I}{\partial\,\Psi} + \frac{\sin\Theta\sin\varphi}{r\,\sin\Psi}\,\frac{\partial\,I}{\partial\,\Phi} + \frac{\sin\Theta\,\cos\varphi}{r}\,(-\cos\varphi)\,\frac{\partial\,I}{\partial\,\Theta} +$$

$$\frac{\sin\Theta\cos\varphi}{r}\,\frac{\cos\Theta\,\sin\varphi}{\sin\Theta}\,\frac{\partial\,I}{\partial\,\varphi} + \frac{\sin\Theta\sin\varphi}{r\sin\Psi}\,(-\sin\varphi\,\sin\Psi)\,\frac{\partial\,I}{\partial\,\Theta} +$$

$$\frac{\sin\Theta\sin\varphi}{r\sin\Psi}\,\left(-\frac{\cos\Theta\,\cos\varphi\,\sin\Psi + \sin\Theta\,\cos\Psi}{\sin\Theta}\right)\,\frac{\partial\,I}{\partial\,\varphi}\,. \quad (3.62)$$

As a result, the general form of the radiative transfer equation, Eq. (3.27), in spherical coordinates is given by

$$\cos\Theta\,\frac{\partial\,I_{dif}}{\partial\,r} + \frac{\sin\Theta\cos\varphi}{r}\,\frac{\partial\,I_{dif}}{\partial\,\Psi} + \frac{\sin\Theta\sin\varphi}{r\,\sin\Psi}\,\frac{\partial\,I_{dif}}{\partial\,\Phi}$$

$$-\frac{\sin\Theta}{r}\,\frac{\partial\,I_{dif}}{\partial\,\Theta} - \frac{\sin\Theta\cos\varphi\cot\Psi}{r}\,\frac{\partial\,I_{dif}}{\partial\,\varphi} = -\,\alpha\,(I_{dif} - J_{ms} - J_{ss})\,, \quad (3.63)$$

where

$$\begin{aligned} I_{dif} &= I_{dif}(r,\Psi,\Phi,\Theta,\varphi)\,,\\ J_{ms} &= J_{ms}(r,\Psi,\Phi,\Theta,\varphi)\,,\\ J_{ss} &= J_{ss}(r,\Psi,\Phi,\Theta,\varphi)\,,\\ \alpha &= \alpha(r,\Psi,\Phi) \end{aligned}$$

In the selected coordinate system, the multiple scattering source function, J_{ms}, and the single scattering source function, J_{ss}, according to Eqns. (3.24) and (3.25), respectively, are given by

$$J_{ms}(r,\Psi,\Phi,\Theta,\varphi) = \frac{\varpi(r,\Psi,\Phi)}{4\pi}\,\int_0^{2\pi} d\hat{\varphi}\,\int_0^{\pi} d\hat{\Theta}\;p(r,\Psi,\Phi,\gamma)\,I_{dif}(r,\Psi,\Phi,\hat{\Theta},\hat{\varphi})\,\sin\hat{\Theta} \quad (3.64)$$

and

$$J_{ss}(r,\Psi,\Phi,\Theta,\varphi) = \frac{\varpi(r,\Psi,\Phi)}{4\pi}\,F_0\,p(r,\Psi,\Phi,\gamma_{\rm o})\exp\left(-\int_0^{s}\alpha(\hat{s})\,d\hat{s}\right)\,. \quad (3.65)$$

Here the scattering angles γ and $\gamma_{\rm o}$ are defined by

$$\gamma = \cos\Theta\cos\hat{\Theta} + \sin\Theta\sin\hat{\Theta}\cos(\varphi - \hat{\varphi}) \quad (3.66)$$

and

$$\gamma_{\rm o} = -\cos\Theta\cos\Psi + \sin\Theta\sin\Psi\cos\varphi\,, \quad (3.67)$$

respectively. The integration in Eq. (3.74) is performed along the direct solar beam and s denotes the total path-length along the beam.

3.4 Approximative differential operator in a spherical atmosphere

If a spherical shell medium is considered, all atmospheric characteristics and, therefore, the intensity of radiation do not depend on global azimuth angle Φ. Hence, the third term in Eq. (3.63) containing $\partial/\partial\Phi$ vanishes, and Eq. (3.63) leads to the differential radiative transfer equation for a spherical planetary atmosphere introduced by *Lenoble and Sekera* [1961] and independently by *Sobolev and Minin* [1962]:

$$\cos\Theta\,\frac{\partial\,I_{dif}}{\partial\,r} + \frac{\sin\Theta\cos\varphi}{r}\,\frac{\partial\,I_{dif}}{\partial\,\Psi} - \frac{\sin\Theta}{r}\,\frac{\partial\,I_{dif}}{\partial\,\Theta}$$

$$- \frac{\sin\Theta\cos\varphi\cot\Psi}{r}\,\frac{\partial\,I_{dif}}{\partial\,\varphi} = -\,\alpha\,(I_{dif} - J_{ms} - J_{ss})\;. \quad (3.68)$$

This form of the radiative transfer equation has been also used in the extended Sobolev method discussed in [*Wilson and Sen*, 1980a,b].

Considering each spherical shell layer to be horizontal-homogeneously illuminated by the direct solar radiance, i.e., the intensity of direct radiation given by Eq. (3.21) to be independent of the position of point $\mathbf{r}$ with respect to the Sun ($I_{dir}(\mathbf{r},\mathbf{e}_s) = I_{dir}(r,\mathbf{e}_s)$), the derivative $\partial/\partial\Psi$ disappears and the following expression for the corresponding approximative differential operator is appropriate:

$$\frac{d}{d\,s} = \cos\Theta\,\frac{\partial}{\partial\,r} - \frac{\sin\Theta}{r}\,\frac{\partial}{\partial\,\Theta} - \frac{\sin\Theta\cos\varphi\cot\Psi}{r}\,\frac{\partial}{\partial\,\varphi}\;. \quad (3.69)$$

The radiative transfer equation employing this approximate differential operator has been used by *Balluch* [1996] to calculate photolysis rates and solar heating in a spherical planetary atmosphere.

If an atmosphere is isotropically illuminated, the diffuse radiation field becomes azimuthally independent and the following approximation for the differential operator is obtained:

$$\frac{d}{d\,s} = \cos\Theta\,\frac{\partial}{\partial\,r} - \frac{\sin\Theta}{r}\,\frac{\partial}{\partial\,\Theta}\;. \quad (3.70)$$

In this case the radiance is a function of two variables only, namely, r and Θ. It is the radiative transfer equation with the differential operator defined by (3.70), which was used to solve the radiative transfer problem in stellar atmospheres, as well as neutron transport and heat transfer problems [*Sen and Wilson*, 1990].

3.5 Plane-parallel and pseudo-spherical atmospheres

A substantial simplification of the radiative transfer equation can be achieved considering an atmosphere consisting of plane-parallel layers (*plane-parallel atmosphere*) instead of a

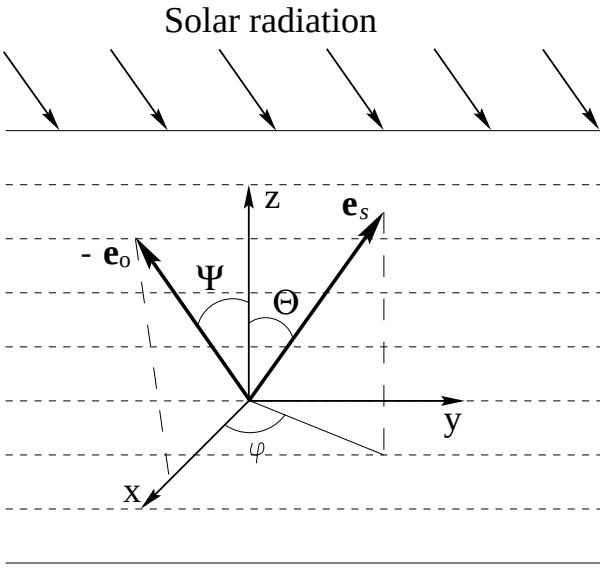

Figure 3.3: Definition of directional coordinates in a plane-parallel atmosphere.

spherical atmosphere. The simplest way to obtain the solution of the radiative transfer equation is a one-dimensional plane-parallel radiative transfer model, see, for example, [*Dave and Mateer*, 1967; *Meier et al.*, 1982; *Stamnes et al.*, 1988; *Rozanov et al.*, 1997]. In such models the spatial position of a point in the atmosphere is defined only by its altitude, whereas in three-dimensional plane-parallel radiative transfer models, see, for example, [*Evans*, 1998], the position of a point in the atmosphere is commonly defined by three Cartesian coordinates. The coordinates which are commonly used in a plane-parallel atmosphere are shown in Fig 3.3. The z-axis points upwards and z-coordinate corresponds to the altitude, $z = 0$ refer to the bottom of the atmosphere and, hence, $z = r - R$, where R is the Earth's radius. The x-axis is commonly selected to set the azimuth angle of the direct solar beam to zero, i.e., $\varphi_o = 0$.

Since the variables Θ and φ in a plane-parallel atmosphere do not depend on the position in the atmosphere, the angular redistribution terms in Eq. (3.34) disappear. The metric coefficients, h_i, are equal to the unity when the Cartesian coordinates are used. Thus, the following expression for the path-length derivative of diffuse radiation intensity in a plane-parallel atmosphere is obtained:

$$\frac{d\,I_{dif}}{d\,s} = \sin\Theta\cos\varphi\,\frac{\partial\,I_{dif}}{\partial\,x} + \sin\Theta\sin\varphi\,\frac{\partial\,I_{dif}}{\partial\,y} + \cos\Theta\,\frac{\partial\,I_{dif}}{\partial\,z}\,. \tag{3.71}$$

Considering horizontally homogeneous atmosphere, all atmospheric characteristics and, therefore, the intensity of diffuse radiation become independent of the position in a horizontal layer. This leads to one-dimensional plane-parallel atmosphere and the following radiative transfer equation Eq. (3.27) is appropriate:

$$\cos\Theta\,\frac{d\,I_{dif}(z,\Theta,\varphi)}{d\,z} = -\,\alpha(z)\,(I_{dif}(z,\Theta,\varphi) - J_{ms}(z,\Theta,\varphi) - J_{ss}(z,\Theta,\varphi))\,, \tag{3.72}$$

where the multiple scattering source function, J_{ms}, and the single scattering source function, J_{ss}, are given by

$$J_{ms}(z,\Theta,\varphi) = \frac{\varpi(z)}{4\pi} \int_0^{2\pi} d\hat{\varphi} \int_0^{\pi} d\hat{\Theta}\; p(z,\Theta,\varphi,\hat{\Theta},\hat{\varphi})\, I_{dif}(z,\hat{\Theta},\hat{\varphi})\, \sin\hat{\Theta} \tag{3.73}$$

and

$$J_{ss}(z,\Theta,\varphi,\Psi) = \frac{\varpi(z)}{4\pi}\, F_0\, p(z,\Theta,\varphi,\Psi) \exp\left(- \int_0^{z_t} \frac{\alpha(\hat{z})}{\cos\Psi}\, d\hat{z} \right) , \tag{3.74}$$

respectively. Here, z_t refers to the top of the atmosphere. Since the radiative transfer equation in a plane-parallel atmosphere is always solved at one specified solar zenith angle, the dependence of J_{ss} on Ψ in Eq. (3.74) is parametrical and does not have to be included in the radiative transfer equation.

The accuracy of the radiative transfer calculations at large solar zenith angles (larger than about 85°) can be substantially improved considering a *pseudo-spherical atmosphere* instead of a plane-parallel one. This means that a plane-parallel atmosphere is considered to be horizontal-homogeneously illuminated by direct solar radiance, which is attenuated as in a spherical atmosphere. Thus, Eqns. (3.72) and (3.73) for a pseudo-spherical atmosphere remain unchanged, whereas the single scattering source function $J_{ss}(z,\Theta,\varphi)$ is calculated in a spherical atmosphere, i.e.

$$J_{ss}(z,\Theta,\varphi) = \frac{\varpi(z)}{4\pi}\, F_0\, p(z,\Theta,\varphi,\Psi) \exp\left(- \int_0^{s_t} \alpha(\hat{s})\, d\hat{s} \right) . \tag{3.75}$$

Here, integration is to be performed along the direct solar beam and s_t, hence, denotes the full length of the integration line from the selected point to the top of the atmosphere along the beam. Similar to plane-parallel atmosphere, the radiative transfer equation in a pseudo-spherical atmosphere is solved for one selected solar zenith angle at a time.

In recent times, pseudo-spherical radiative transfer models have commonly been used to compute fast, and relatively accurately, the radiation field in the Earth's atmosphere as well as applied to a wide range of other problems concerning the remote sensing of the Earth's atmosphere, see, for example, [*DeLuisi and Mateer*, 1971; *Klenk et al.*, 1982; *Ridley et al.*, 1984; *Mateer and DeLuisi*, 1992; *McPeters et al.*, 1996; *Rozanov et al.*, 2000b].

Chapter 4

Numerical methods to solve the radiative transfer equation in a spherical atmosphere

4.1 Radiative transfer models overview

A radiative transfer model employed for the interpretation of the measurements of solar radiation scattered in the atmosphere or reflected from the Earth's surface performed by satellite or ground-based instruments in an arbitrary viewing geometry has to incorporate the following characteristics:

- determine accurate multiple–scattered radiation in a spherical atmosphere for all relevant solar zenith angles and viewing geometries;
- perform well over a wide range of phase functions;
- allow optical characteristics and phase functions of the medium to vary spatially;
- be computationally efficient.

Some methods to solve the spherical radiative transfer equation are discussed below. The possibility to employ, in a spherical atmosphere, the well-known methods which were effectively used in a plane-parallel medium is also discussed.

4.1.1 Monte Carlo method

A well–known method, which complies with most of the requirements formulated above, is the Monte Carlo technique [*Marchuk et al.*, 1980]. In a Monte Carlo simulation the intensity of radiation is determined statistically by following a large number of individual photon trajectories through the atmosphere. For atmospheric applications, the backward Monte Carlo method is commonly used. In this method the photons are started from the detector and their path is followed backward to the point where they leave the atmosphere

toward the Sun. This technique is very effective when the receiver has a narrow field of view because all simulated photons contribute to the signal, whereas in a forward simulation only a small fraction of the photons coming from the Sun reach the instrument. However, there are two serious disadvantages of the Monte Carlo method: (1) it requires long running-times to achieve reasonable accuracy and (2) the accuracy of the backward Monte Carlo method is poor when the medium is optically thick or has a weak absorption. Using the quasi Monte Carlo technique discussed in [*O'Brien*, 1992], the calculation time can be significantly reduced, but the difficulty of the backward Monte Carlo integration in an optically thick or week absorbing atmosphere is not eliminated. Applications of the Monte Carlo method for radiation field calculations in a spherical atmosphere can be found in [*Collins et al.*, 1972; *Kondratjev et al.*, 1977; *Oikarinen et al.*, 1999].

4.1.2 Methods involving azimuthal Fourier series expansion

Most of the methods which are successfully used for radiative transfer calculations in a plane-parallel atmosphere, such as "Spherical Harmonics", "Discrete Ordinate", "Finite Difference ", etc. (the methods are discussed in detail, for example, in [*Lenoble*, 1985]), involve the expansion of the intensity and the scattering phase function in Fourier series as follows:

$$I_{dif}(z,\Theta,\varphi) = \sum_{k=0}^{K} (2-\delta_{0,k})\, I_{dif}^{(k)}(z,\Theta)\, \cos k\varphi \tag{4.1}$$

and

$$p(z,\Theta,\varphi,\hat{\Theta},\hat{\varphi}) = \sum_{k=0}^{K} (2-\delta_{0,k})\, p^{(k)}(z,\Theta,\hat{\Theta})\, \cos k(\varphi-\hat{\varphi})\ . \tag{4.2}$$

Here, K is the total number of the Fourier terms in the expansion and δ_{0k} is the Kronecker symbol defined as

$$\begin{cases} \delta_{0,k} = 0, k \neq 0 \\ \delta_{0,k} = 1, k = 0 \end{cases} \tag{4.3}$$

Combining Eqns. (3.73), (4.1), and (4.2) the Fourier expansion coefficients for the multiple scattering source function in a plane-parallel atmosphere can be obtained as follows:

$$J_{ms}^{(k)}(z,\Theta) = \frac{\varpi(z)}{4\pi} \int_0^{2\pi} d\hat{\varphi} \int_0^{\pi} d\hat{\Theta}\, p^{(k)}(z,\Theta,\hat{\Theta})\, I_{dif}^{(k)}(z,\hat{\Theta})\, \sin\hat{\Theta}\ , \quad k=0,\ldots,K\ . \tag{4.4}$$

The Fourier expansion coefficients for the single scattering source function are obtained from Eqns. (3.74) and (4.2) taking into account that for the direct solar radiation $\hat{\Theta} = \pi - \Psi$ and $\hat{\varphi} = 0$ are appropriate:

$$J_{ss}^{(k)}(z,\Theta,\Psi) = \frac{\varpi(z)}{4\pi} F_0\, p^{(k)}(z,\Theta,\Psi) \exp\left(- \int_0^{z_t} \frac{\alpha(\hat{z})}{\cos\Psi}\, d\hat{z} \right)\ , \quad k=0,\ldots,K\ . \tag{4.5}$$

Using this approach, the radiative transfer equation, as given by Eq. (3.72), for an arbitrarily selected solar zenith angle can be split into the system of independent equations for each Fourier coefficient:

$$\cos\Theta \frac{d\, I_{dif}^{(k)}(z,\Theta)}{d\, z} = -\,\alpha(z)\,(I_{dif}^{(k)}(z,\Theta) - J_{ms}^{(k)}(z,\Theta) - J_{ss}^{(k)}(z,\Theta))\;, \quad k = 0,\ldots,K\;. \quad (4.6)$$

In a spherical atmosphere, the cosine Fourier expansion, as given by Eqns. (4.1) and (4.2), can be used only if the dependence of the intensity of the diffuse radiation on global azimuth angle, Φ, is neglected. Thus, in this case, the radiative transfer equation given by Eq. (3.68) is appropriate. Combining Eqns. (3.68), (4.1), (4.4), and (4.5) results in the following system of coupled differential equations:

$$\cos\Theta \frac{\partial\, I_{dif}^{(k)}}{\partial\, r} + \frac{\sin\Theta}{r}\left[\frac{1}{2}\frac{\partial\, I_{dif}^{(k-1)}}{\partial\,\Psi} + \frac{1}{2-\delta_{0,k}}\frac{\partial\, I_{dif}^{(k+1)}}{\partial\,\Psi}\right]$$

$$-\frac{\sin\Theta}{r}\frac{\partial\, I_{dif}^{(k)}}{\partial\,\Theta} - \frac{\sin\Theta\cot\Psi}{r}\left[\frac{k-1}{2}\, I_{dif}^{(k-1)} + \frac{k+1}{2-\delta_{0,k}}\, I_{dif}^{(k+1)}\right]$$

$$= -\,\alpha\,(I_{dif}^{(k)} - J_{ms}^{(k)} - J_{ss}^{(k)})\;, \quad k = 0,\ldots,K\;, \quad (4.7)$$

where $J_{ms}^{(k)}$ and $J_{ss}^{(k)}$ are the Fourier expansion coefficients for multiple scattering and single scattering source functions in a spherical atmosphere. The spherical Fourier expansion coefficients are obtained analogously to them in a plane-parallel atmosphere (Eqns. (4.4) and (4.5)) from Eqns. (3.64) and (3.65), respectively. As clearly seen, the equation for the k-th Fourier coefficients contains also the $(k-1)$-th and the $(k+1)$-th coefficients of the Fourier expansion for the intensity. This means that each equation has to be solved in combination with two neighboring equations, i.e., the system of the radiative transfer equations for Fourier coefficients can not be split into independent equations any more.

Since the possibility to solve the radiative transfer equation for each Fourier coefficient separately is the main advantage of the above mentioned methods, it is reasonable to extend them for a spherical atmosphere only if an azimuthal independent radiation field and no external anisotropic illumination is considered [*Sen and Wilson*, 1990]. Thus, these methods can be used to perform radiative transfer calculations in stellar atmospheres, as well as neutron transport and heat transfer calculations. Although several advanced methods have been developed during the past years [*Madkour*, 1996; *Abulwafa and Attia*, 1997], they can not be applied for the radiative transfer calculations in planetary atmospheres as well.

4.1.3 Moment approach

Another well–known method for solving the radiative transfer equation in a spherical shell planetary atmosphere is the "Moment approach" [*Sobolev*, 1975], which was introduced in

[*Sobolev*, 1943] for a plane-parallel atmosphere and extended in [*Sobolev and Minin*, 1962] for a spherical shell atmosphere. The basic idea of this method is solving the radiative transfer equation for the moments of the intensity instead for the intensity itself. The moments are defined by

$$M_0(r,\Psi) = \frac{1}{4\pi}\int_0^{2\pi} d\varphi \int_0^{\pi} d\Theta\, \sin\Theta\, I(r,\Psi,\Theta,\varphi)\ , \tag{4.8}$$

$$M_1(r,\Psi) = \frac{1}{4\pi}\int_0^{2\pi} d\varphi \int_0^{\pi} d\Theta\, \sin\Theta\, \cos\Theta\, I(r,\Psi,\Theta,\varphi)\ , \tag{4.9}$$

$$M_2(r,\Psi) = \frac{1}{4\pi}\int_0^{2\pi} d\varphi \int_0^{\pi} d\Theta\, \sin^2\Theta\, \cos\varphi\, I(r,\Psi,\Theta,\varphi)\ . \tag{4.10}$$

The zeroth moment, M_0, is the mean intensity of the diffuse radiation, the first moment, M_1, is proportional to the vertical flux of the diffuse radiation, and the second moment, M_2, is proportional to the flux of the diffuse radiation in the direction $\varphi = 0$ in a horizontal plane.

In moment approach, only the first two terms of the Legendre expansion of the phase function are considered, i.e., the scattering phase function is given by

$$p(\gamma) = 1 + \beta\, \cos\gamma\ . \tag{4.11}$$

Combining Eqns. (3.64)–(3.67) and (4.8)–(4.10), the following formula for the total source function can be obtained:

$$\begin{aligned} J = {} & \varpi\,(M_0 + \beta\, M_1 \cos\Theta + \beta\, M_2 \sin\Theta\cos\varphi) \\ & + \frac{\varpi(z)}{4\pi}\, F_0\,(1 - \beta\, \cos\Theta + \beta\, \sin\Theta \sin\Psi \cos\varphi)\ e^{-\tau}\ , \end{aligned} \tag{4.12}$$

where τ is the optical depth defined by

$$\tau = \int_0^s \alpha(\hat{s})\, d\hat{s}\ . \tag{4.13}$$

According to [*Sobolev*, 1975], the following system of differential equations for the moments can be obtained:

$$\frac{\partial M_1}{\partial r} + \frac{2}{r}\, M_1 + \frac{1}{r}\, \frac{\partial M_2}{\partial \Psi} + \frac{\cot\Psi}{r}\, M_2 = -\,\alpha\,(1-\varpi)\, M_0 + \alpha\, \frac{\varpi}{4\pi}\, F_0\, e^{-\tau}\ , \tag{4.14}$$

$$(3 - \varpi\,\beta)\, M_1 = -\,\frac{1}{\alpha}\, \frac{\partial M_0}{\partial r} - \frac{\varpi}{4\pi}\, F_0\, e^{-\tau}\ , \tag{4.15}$$

$$(3 - \varpi\,\beta)\, M_2 = -\,\frac{1}{\alpha\, r}\, \frac{\partial M_0}{\partial \Psi} + \frac{\varpi}{4\pi}\, F_0\, e^{-\tau}\ . \tag{4.16}$$

The equations (4.14)–(4.16) were derived multiplying the spherical radiative transfer equation, as given by Eq. (3.68), successively by

$$\frac{1}{4\pi}\,\sin\Theta\,d\Theta\,d\varphi\;,\quad \frac{1}{4\pi}\,\sin\Theta\,\cos\Theta\,d\Theta\,d\varphi\;,\quad \text{and}\quad \frac{1}{4\pi}\,\sin^2\Theta\,\cos\varphi\,d\Theta\,d\varphi$$

and integrating over all directions. To obtain Eqns. (4.14)–(4.16) from Eq. (3.68), the following approximative relation was used:

$$\frac{1}{4\pi}\int_0^{2\pi} d\varphi \int_0^{\pi} d\Theta\,\sin\Theta\,\cos^2\Theta\,I(r,\Psi,\Theta,\varphi) = \frac{1}{3}\,M_0\;, \tag{4.17}$$

which is commonly referred to as the Eddington approximation.

Solving the system of differential equations (4.14)–(4.16) all three moments can be found and, therefore, the source function, as given by Eq.(4.12), can be calculated. Once the source function is known, the integro-differential radiative transfer equation, Eq. (3.68), becomes a partial differential equation which can be solved using standard numerical methods.

The moment approach has been used by *Smokty* [1986] for simulations of outgoing radiance at line-of-sights having their tangent point near the terminator. The method is also known as the "Sobolev method" [*Sen and Wilson*, 1990]. The main disadvantages of the method are (i) a simplified consideration of the azimuthal dependence of the diffuse radiation field (see Eqns. (4.11) and (4.12)), (ii) employing the Eddington approximation, as defined by Eq. (4.17), and (iii) approximate boundary conditions.

4.1.4 Further improvements to the Sobolev method

Three-stream moment method

The Sobolev method was further developed in [*Wilson et al.*, 1980; *Wilson and Sen*, 1980a,b]. In addition to Sobolev's moments, as defined by Eqns. (4.8)–(4.10), six new

moments were introduced as follows:

$$M_3(r,\Psi) = \frac{1}{4\pi}\int_0^{2\pi} d\varphi \int_0^{\pi} d\Theta\, \sin\Theta\, \cos^2\Theta\, I(r,\Psi,\Theta,\varphi)\;, \tag{4.18}$$

$$M_4(r,\Psi) = \frac{1}{4\pi}\int_0^{2\pi} d\varphi \int_0^{\pi} d\Theta\, \sin\Theta\, \cos^3\Theta\, I(r,\Psi,\Theta,\varphi)\;, \tag{4.19}$$

$$M_5(r,\Psi) = \frac{1}{4\pi}\int_0^{2\pi} d\varphi \int_0^{\pi} d\Theta\, \sin^2\Theta\, \cos\Theta\, \cos\varphi\, I(r,\Psi,\Theta,\varphi)\;, \tag{4.20}$$

$$M_6(r,\Psi) = \frac{1}{4\pi}\int_0^{2\pi} d\varphi \int_0^{\pi} d\Theta\, \sin^2\Theta\, \cos^2\Theta\, \cos\varphi\, I(r,\Psi,\Theta,\varphi)\;, \tag{4.21}$$

$$M_7(r,\Psi) = \frac{1}{4\pi}\int_0^{2\pi} d\varphi \int_0^{\pi} d\Theta\, \sin^3\Theta\, \cos^2\varphi\, I(r,\Psi,\Theta,\varphi)\;, \tag{4.22}$$

$$M_8(r,\Psi) = \frac{1}{4\pi}\int_0^{2\pi} d\varphi \int_0^{\pi} d\Theta\, \sin^3\Theta\, \sin^2\varphi\, I(r,\Psi,\Theta,\varphi)\;. \tag{4.23}$$

Following [*Wilson and Sen*, 1980a], the spherical radiative transfer equation, as given by Eq. (3.68), results in the following system of differential equations for nine moments:

$$\frac{\partial M_1}{\partial r} + \frac{2}{r} M_1 + \frac{1}{r}\frac{\partial M_2}{\partial \Psi} + \frac{\cot\Psi}{r} M_2 = -\alpha\,(1-\varpi)\, M_0 + \alpha\,\frac{\varpi}{4\pi}\, F_0\, e^{-\tau}\;, \tag{4.24}$$

$$\frac{\partial M_3}{\partial r} + \frac{1}{r}\,(3\,M_3 - M_0) + \frac{1}{r}\frac{\partial M_5}{\partial \Psi} + \frac{\cot\Psi}{r} M_5 = \\ -\,\alpha\, M_1 + \alpha\left[\frac{\varpi\,\beta\, M_1}{3} - \frac{\varpi\,\beta\,\cos\Psi\, F_0\, e^{-\tau}}{4\pi}\right]\;, \tag{4.25}$$

$$\frac{\partial M_4}{\partial r} + \frac{1}{r}\,(4\,M_4 - 2\,M_1) + \frac{1}{r}\frac{\partial M_6}{\partial \Psi} + \frac{\cot\Psi}{r} M_6 = \\ -\,\alpha\, M_3 + \alpha\left[\frac{\varpi\, M_0}{3} + \frac{\varpi\, F_0\, e^{-\tau}}{12\pi}\right]\;, \tag{4.26}$$

$$\frac{\partial M_5}{\partial r} + \frac{3}{r} M_5 + \frac{1}{r}\frac{\partial M_7}{\partial \Psi} + \frac{\cot\Psi}{r}\,(M_7 - M_8) = \\ -\,\alpha\, M_2 + \alpha\left[\frac{\varpi\,\beta\, M_2}{3} + \frac{\varpi\,\beta\,\sin\Psi\, F_0\, e^{-\tau}}{12\pi}\right]\;. \tag{4.27}$$

In order to complete the system, five additional equations have to be found. This can be achieved employing a three-stream approximation for the radiation field [*Wilson and Sen*, 1980a] :

$$I(r,\Psi,\Theta,\varphi) = \begin{cases} I_1(r,\Psi) + f(r,\Psi)\,\cos\varphi, & \mu_r > \cos\Theta \geqslant 1\ , \\ I_2(r,\Psi) + f(r,\Psi)\,\cos\varphi, & 0 > \cos\Theta \geqslant \mu_r\ , \\ I_3(r,\Psi) + f(r,\Psi)\,\cos\varphi, & -1 \geqslant \cos\Theta \geqslant 0\ , \end{cases} \tag{4.28}$$

where

$$\mu_r = \sqrt{1 - \left(\frac{r}{R}\right)^2}\ . \tag{4.29}$$

Here, R denotes the Earth's radius. Combining Eqns. (4.8)–(4.10) and (4.18)–(4.23) with Eq. (4.28) and excluding I_1, I_2, and I_3 from the resulting system the following additional equations are obtained:

$$2(2\,M_4 - M_1) = \mu_r(3\,M_3 - M_0)\ , \tag{4.30}$$

$$M_2 = \frac{\pi}{8}\,f\ , \tag{4.31}$$

$$M_5 = 0\ , \tag{4.32}$$

$$M_6 = \frac{\pi}{32}\,f\ , \tag{4.33}$$

$$M_7 = \frac{1}{2}(M_0 - M_3)\ , \tag{4.34}$$

$$M_8 = \frac{1}{2}(M_0 - M_3)\ . \tag{4.35}$$

The relation given by Eq. (4.30) is called the generalized Eddington approximation.

Solving Eqns. (4.24)–(4.27) in conjuction with Eqns. (4.30)–(4.35) all moments can be found. The solution is then obtained in the exact same manner as in the Sobolev method.

Thus, in the discussed method, an essential improvement has been achieved using the generalized Eddington approximation and revised boundary conditions but the simplified consideration of azimuthal dependence of the scattering phase function, as given by Eq. (4.11), has been retained.

Moment method employing Cutteridge–Devyatov polynomials

In a new revision of the moment approach discussed by *Solovjev* [1992] the radiance is developed in Cutteridge–Devyatov polynomials using the moments of the diffuse radiation as expansion coefficients:

$$I = \sum_{i=0}^{n-1} \tilde{M}_i\,\frac{d\,\mathcal{P}_i}{d\,\cos\Theta}\ . \tag{4.36}$$

Here, n is the total number of the moments which can be selected arbitrary and the moments, $\tilde{M}_i$, are defined by

$$\tilde{M}_i = \int_0^\pi \sin\Theta \, \cos^i\Theta \, I \, d\Theta \, . \tag{4.37}$$

The systems of the Cutteridge–Devyatov polynomials, $\mathcal{P}_i$, have distinctive forms for different n and are given by

$$\mathcal{P}_i = \sum_{m=0}^{n-1} c_{im} \, \cos^{m+1}\Theta, \quad i = 0, \ldots, n-1 \, . \tag{4.38}$$

Here, the coefficients c_{im} are constant for each selected i and m.

Similar to the Sobolev method, the radiative transfer equation results, employing this technique, in the system of n differential equation for $n+1$ moments. In this case, however, the Eddington approximation used to complete the system of the differential equations can be replaced by the following exact relation:

$$\tilde{M}_n = \int_0^\pi \sin\Theta \, \left[\sum_{i=0}^{n-1} \tilde{M}_i \, \frac{d\,\mathcal{P}_i}{d\,\cos\Theta} \right] \, d\Theta \, . \tag{4.39}$$

Although, this approach was introduced by *Solovjev* [1992] for a plane-parallel isotropically scattering atmosphere, it can be easily extended for an anisotropically scattering medium employing the expansion of the scattering phase function and the diffuse radiation field in Fourier series with an arbitrary number of azimuthal expansion terms. Thus, all disadvantages of the Sobolev method are eliminated. However, our attempts to extend this method for a spherical medium failed for the following reasons. The determination of the zeroth moment with an appropriate accuracy from Eq. (4.39) was found to require very high accuracy of the other moments. The more moments in the radiance development series are used, the higher the accuracy required for their calculation. Since in a spherical atmosphere, unlike the plane-parallel case, the system of equations for the moments has to be solved iteratively, a certain inaccuracy of moments determination is inevitable and the iteration scheme fails to converge.

4.1.5 Other methods

A new approach to the solution of the integral radiative transfer equation in a spherical shell atmosphere employing the Gauss–Seidel iteration scheme has been suggested recently by *Herman et al.* [1994]. The basic idea of this method is avoiding the calculation of the radiation field throughout the entire hemisphere employing instead a conical boundary surrounding the zenith direction along which the solution is desired. Approximate solutions are found along this boundary, and these solutions are used in an interpolation scheme to obtain the radiation field along the zenith direction. Thus, using this technique the

intensities are found at a discrete set of directions at discrete height levels along a selected radial line in the atmosphere. The main approximation which has to be employed in order to obtain the approximate solutions along the cone is that the ratio of multiple to single scattering terms outside the cone is constant along any shell. Thus, this approach limits the model to cases in which the single scattering term is not zero, i.e., the solar zenith angle has to be less than 90°. Furthermore, according to [*Lenoble*, 1985], the Gauss–Seidel iteration scheme is computationally inefficient for an optically thick atmosphere.

There are also radiative transfer models, which use some approximations enabling the mean intensity in a spherical atmosphere to be calculated efficiently. For example, in [*Anderson*, 1983] the radiation field was assumed to be isotropic, in [*Balluch*, 1996] the variation of the solar zenith angle with the spatial coordinates was neglected, and in [*Dahlback and Stamnes*, 1991] the azimuthally averaged radiative transfer equation was solved iteratively considering the spherical terms as a perturbation. Such models, however, can not reproduce the angular dependence of the radiance accurately enough.

A new Combining Differential–Integral approach involving the Picard Iterative approximation (CDIPI) was recently developed by *Rozanov et al.* [2001]. This approach involves the Characteristics method [*Currant and Hilbert*, 1962] and the Picard iterative approximation [*Hirsh and Smale*, 1974] to solve the radiative transfer equation in a spherical planetary atmosphere. The theoretical basis of the method is discussed in the next section. The CDIPI radiative transfer model which employs this approach to calculate the radiation field in a spherical planetary atmosphere is discussed in detail in Section 7.

4.2 Characteristics method

Taking the requirements formulated in Section 4.1 into account, only the full differential operator is suitable to solve the radiative transfer equation in a spherical planetary atmosphere accurately enough. As discussed in Section 3.3, the full differential operator in spherical coordinates (see Fig. 3.2) is given by

$$\frac{d}{d\,s} = \cos\Theta\,\frac{\partial}{\partial\,r} + \frac{\sin\Theta\cos\varphi}{r}\,\frac{\partial}{\partial\,\Psi} + \frac{\sin\Theta\sin\varphi}{r\,\sin\Psi}\,\frac{\partial}{\partial\,\Phi}$$

$$- \frac{\sin\Theta}{r}\,\frac{\partial}{\partial\,\Theta} - \frac{\sin\Theta\cos\varphi\cot\Psi}{r}\,\frac{\partial}{\partial\,\varphi}\,. \quad (4.40)$$

Therefore, a first-order partial differential equation for the intensity of diffuse radiation as a function of five variables r, Ψ, Φ, Θ, and φ has to be solved. One of the well-known methods to solve such an equation is the so-called "Characteristics method" [*Currant and Hilbert*, 1962]. This method performs the conversion of the resulting first-order partial differential equation into an integral equation by integrating its two sides along a characteristic. If no refraction effects are considered, the characteristics are straight lines defined by direction cosines $\xi_1 = \cos\varphi\sin\Theta$, $\xi_2 = \sin\varphi\sin\Theta$, and $\xi_3 = \cos\Theta$. The angle variables Θ and φ are assumed to be functions of Ψ and Φ. Beginning at the boundary and performing

an integration along a characteristic, the following integral form of the radiative transfer equation (3.27) can be obtained:

$$I_{dif}(r,\Psi,\Phi,\Theta,\varphi) = I_0(r,\Psi,\Phi,\Theta,\varphi) + \mathrm{L}_\mathrm{s}^\mathrm{sp}\, J(\tilde{r},\tilde{\Psi},\tilde{\Phi},\tilde{\Theta},\tilde{\varphi}) \;, \tag{4.41}$$

where $I_0(r,\Psi,\Phi,\Theta,\varphi)$ is defined by the boundary conditions. The integral operator $\mathrm{L}_\mathrm{s}^\mathrm{sp}$ is given by

$$\mathrm{L}_\mathrm{s}^\mathrm{sp} \equiv \int_0^{s_\mathrm{c}} ds\, \alpha(s)\, \exp\left(- \int_0^s \alpha(\tilde{s})\, d\tilde{s} \right) \;, \tag{4.42}$$

where s is the path-length along the characteristic and s_c the full length of the characteristic. Variables $\tilde{r}$, $\tilde{\Psi}$, $\tilde{\Phi}$, $\tilde{\Theta}$, and $\tilde{\varphi}$ are assumed to be functions of s.

The characteristics method was first applied for radiative transfer calculations in a spherical planetary atmosphere in [*Germogenova et al.*, 1969], where the single–scattered solar radiance was calculated for limb viewing geometry. Mathematical details on this application can be found in [*Sushkevich et al.*, 1990].

Equation (4.41) is only a formal solution of the differential equation (3.27), because the source function $J(\tilde{r},\tilde{\Psi},\tilde{\Phi},\tilde{\Theta},\tilde{\varphi})$ is a functional of the intensity of the diffuse radiation $I_{dif}(\tilde{r},\tilde{\Psi},\tilde{\Phi},\hat{\Theta},\hat{\varphi})$ (see Eqns. (3.23)–(3.26)):

$$J(\tilde{r},\tilde{\Psi},\tilde{\Phi},\tilde{\Theta},\tilde{\varphi}) = \mathrm{L}_\mathrm{a}\, I_{dif}(\tilde{r},\tilde{\Psi},\tilde{\Phi},\hat{\Theta},\hat{\varphi}) + J_{ss}(\tilde{r},\tilde{\Psi},\tilde{\Phi},\tilde{\Theta},\tilde{\varphi}) \;, \tag{4.43}$$

where L_a is an angular integration operator defined by

$$\mathrm{L}_\mathrm{a} \equiv \frac{\omega(\tilde{\mathbf{r}})}{4\pi} \int_0^{2\pi} d\,\hat{\varphi} \int_0^{\pi} d\,\hat{\Theta}\, \sin\hat{\Theta}\; p(\tilde{\mathbf{r}},\tilde{\Theta},\tilde{\varphi},\hat{\Theta},\hat{\varphi}) \;. \tag{4.44}$$

Here, $\omega(\tilde{\mathbf{r}})$ is the single scattering albedo and $p(\tilde{\mathbf{r}},\tilde{\Theta},\tilde{\varphi},\hat{\Theta},\hat{\varphi})$ is the scattering phase function. Equation (4.41), hence, can be rewritten as follows:

$$I_{dif}(r,\Psi,\Phi,\Theta,\varphi) = \mathfrak{I}(r,\Psi,\Phi,\Theta,\varphi) + \mathrm{L}_\mathrm{s}^\mathrm{sp}\, \mathrm{L}_\mathrm{a}\, I_{dif}(\tilde{r},\tilde{\Psi},\tilde{\Phi},\hat{\Theta},\hat{\varphi}) \;, \tag{4.45}$$

where

$$\mathfrak{I}(r,\Psi,\Phi,\Theta,\varphi) = I_0(r,\Psi,\Phi,\Theta,\varphi) + \mathrm{L}_\mathrm{s}^\mathrm{sp}\, J_{ss}(\tilde{r},\tilde{\Psi},\tilde{\Phi},\tilde{\Theta},\tilde{\varphi}) \;. \tag{4.46}$$

Equation (4.45) is a linear integral operator equation which can be solved using an iterative approach. The commonly used equation for the iterative scheme known as "Picard iterative approximation" [*Hirsh and Smale*, 1974] is given by:

$$I_{dif}^{(n)}(r,\Psi,\Phi,\Theta,\varphi) = \mathfrak{I}(r,\Psi,\Phi,\Theta,\varphi) + \mathrm{L}_\mathrm{s}^\mathrm{sp}\, \mathrm{L}_\mathrm{a}\, I_{dif}^{(n-1)}(\tilde{r},\tilde{\Psi},\tilde{\Phi},\hat{\Theta},\hat{\varphi}) \;. \tag{4.47}$$

This iterative approach has been used for radiative transfer calculations in a plane-parallel three-dimensional atmosphere in such radiative transfer models as SHDOM [*Evans*, 1998] and PI approximation [*Kuo et al.*, 1996].

In order to perform the first iteration, an initial guess is required. One way to choose an initial guess is the Successive Order of Scattering (SOS) method, which uses the single–scattered radiance as an initial estimate. As pointed out by *O'Brien* [1992], the SOS method is logically equivalent to the simulation of trajectories in the backward Monte Carlo approach. Thus, the major criteria for a desirable solution technique, as summarized in the introduction, are met, except for the computational efficiency. The computational inefficiency, however, is found not to be an inherent limitation of the general approach, but rather it is due to a poor initial approximation. Thus in [*Kuo et al.*, 1995], in the case of a plane-parallel atmosphere, the radiance obtained by employing a low order expansion of the spherical harmonics solution has been used as an initial guess for the iterative approach. It has been shown that using such an initial guess much fewer iterations compared to the SOS method are required to achieve convergence. The basic idea of this method is to simplify the integral operator $\mathrm{L_a}$ which characterizes the local properties of the medium. In the case of a spherical atmosphere, a better initial approximation can be achieved retaining the local integral operator $\mathrm{L_a}$ and simplifying instead the integral operator $\mathrm{L_s^{sp}}$, which characterizes the global behavior of light in the atmosphere. Since simplifying the differential operator as given by equations (3.69) and (3.70) does not simplify the integral operator $\mathrm{L_s^{sp}}$, the one-dimensional plane-parallel differential operator $\mathrm{L_s^{pp}}$ is used in the CDIPI radiative transfer model instead of $\mathrm{L_s^{sp}}$ to obtain an initial estimation of the radiation field. This means, the first guess radiance $I_{dif}^{(0)}(r, \Psi, \Phi, \Theta, \varphi)$ has to satisfy the following equation:

$$I_{dif}^{(0)}(r, \Psi, \Phi, \Theta, \varphi) = \mathfrak{I}(r, \Psi, \Phi, \Theta, \varphi) + \mathrm{L_s^{pp}}\, \mathrm{L_a}\, I_{dif}^{(0)}(\tilde{r}, \tilde{\Psi}, \tilde{\Phi}, \hat{\Theta}, \hat{\varphi}) \;, \tag{4.48}$$

where , according to Eq. (3.72), the one-dimensional plane-parallel integral operator $\mathrm{L_s^{pp}}$ is given by

$$\mathrm{L_s^{pp}} = \frac{1}{\cos\Theta} \int_r^{r_b} d\tilde{r}\, \alpha(\tilde{r})\, \exp\left(-\frac{1}{\cos\Theta} \int_r^{\tilde{r}} \alpha(\hat{r})\, d\,\hat{r} \right) \tag{4.49}$$

where r_b refer to the medium boundary and the corresponding differential operator is ,

$$\frac{d}{d\,s} = \cos\Theta\, \frac{\partial}{\partial\, r} \;. \tag{4.50}$$

Using this approach to determine the initial guess, all scattering orders are considered. The dependence of the first guest radiance on the variables r, Ψ, Φ, Θ, and φ can also be accurately taken into account.

Part II

Solar occultation measurements

Chapter 5

Radiative transfer model and retrieval algorithm

5.1 Radiative transfer equation

As discussed in Section 3.1, the direct solar radiation transmitted through the atmosphere is given by Lambert-Beer law, Eq. 3.21. According to Fig 3.2, $\Theta_\mathrm{o} = \pi - \Psi$, and, therefore, $\cos\Theta_\mathrm{o} = -\cos\Psi$, for any point on the instrument line-of-sight. The x-axis of the directional coordinate system is commonly selected to set the azimuth angle of the direct solar beam to zero, i.e. $\varphi_\mathrm{o} = 0$. Thus, the direction $\mathbf{e}_\mathrm{o}$ is defined by the solar zenith angle Ψ and Eq. 3.21 can be rewritten as follows:

$$I_{dir}(r, \Psi, \Phi, \Theta) = F_0\, \delta(\cos\Theta + \cos\Psi, \varphi)\, \mathrm{e}^{-\tau(r,\Psi,\Phi)} \;, \tag{5.1}$$

where τ is the full optical depth along the solar beam given by

$$\tau(r, \Psi, \Phi) = \int_0^{s_\mathrm{o}} \alpha(\tilde{r}(s), \tilde{\Psi}(s), \tilde{\Phi}(s))\, ds \;. \tag{5.2}$$

Here, ds is the differential path-length along the direct solar beam and s_o the full path-length along the beam. The extinction coefficient α is, generally, a function of all three spatial coordinates ($\tilde{r}$, $\tilde{\Psi}$, and $\tilde{\Phi}$). In a spherical atmosphere the spatial coordinates vary along the line-of-sight and, therefore, they are functions of s. The method to calculate $\tilde{r}$, $\tilde{\Psi}$, and $\tilde{\Phi}$ at any point on the line-of-sight from selected initial values r, Ψ, and Φ is discussed in detail in Appendix B. For each point in the atmosphere and each wavelength λ the extinction coefficient can be calculated as follows:

$$\alpha(\tilde{r}, \tilde{\Psi}, \tilde{\Phi}, \lambda) = \sum_{j=1}^{M} \sigma_j(\lambda, T, P)\, N_j(\tilde{r}, \tilde{\Psi}, \tilde{\Phi}) + \alpha_a(\tilde{r}, \tilde{\Psi}, \tilde{\Phi}, \lambda) + \alpha_r(\tilde{r}, \tilde{\Psi}, \tilde{\Phi}, \lambda) \;. \tag{5.3}$$

Here, $\sigma_j(\nu, T, P)$ is the absorption cross section of trace gas j at wavelength λ, temperature T, and pressure P. Generally, the temperature and the pressure depend on the position of

the selected point in the atmosphere, i.e., $T = T(\tilde{r}, \tilde{\Psi}, \tilde{\Phi})$ and $P = P(\tilde{r}, \tilde{\Psi}, \tilde{\Phi})$. $N_j(\tilde{r}, \tilde{\Psi}, \tilde{\Phi})$ is the number density of trace gas j , M is the number of atmospheric trace gases having absorption features at wavelength λ, $\alpha_a(\tilde{r}, \tilde{\Psi}, \tilde{\Phi}, \lambda)$ is the aerosol extinction coefficient, and $\alpha_r(\tilde{r}, \tilde{\Psi}, \tilde{\Phi}, \lambda)$ is the molecular (Rayleigh) scattering coefficient.

The dependence of the intensity of direct solar radiation on global azimuth angle Φ is caused only by the dependence of the extinction coefficient α on this variable. In the case of spherical shell atmosphere, which will be discussed below, the intensity of direct solar radiation is independent of the global azimuth angle.

To interprete measurements performed by satellite or ground-based instruments, only the radiation at the top or the bottom of the atmosphere, respectively, is required. Omitting the dependence on r below means that the quantity refers to the top or the bottom of the atmosphere.

Since the Sun as observed in occultation viewing geometry has a finite geometrical size and the instrument has a finite field of view, the delta-function in Eq. (5.1) has to be replaced by the integration over the instrument field of view, Ω, with the instrument apparatus function, $f(\omega)$. For multispectral instruments the radiation has to be convolved with the instrument slit function, $a(\lambda, \lambda')$, as well. Thus, the radiance, Υ, measured by a satellite or ground-based instrument is a convolution of the direct solar radiation transmitted through the atmosphere with the apparatus function $f(\omega)$, which depends on the field of view of the instrument, and with the slit function $a(\lambda, \lambda')$:

$$\Upsilon(\Psi, \lambda) = \int_{\Omega} \int_{\Delta\lambda} f(w)\, F_0(\lambda')\, a(\lambda, \lambda')\, e^{-\tau(\Psi, \Phi, \omega, \lambda')}\, d\lambda'\, d\omega \; . \tag{5.4}$$

Here, $\Delta\lambda$ is the total width of the instrument slit function. The additional dependence of the optical depth τ on ω depicts that the integration in Eq. (5.2) is performed along different line-of-sights then ω are different. Thus, s is also a function of ω, and, therefore, $\tilde{r}$, $\tilde{\Psi}$ and $\tilde{\Phi}$ are functions of ω as well.

5.2 Absorption cross sections

In the UV-Vis spectral region, where the fine spectral structure of the absorption cross sections of the relevant atmospheric constituents, with exception of H_2O and O_2, is relatively weak, pre-measured moderate resolution absorption cross sections can be used to calculate the extinction coefficient α as given by Eq. (5.3). In order to compute the absorption cross sections of atmospheric trace gases in the near-IR spectral region as well as the absorption cross sections of H_2O and O_2 in the visible spectral region, the so-called "line-by-line" calculations are commonly employed. In this case the formula for absorption cross section at a wavenumber ν is given by

$$\sigma(\nu, P, T) = \sum_i S(\nu_i, T)\, \mathcal{F}(\nu, \nu_i, P, T) \; , \tag{5.5}$$

where $S(\nu_i, T)$ is the spectral line intensity at the temperature T of line i having center wavenumber ν_i and $\mathcal{F}(\nu, \nu_i, P, T)$ is the line shape function. Summation in Eq (5.5) is

performed over all spectral lines whose line shape functions at wavenumber ν are larger than a selected threshold value. According to [*Goody*, 1964], the intensity of the spectral line $S(\nu_i, T)$ at particular temperatures can be calculated using the intensity at a temperature of 296K, S_0, provided by the HITRAN database [*Rothman et al.*, 1998] as follows:

$$S(\nu_i, T) = S_0 \, \frac{n_g(T)}{n_g(T_0)} \, \frac{1 - \exp\left(-\frac{hc\nu_i}{kT}\right)}{1 - \exp\left(-\frac{hc\nu_i}{kT_0}\right)} \, . \tag{5.6}$$

Here, $n_g(T)$ and $n_g(T_0)$ are the populations of the lower energy level at the temperature T and T_0, respectively, h is the Planck constant, c is the light velocity, and k is the Boltzmann constant. The exponential terms in Eq. (5.6) owe their existence to induced emission, see, for example, [*Townes and Schawlow*, 1975], and it is often argued that they may be neglected. The population of an energy level can be found according to the Boltzmann law as follows (only internal energy states are considered):

$$n(T) = \frac{g \, N}{Q^{int}} \, \exp\left(-\frac{hcE}{kT}\right) \, , \tag{5.7}$$

where E and g are level energy and degeneracy, respectively, and Q^{int} is internal partition function (state sum). The partition function characterizes how molecules in thermodynamic equilibrium are distributed among various energy states at particular temperatures. A detailed discussion of the partition functions and methods to calculate them can be found elsewhere, see, for example, [*Fay*, 1965; *Incropera*, 1974]. Generally, the internal molecular partition function is given by

$$Q^{int} = \sum g_n \, \mathrm{e}^{-\frac{E_n}{kT}} \, . \tag{5.8}$$

Here, the sum is calculated over all internal energy states of the molecule, E_n is the total energy in [J] of state n, and g_n is the total statistical weight (degeneracy) of the state. The internal partition function can be approximately considered as the product of component partition functions:

$$Q^{int} = Q^{rot} \, Q^{vib} \, Q^{elec} \, Q^{nuc} \, , \tag{5.9}$$

where Q^{rot}, Q^{vib}, Q^{elec}, and Q^{nuc} are rotational, vibrational, electronic and nuclear partition functions, respectively. The atmospheric species considered in this study are in their ground electronic and nuclear states, thus, the electronic and nuclear partition functions are constant and equal to the electronic and nuclear ground-state degeneracy, respectively, i.e., $Q^{elec} = g_0^{elec}$ and $Q^{nuc} = g_0^{nuc}$.

As discussed by *Gamache et al.* [1990], the product of the vibrational and the rotational partition functions, $Q^{v,r} = Q^{vib} \, Q^{rot}$, as a function of temperature can be approximated by the following polynomial expression:

$$Q^{v,r} = a_0 + a_1 \, T + a_2 \, T^2 + a_3 \, T^3 \, , \tag{5.10}$$

where the coefficients a_0, a_1, a_2, and a_3 are obtained by fitting to the calculated partition functions using a Simplex nonlinear minimization algorithm [*Nelder and Mead*, 1965]. It is

the form of partition functions storage given by Eq. (5.10), which is used in the HITRAN database to simplify the computation of the partition functions.

Thus, combining Eqns. (5.6), (5.7) and (5.9), the following expression for the intensity of the spectral line at the particular temperature T is obtained

$$S(\nu_i, T) = S_0 \frac{Q_0^{v,r}}{Q^{v,r}} \frac{\exp\left(-\frac{hcE_g}{kT}\right)}{\exp\left(-\frac{hcE_g}{kT_0}\right)} \frac{1-\exp\left(-\frac{hc\nu_i}{kT}\right)}{1-\exp\left(-\frac{hc\nu_i}{kT_0}\right)} , \tag{5.11}$$

where E_g is the lower state energy of the transition [cm^{-1}] contained in the HITRAN database. $Q^{v,r}$ and $Q_0^{v,r}$ are the vibrational-rotational partition functions at the temperature T and T_0, respectively.

The shape of spectral lines depends on a dominant broadening mechanism. Spectral lines of atmospheric trace gases are broadened for one of two reasons, either because of the Doppler shifts resulting from molecular thermal motions (Doppler broadening), or because of interactions between pairs of molecules (pressure broadening), see, for example [*Goody*, 1964].

In the troposphere and the lower stratosphere, the pressure broadening of spectral lines dominates and the line shape function is given by Lorentz profile:

$$\mathcal{F}_L(\nu_i, \nu, P, T) = \frac{1}{\pi} \frac{\alpha_L}{(\nu-\nu_i)^2 + \alpha_L^2} . \tag{5.12}$$

Here, α_L is the Lorentz (pressure broadened) line width defined in terms of the half frequency width at the half maximum of the profile. According to [*Goody*, 1964], the expression for Lorentz line width resulting from the kinetic theory is written as follows:

$$\alpha_L = \sum_j n_j \sigma_j^2 \sqrt{\frac{2kT}{\pi}\left(\frac{1}{m} + \frac{1}{m_j}\right)} , \tag{5.13}$$

where n_j is the number density of the jth species of perturber, m_j is its mass, m is the mass of the absorber, and σ_j is the optical collision diameter. If the composition is held constant, all of the n_j are proportional to the total pressure and Eq. (5.13) gives the important result, common to all impact theories, that line width is proportional to the pressure. The temperature variation indicated by Eq. (5.13) depends upon the details of the collision, and is uncertain, but this is rarely a crucial factor in thermal calculations.

Thus, as discussed in [*Rothman et al.*, 1998], the pressure broadened line width at the temperature T and pressure P can be calculated from the Lorentz line width at $T_0 = 296$K and $P_0 = 1$ bar, $\alpha_L(T_0, P_0)$, contained in the HITRAN database as follows:

$$\alpha_L(T, P) = \alpha_L(T_0, P_0) \frac{P}{P_0} \left(\frac{T_0}{T}\right)^{\beta} , \tag{5.14}$$

where β is the temperature dependence coefficient provided by the HITRAN database as well.

As discussed, for example, in [*Breene*, 1961; *Sobel'man*, 1972], due to collision effects the spectral lines are not only broadened but also shifted. The pressure shift of the peak of a spectral line is proportional to the number density of perturber molecules and, therefore, to the total pressure. Using the air-broadened pressure shift at $T_0 = 296$K and $P_0 = 1$ atm, δ^*, from the HITRAN database, a shifted transition frequency ν_i^* can be calculated as follows:

$$\nu_i^* = \nu_i + \delta^* \frac{P}{P_0} \tag{5.15}$$

In upper stratosphere and the mesosphere, where the influence of collision effects is relatively weak, Doppler broadening is dominant, i.e., the width of the spectral lines is determined by the Doppler shifts origined from random molecular motions. The probability that there is a relative velocity u between absorber and observer is, from Maxwell's law,

$$p(u) = \sqrt{\frac{m}{2\pi kT}}\ \exp\left(-\frac{mu^2}{2kT}\right)\ , \tag{5.16}$$

where m is the mass of absorber molecule. If $u/c \ll 1$, the Doppler shift is given by

$$\nu - \nu_i = \frac{\nu_i u}{c}\ . \tag{5.17}$$

Averaging over the Maxwell distribution, the following expression for the Doppler line shape is obtained:

$$\mathcal{F}_{D}(\nu_i, \nu, T) = \frac{1}{\alpha_{D}\sqrt{\pi}}\ \exp\left\{-\left(\frac{\nu - \nu_i}{\alpha_{D}}\right)^2\right\}\ , \tag{5.18}$$

where

$$\alpha_{D} = \frac{\nu_i}{c}\sqrt{\frac{2kT}{m}} \tag{5.19}$$

is the Doppler line width defined in terms of the half frequency width to e^{-1} of the maximum of the profile, rather than 2^{-1} as for the Lorentz profile. The Doppler width does not depend upon the pressure and, thus, at low enough pressures, it always exceeds the Lorentz width.

In the middle atmosphere, both broadening mechanisms have to be taken into account. Assuming the collisional and Doppler broadening to be completely independent, as treated in [*Goody*, 1964; *Sobel'man*, 1972], the collision broadened line shape should be shifted by the Doppler shift Eq. (5.17) and averaged over the Maxwell distribution given by Eq. (5.16). If this procedure is applied to the Lorentz profile, as given by Eq. (5.12), taking into account the pressure shift, Eq. (5.15), the Voigt line shape function is obtained which is commonly used in radiative transfer models in order to approximate the shape of absorption lines in the atmosphere:

$$\mathcal{F}_{v}(\nu_i, \nu, P, T) = \int_{-\infty}^{\infty} \frac{a_{L}}{\pi}\sqrt{\frac{m}{2\pi kT}}\ \frac{1}{\left(\nu - \nu_i^* - \frac{u\nu_i}{c}\right)^2 + a_{L}^2}\ \exp\left(-\frac{mu^2}{2kT}\right)\ du\ . \tag{5.20}$$

The Voigt profile is extensively tabulated in terms of the parameter $d = 2\,a_{L}/a_{D}$ and fast numerical algorithms are available for its computation [*Hui et al.*, 1978; *Humlicek*, 1982].

5.3 Rayleigh scattering

The generally used form of the Rayleigh scattering coefficient per particle (Rayleigh scattering cross section), ε, is that of Cabannes [*Chandrasekhar*, 1960]:

$$\varepsilon(\lambda) = \frac{8\,\pi^3\,(n_s^2-1)^2}{3\,\lambda^4\,N_s^2}\,F_K\ , \tag{5.21}$$

where n_s is the refractive index of standard air[1] which depends on the wavelength and N_s is the Loschmidt's number. The King correction factor [*King*, 1923], F_K, may be expressed as follows:

$$F_K = \frac{6+3\,\rho}{6-7\rho}\ , \tag{5.22}$$

where ρ is the depolarization factor of standard air. Although, according to [*Bates*, 1984], the King correction factor is weakly dependent on wavelength, a wavelength independent King correction value is commonly used for the Rayleigh cross section calculations, see, for example, [*Penndorf*, 1957; *Young*, 1980; *Hoyt*, 1977; *Fröhlich and Shaw*, 1980]. If the refractive index n_s is close to unity, as for a gas, the following expression for the the Rayleigh scattering cross section can be obtained from Eq. (5.21):

$$\varepsilon(\lambda) = \frac{32\,\pi^3\,(n_s-1)^2}{3\,\lambda^4\,N_s^2}\,F_K\ . \tag{5.23}$$

The refractive index is usually calculated using an approximative four- or five-parameter formula. One of the commonly used formulas is that from [*Edlén*, 1966]:

$$(n_s-1)\cdot 10^8 = 8342.13 + \frac{2406030}{130-\lambda^{-2}} + \frac{15997}{38.9-\lambda^{-2}}\ , \tag{5.24}$$

where λ is given in micrometers. The Rayleigh scattering cross section may also be calculated using another formulas, as in [*Edlén*, 1957; *Peck and Reeder*, 1972; *Chance and Spurr*, 1997], or tabulated as a function of wavelength [*Bates*, 1984]. The differences between the Rayleigh cross sections calculated using different formulas are found to be less than 0.5% [*Chance and Spurr*, 1997; *Bucholtz*, 1995].

In order to calculate the Rayleigh scattering coefficient, $\alpha_r(\tilde{r},\tilde{\Psi},\tilde{\Phi},\lambda)$ in Eq. (5.2), the Rayleigh scattering cross section $\varepsilon(\lambda)$ given by Eq. (5.21) has to be multiplied by the molecular number density of air, $N(\tilde{r},\tilde{\Psi},\tilde{\Phi})$, which is a function of pressure and temperature and, therefore, depends on the position of the selected point in the atmosphere. Thus, the following equation for the Rayleigh scattering coefficient is appropriate:

$$\alpha_r(\tilde{r},\tilde{\Psi},\tilde{\Phi},\lambda) = N(\tilde{r},\tilde{\Psi},\tilde{\Phi})\,\varepsilon(\lambda)\ . \tag{5.25}$$

[1] Pressure 1013.25 mb, temperature 15°C

5.4 Aerosol extinction

The extinction cross section, k_{ext}, is one of the major quantities characterizing the scattering of electromagnetic waves by a particle. For the light scattering by small spherical particles, the extinction cross section can be analytically calculated using the Mie theory developed in [*Mie*, 1908] and discussed also in [*Stratton*, 1941; *van de Hulst*, 1957]. The extinction cross section depends on the particle radius, r, on the relative refractive index, n, and on the wavelength, λ. The relative refractive index is given by the ratio of the refraction index of the particle to that of the medium and may be complex. A more convenient parameter, which is commonly used instead of k_{ext}, is the extinction efficiency factor, Q_{ext}, obtained by the division of the extinction cross section by the geometric cross section of the particle, i.e,

$$Q_{ext} = \frac{k_{ext}}{\pi r^2} \; . \tag{5.26}$$

The probability that the particle has a radius r within the range r to $r+dr$ is defined by the aerosol particle size distribution function, $f_a(r)$. Examples of commonly used particle size distribution functions can be found elsewhere, for example, in [*Deirmendjian*, 1969; *Kerker*, 1969; *d'Almeida at al.*, 1991]. In order to obtain the expression for the aerosol extinction coefficient, the extinction cross section has to be multiplied by the aerosol particle number density, N_a, and integrated over all possible particle sizes with the particle size distribution function. According to [*Deirmendjian*, 1969], the expression for the aerosol extinction coefficient can be written as follows:

$$\alpha_a(\tilde{r}, \tilde{\Psi}, \tilde{\Phi}, \lambda) = N_a(\tilde{r}, \tilde{\Psi}, \tilde{\Phi}) \int_0^\infty \pi \, r^2 \, Q_{ext}(r, n, \lambda) \, f_a(r) \, dr \; . \tag{5.27}$$

The first term in Eq. (5.27), the aerosol particle number density, depends only on the position in the atmosphere. Generally, the aerosol particle size distribution function, f_a, and the extinction efficiency factor, Q_{ext}, may also depend on the position in the atmosphere. Thus, Eq. (5.27) can be rewritten as follows:

$$\alpha_a(\tilde{r}, \tilde{\Psi}, \tilde{\Phi}, \lambda) = \tilde{\alpha}_a(\tilde{r}, \tilde{\Psi}, \tilde{\Phi}, \lambda) \, N_a(\tilde{r}, \tilde{\Psi}, \tilde{\Phi}) \; , \tag{5.28}$$

where

$$\tilde{\alpha}_a(\tilde{r}, \tilde{\Psi}, \tilde{\Phi}, \lambda) \equiv \int_0^\infty \pi \, r^2 \, Q_{ext}(r, n(\tilde{r}, \tilde{\Psi}, \tilde{\Phi}, \lambda), \lambda) \, f_a(r, \tilde{r}, \tilde{\Psi}, \tilde{\Phi}, \lambda) \, dr \; . \tag{5.29}$$

In the radiative transfer model under consideration, the first term in Eq. (5.28) is obtained employing the well-known LOWTRAN/MODTRAN aerosol parameterization [*Kneizys et al.*, 1996]. The wavelength dependent term in Eq. (5.28) is usually defined at a relatively rare wavelength grid and is supposed to change linearly with the wavelength between the grid points.

5.5 Weighting functions

5.5.1 Mathematical definition for atmospheric measurements

The interpretation of atmospheric measurements, independent of viewing geometry, comprises commonly the retrieval of the vertical distributions of the atmospheric trace gases as well as eventually aerosol parameters, temperature profile, surface albedo and other atmospheric parameters. Since the radiation field and, therefore, the radiance measured by the instrument, are non-linear functionals of the atmospheric parameters, the so-called non-linear problem has to be solved. Generally, for each wavelength, the intensity of the radiation is a function of five variables, namely, of three spatial variables, $\mathbf{x}^s \equiv \{r, \Psi, \Phi\}$, defining the position in the atmosphere and two directional variables, $\mathbf{x}^d \equiv \{\Theta, \varphi\}$, defining the direction of the radiation.

Forward simulation is performed for a reference or "mean" climatological model of the atmosphere, defined by atmospheric parameters, $\bar{p}_j$ $(j = 1, \ldots, J)$, which are, generally, functions of three spatial variables, i.e., $\bar{p}_j = \bar{p}_j(\mathbf{x}^s)$. The expansion of the radiation field in a functional Taylor series around these mean values of the atmospheric parameters yields a linear relationship between the intensity of the radiation and the variation of atmospheric parameters at each wavelength:

$$I(\mathbf{x}^s, \mathbf{x}^d, \mathbf{p}(\mathbf{x}^s)) = I(\mathbf{x}^s, \mathbf{x}^d, \bar{\mathbf{p}}(\mathbf{x}^s)) + \sum_{j=1}^{J} \int \left. \frac{\delta I(\hat{\mathbf{x}}^s, \mathbf{x}^d, \mathbf{p}(\hat{\mathbf{x}}^s))}{\delta p_j(\hat{\mathbf{x}}^s)} \right|_{\bar{\mathbf{p}}(\hat{\mathbf{x}}^s)} \delta p_j(\hat{\mathbf{x}}^s)\, d\hat{\mathbf{x}}^s \ , \quad (5.30)$$

where $\mathbf{p}(\hat{\mathbf{x}}^s) = \{p_1(\hat{\mathbf{x}}^s), ..., p_J(\hat{\mathbf{x}}^s)\}$ is a vector containing J atmospheric parameters which influence the radiation field. The integration in Eq. (5.30) has to be performed over entire argument space of $p_j(\hat{\mathbf{x}}^s)$, i.e., over all possible values of $\hat{\mathbf{x}}^s$.

Thus, as follows from Eq. (5.30), for a linear problem, the variation of the radiation field due to the variation of the atmospheric parameter $p_j(\mathbf{x}^s)$, defined by

$$\delta I(\mathbf{x}^s, \mathbf{x}^d, \bar{p}_1(\mathbf{x}^s), ..., p_j(\mathbf{x}^s), ..., \bar{p}_J(\mathbf{x}^s)) = I(\mathbf{x}^s, \mathbf{x}^d, \bar{p}_1(\mathbf{x}^s), ..., p_j(\mathbf{x}^s), ..., \bar{p}_J(\mathbf{x}^s)) - I(\mathbf{x}^s, \mathbf{x}^d, \bar{\mathbf{p}}(\mathbf{x}^s)) \ , \quad (5.31)$$

is proportional to the variation of this parameter, $\delta p_j(\hat{\mathbf{x}}^s)$ given by

$$\delta p_j(\mathbf{x}^s) = p_j(\mathbf{x}^s) - \bar{p}_j(\mathbf{x}^s) \ , \quad (5.32)$$

with the coefficient of proportionality called weighting function. Therefore, according to Eq. (5.30), the weighting function of an atmospheric parameter is defined as a variational derivative of the intensity of radiation with respect to this parameter calculated at the mean value of the parameter assuming that other parameters remain unchanged:

$$W_j(\mathbf{x}^s, \mathbf{x}^d, \bar{\mathbf{p}}(\mathbf{x}^s)) \equiv \left. \frac{\delta I(\mathbf{x}^s, \mathbf{x}^d, \mathbf{p}(\mathbf{x}^s))}{\delta p_j(\mathbf{x}^s)} \right|_{\bar{\mathbf{p}}(\mathbf{x}^s)} \quad (5.33)$$

Thus, for the variation of the radiation field due to the variation of atmospheric parameters, Eq. (5.30) can be rewritten as follows:

$$\delta I(\mathbf{x}^s, \mathbf{x}^d, \mathbf{p}(\mathbf{x}^s)) = \sum_{j=1}^{J} \int W_j(\hat{\mathbf{x}}^s, \mathbf{x}^d, \bar{\mathbf{p}}(\mathbf{x}^s))\, \delta p_j(\hat{\mathbf{x}}^s)\, d\hat{\mathbf{x}}^s \,. \tag{5.34}$$

5.5.2 Weighting functions for occultation measurements

For occultation measurements, the atmospheric parameters of interest are the trace gas number densities, N_j, which, generally, depend on r, Ψ and Φ. Therefore, the vector of parameters, $\mathbf{p}(\hat{\mathbf{x}}^s)$, is given by $\{N_1(r, \Psi, \Phi), ..., N_J(r, \Psi, \Phi)\}$. For a spherical shell atmosphere, the dependence on the global azimuth angle, Φ, disappears. Furthermore, for most applications, the atmospheric trace gas number densities are assumed to be independent on the local solar zenith angle, Ψ, i.e., $N_j = N_j(r)$. Thus, commonly, only vertical distributions of the atmospheric trace gas number density are of interest. Since the radiance measured by the instrument, Υ, as given by Eq. (5.4) rather than the radiation field, as discussed in Section 5.5.1, is known, Eq. (5.34) is rewritten with respect to the measured radiance as follows:

$$\delta\Upsilon(\Psi, \lambda, \mathbf{p}(r)) = \sum_{j=1}^{J} \int_{r_b}^{r_t} W_j(\Psi, \lambda, \bar{\mathbf{p}}(\hat{r}))\, \delta p_j(\hat{r})\, d\hat{r} \,. \tag{5.35}$$

Here, r_t and r_b denote the top and the bottom of the atmosphere, respectively, and W_j are the weighting functions for the measured radiance rather then for the intensity, i.e., analogous to Eq. (5.33):

$$W_j(\mathbf{x}^s, \mathbf{x}^d, \bar{\mathbf{p}}(\mathbf{x}^s)) \equiv \left. \frac{\delta\Upsilon(\mathbf{x}^s, \mathbf{x}^d, \mathbf{p}(\mathbf{x}^s))}{\delta p_j(\mathbf{x}^s)} \right|_{\bar{\mathbf{p}}(\mathbf{x}^s)} \tag{5.36}$$

For occultation measurements, the weighting functions of the atmospheric trace gases, as defined by Eq. (5.36), may be derived analytically as discussed below. The variation of the measured radiance due to variation of the concentration of trace gas j is given by

$$\begin{aligned} \delta\Upsilon(\Psi, \lambda, N_1(r), ..., N_j(r), ..., N_J(r)) = \\ \Upsilon(\Psi, \lambda, N_1(r), ..., N_j(r) + \delta N_j(r), ..., N_J(r)) \\ - \Upsilon(\Psi, \lambda, N_1(r), ..., N_j(r), ..., N_J(r)) \,. \end{aligned} \tag{5.37}$$

Substituting the measured radiance as given by Eq. (5.4) in Eq. (5.37), the following expression for the variation of the measured radiance due to variation of the concentration of trace gas j is obtained:

$$\delta\Upsilon(\Psi, \lambda) = \int_{\Omega} \int_{\Delta\lambda} f(w)\, F_0(\lambda')\, a(\lambda, \lambda') \left[-e^{-\tau_j(\Psi, \omega, \lambda')}\, \delta\tau(\Psi, \omega, \lambda') \right] d\lambda'\, d\omega \,. \tag{5.38}$$

Using Eq. (5.2) to calculate the variation of the optical depth due to variation of the concentration of trace gas j, $\delta\tau_j(\Psi,\omega,\lambda')$, and changing the order of integration, the following equation is obtained:

$$\delta\Upsilon(\Psi,\lambda) = -\int_\Omega d\omega\, f(w) \int_0^{s_o} ds\, \delta N_j(\tilde{r}) \int_{\Delta\lambda} a(\lambda,\lambda')\, F_0(\lambda')\, e^{-\tau_j(\Psi,\omega,\lambda')}\, \sigma_j(\lambda',\tilde{r})\, d\lambda' \,, \quad (5.39)$$

Here, as discussed in Section 5.1, $\tilde{r}$ is a function of s, whereas s and s_o are functions of ω. The atmospheric trace gas cross sections are assumed to be independent on the local solar zenith angle, $\tilde{\Psi}$, i.e., $\sigma_j = \sigma_j(\lambda',\tilde{r})$. Using an appropriate Jacobian, the integration along the direct solar beam in Eq. (5.39) can be replaced by the integration along the vertical as follows:

$$ds(\omega) = \frac{d\tilde{r}}{\cos\tilde{\Psi}(\tilde{r},\omega)} \,. \quad (5.40)$$

Thus, introducing a new function, $\chi(\Psi,\tilde{r},\omega)$, Eq. (5.39) can be rewritten as follows:

$$\delta\Upsilon(\Psi,\lambda) = -\int_\Omega d\omega\, f(w) \int_{r_b}^{r_t} d\tilde{r}\, \frac{\delta N_j(\tilde{r})}{\cos\tilde{\Psi}(\tilde{r},\omega)}\, \chi(\Psi,\tilde{r},\omega) \int_{\Delta\lambda} a(\lambda,\lambda')\, F_0(\lambda')\, e^{-\tau_j(\Psi,\omega,\lambda')}\, \sigma_j(\lambda',\tilde{r})\, d\lambda' \,, \quad (5.41)$$

Here, the function $\chi(\Psi,\tilde{r},\omega)$ is defined as follows. For ground-based measurements, $\chi(\Psi,\tilde{r},\omega) = 1$ is appropriate. For measurements performed by means of satellite-based instruments, the following function is appropriate:

$$\begin{cases} \chi(\Psi,\tilde{r},\omega) = 2, r > R+h \\ \chi(\Psi,\tilde{r},\omega) = 0, r \le R+h \end{cases} \,, \quad (5.42)$$

which is similar to the Heaviside function. Here, R is the Earth's radius and h is the tangent height of the instrument line-of-sight. The geometrical tangent height, i.e., the tangent height neglecting refraction effects, h_g, can be calculated as follows:

$$h_g = (R+H)\sin\Psi - R \,, \quad (5.43)$$

where H in Eq. (5.43) denote the total height of the atmosphere. The tangent height is commonly used instead of the solar zenith angle to determine the line-of-sight direction of satellite-based instruments.

Changing the order of the integration in Eq. (5.39) leads to the following expression for the variation of the measured radiance:

$$\delta\Upsilon(\Psi,\lambda) = -\int_{r_b}^{r_t} d\tilde{r}\, \delta N_j(\tilde{r}) \int_\Omega d\omega\, \frac{f(w)}{\cos\tilde{\Psi}(\tilde{r},\omega)}\, \chi(\Psi,\tilde{r},\omega) \int_{\Delta\lambda} a(\lambda,\lambda')\, F_0(\lambda')\, e^{-\tau_j(\Psi,\omega,\lambda')}\, \sigma_j(\lambda',\tilde{r})\, d\lambda' \,, \quad (5.44)$$

Comparing Eqns. (5.35) and (5.44), the following expression for the weighting function of atmospheric trace gas j is obtained:

$$W_j(\Psi, \lambda, \mathbf{p}(\tilde{r})) = -\int_{\Omega} d\omega \, \frac{\hat{\chi}(\Psi, \tilde{r}, \omega)}{\cos\tilde{\Psi}(\tilde{r}, \omega)} \int_{\Delta\lambda} a(\lambda, \lambda') \, F_0(\lambda') \, e^{-\tau_j(\Psi, \omega, \lambda')} \, \sigma_j(\lambda', \tilde{r}) \, d\lambda' \, , \quad (5.45)$$

where

$$\hat{\chi}(\Psi, \tilde{r}, \omega) \equiv f(\omega) \, \chi(\Psi, \tilde{r}, \omega) \, . \quad (5.46)$$

One of the commonly used approximations for the instrument apparatus function, $f(\omega)$, is given by

$$\begin{cases} f(\omega) = 1, & \omega \in \Omega \\ f(\omega) = 0, & \omega \notin \Omega \end{cases} \quad (5.47)$$

5.6 Retrieval algorithm

5.6.1 Optimal estimation method

One of the commonly used methods of retrieving atmospheric parameters from the measurements of the atmospheric radiation using *a priori* information is the optimal estimation method. The method is discussed in detail in [*Rodgers*, 1976, 1990] and will be briefly described below.

The parameters to be retrieved from the measurements are represented by a model state vector $\mathbf{x}$ with M elements. Usually, the model state vector contains vertical profiles of atmospheric constituents defined at a finite number of layers, n. In this case, $M = n \times J$, where J is the number of the atmospheric constituents whose vertical profiles are to be retrieved. For each model state vector there is a corresponding measurement vector $\mathbf{y}$, which contains L measurements of atmospheric radiation at various spectral points and at various solar zenith angles (tangent heights). Measurements are made to a finite accuracy, with measurement error ε assumed to be normally distributed with mean zero and known error covariance $\mathbf{S}_y$.

The relationship between the model state vector and the measurement vector can be written formally as:

$$\mathbf{y} = \mathbf{A}\mathbf{x} + \varepsilon \, , \quad (5.48)$$

where $\mathbf{A}$ is a non-linear forward model operator. For a linearized forward model the following equation is appropriate instead of Eq. (5.48):

$$\mathbf{y} = \mathbf{y}_0 + \mathbf{K_0}(\mathbf{x} - \mathbf{x}_0) + \varepsilon \, . \quad (5.49)$$

Here, $\mathbf{x}_0$ is an *a priori* state vector, $\mathbf{K}_0$ is a linear forward model operator, and $\mathbf{y}_0$ is a measurement vector corresponding to the *a priori* state vector $\mathbf{x}_0$, i.e., $\mathbf{y}_0$ is calculated using the forward model as follows:

$$\mathbf{y}_0 = \mathbf{A}\mathbf{x}_0 \, . \quad (5.50)$$

The linear forward model operator $\mathbf{K}_0$ is commonly defined by the Taylor series expansion of the forward model operator $\mathbf{A}$ as follows:

$$\mathbf{A}\mathbf{x} \approx \mathbf{A}\mathbf{x}_0 + \left.\frac{\delta \mathbf{A}}{\delta \mathbf{x}}\right|_{\mathbf{x}_0} (\mathbf{x} - \mathbf{x}_0) = \mathbf{y}_0 + \mathbf{K}_0(\mathbf{x} - \mathbf{x}_0) \; . \tag{5.51}$$

Thus, in order to solve the linear inverse problem, the following quadratic form has to be minimized:

$$\| \; (\mathbf{y} - \mathbf{y}_0) - \mathbf{K}_0(\mathbf{x} - \mathbf{x}_0) \; \|^2_{\mathbf{S}_y^{-1}} + \| \; \mathbf{x} - \mathbf{x}_0 \; \|^2_{\mathbf{S}_a^{-1}} \; , \tag{5.52}$$

where $\mathbf{S}_a$ is an *a priori* covariance matrix. The measurement error covariance matrix $\mathbf{S}_y$ is usually assumed to be diagonal, i.e. no correlation between measurement errors at different wavelengths or different tangent heights is considered. Minimizing the quadratic form given by Eq. (5.52) the optimal estimation solution can be obtained:

$$\mathbf{x} = \mathbf{x}_0 + \left(\mathbf{K}_0^T \, \mathbf{S}_y^{-1} \, \mathbf{K}_0 + \mathbf{S}_a^{-1}\right)^{-1} \mathbf{K}_0^T \, \mathbf{S}_y^{-1} \, (\mathbf{y} - \mathbf{y}_0) \; , \tag{5.53}$$

The superscripts T and -1 designate the matrix transpose and inverse, respectively. If the approximation given by Eq. (5.51) is not accurate enough, the solution has to be estimated iteratively. Thus, according to Eq. (5.53), the optimal estimation solution in the iteration step $i+1$ can be written as

$$\mathbf{x}_{i+1} = \mathbf{x}_0 + \left(\mathbf{K}_i^T \, \mathbf{S}_y^{-1} \, \mathbf{K}_i + \mathbf{S}_a^{-1}\right)^{-1} \mathbf{K}_i^T \, \mathbf{S}_y^{-1} \, \left[\mathbf{y} - \mathbf{y}_i + \mathbf{K}_i(\mathbf{x}_i - \mathbf{x}_0)\right] \; , \tag{5.54}$$

After convergence has occurred, the result of the last iteration is identified with retrieval solution $\hat{\mathbf{x}}$. The corresponding solution covariance matrix is given by

$$\hat{\mathbf{S}} = \left(\hat{\mathbf{K}}^T \, \mathbf{S}_y^{-1} \, \hat{\mathbf{K}} + \mathbf{S}_a^{-1}\right)^{-1} \; . \tag{5.55}$$

The theoretical precision of the retrieval of the j-th parameter is defined in terms of elements of matrix $\hat{\mathbf{S}}$ as follows:

$$s_j = \frac{\sigma_j}{x_0^j} \; , \tag{5.56}$$

where σ_j is a square root of the i-th diagonal element of matrix $\hat{\mathbf{S}}$ and x_0^j is the *a priori* value of the j-th parameter to be estimated.

A quantity frequently used to characterize the impact of the true state $\mathbf{x}_t$ on the retrieved state $\hat{\mathbf{x}}$ is the averaging kernels matrix $\hat{\mathbf{A}}_k$, which is defined as

$$\hat{\mathbf{A}}_k = \frac{\partial \hat{\mathbf{x}}}{\partial \mathbf{x}_t} \; . \tag{5.57}$$

In the optimal estimation method the averaging kernels matrix has the following algebraic form:

$$\hat{\mathbf{A}}_k = \left(\hat{\mathbf{K}}^T \, \mathbf{S}_y^{-1} \, \hat{\mathbf{K}} + \mathbf{S}_a^{-1}\right)^{-1} \hat{\mathbf{K}}^T \, \mathbf{S}_y^{-1} \, \hat{\mathbf{K}} \; . \tag{5.58}$$

Using this expression and taking into account Eq. (5.54), the retrieval solution, $\hat{\mathbf{x}}$, can be approximated by

$$\hat{\mathbf{x}} = \mathbf{x}_0 + \hat{\mathbf{A}}_k(\mathbf{x}_t - \mathbf{x}_0) \ , \tag{5.59}$$

that is, if the model state vector is a vertical profile, the retrieved values at each altitude can be expressed as the sum of the *a priori* value at this altitude and of the deviation of the true profile from the *a priori* profile smoothed with the associated row of the averaging kernel matrix.

For an ideal observing system, $\hat{\mathbf{A}}_k$ is a unit matrix. In reality, the rows of the averaging kernel matrix are peaked with a finite width, which can be regarded as a measure of the vertical resolution of the retrieved profile. Some examples of the averaging kernels for solar occultation measurements at various wavelengths can be found in Chapter 6.

5.6.2 Information operator approach

For the atmospheric measurements, the number of parameters to be retrieved is often larger then the rank of the linear forward model operator, $\hat{\mathbf{K}}$, formally defining the maximum number of independent parameters that can be retrieved from the measurement. In the presence of measurement noise the number of parameters retrieved to useful accuracy can be even smaller. It can be estimated by analyzing the information content of the measurement as introduced in [*Shannon and Weaver*, 1949]. According to [*Yaglom and Yaglom*, 1983], under the assumption that both the *a priori* state vector, $\mathbf{x}_0$, and measurement vector, $\mathbf{y}$, can be described by a Gaussian probability density function, the information content, H, of a measurement is given by

$$H = \frac{1}{2} \ln \Big[\det(\mathbf{S}_a)\Big] + \frac{1}{2} \ln \Big[\det(\hat{\mathbf{S}})\Big] \ . \tag{5.60}$$

An elegant way to adapt the number of fit parameters to the information content of the measurement was proposed by *Kozlov* [1983]. A new operator, $\mathbf{P}$, called "information operator" was introduced as

$$\mathbf{P} = \mathbf{S}_a\mathbf{G} \ , \tag{5.61}$$

where

$$\mathbf{G} = \hat{\mathbf{K}}^T\mathbf{S}_y^{-1}\hat{\mathbf{K}} \ , \tag{5.62}$$

and its eigenvalue problem was considered:

$$\mathbf{P}\,\psi_k = \lambda_k\,\psi_k \ . \tag{5.63}$$

The eigenvectors of the information operator, ψ_k, form a basis of the state space. Combining Eqns. (5.60), (5.61), and (5.62), the following equation for the information content of a measurement in terms of eigenvalues of the information operator can be obtained:

$$H = \frac{1}{2} \ln \Big[\det(\mathbf{P} + \mathbf{I})\Big] = \frac{1}{2} \sum_k \ln(\lambda_k + 1) \ . \tag{5.64}$$

Here, $\mathbf{I}$ denotes a unity operator. The operator $\mathbf{P}$ is positive definite and its eigenvalues, thus, are all positive. Commonly, only eigenvalues $\lambda_k > 1$ are considered to make a relevant contribution to the information content. Thus, the state space spanned by the eigenvectors associated with the relevant eigenvalues corresponds to the effective state space accessible with the measurement. Therefore, the number of fit parameters can be easily adapted to the measurement information content expanding the model state vector into a series of eigenvectors of the information operator:

$$\mathbf{x}_{i+1} - \mathbf{x}_0 = \sum_{k=1}^{N_i} \beta_{i,k} \psi_{i,k} \ . \tag{5.65}$$

Here, analogously to Eq. (5.54), $i+1$ denotes the iteration step number and N_i is the number of eigenvalues which are larger than the unity. Now, instead of the state vector $\mathbf{x}_{i+1}$ itself, the expansion coefficients $\beta_{i,k}$ have to be determined. Substituting Eq. (5.65) into Eq. (5.54) leads to

$$\sum_{k=1}^{N_i} \mathbf{G} \beta_{i,k} \psi_{i,k} + \sum_{k=1}^{N_i} \mathbf{S}_a^{-1} \beta_{i,k} \psi_{i,k} = \mathbf{K}_i^T \, \mathbf{S}_y^{-1} \, \Big[\mathbf{y} - \mathbf{y}_i + \mathbf{K}_i (\mathbf{x}_i - \mathbf{x}_0) \Big] \ . \tag{5.66}$$

Introducing a new basis in the state space as

$$\phi_k \equiv \mathbf{G} \, \psi_k \ , \tag{5.67}$$

another feature of the information operator can be employed, namely, the biorthogonality of the basis sets ψ_k and ϕ_k, i.e., for the scalar product of eigenvectors, $\langle \phi_k, \psi_l \rangle$, the following equation is appropriate:

$$\langle \phi_k, \psi_l \rangle = \delta_{kl} \, n_k \ , \tag{5.68}$$

where

$$n_k = \langle \phi_k, \psi_k \rangle \tag{5.69}$$

and δ_{kl} is the Kronecker delta. Combining Eqns. (5.61)–(5.63) and Eq. (5.67) leads to

$$\mathbf{S}_a^{-1} \psi_k = \frac{1}{\lambda_k} \phi_k \ . \tag{5.70}$$

Substituting Eqns. (5.67) and (5.70), Eq. (5.66) can be rewritten as follows:

$$\sum_{k=1}^{N_i} \beta_{i,k} \phi_{i,k} + \sum_{k=1}^{N_i} \frac{1}{\lambda_{i,k}} \beta_{i,k} \phi_{i,k} = \mathbf{K}_i^T \, \mathbf{S}_y^{-1} \, \Big[\mathbf{y} - \mathbf{y}_i + \mathbf{K}_i (\mathbf{x}_i - \mathbf{x}_0) \Big] \ . \tag{5.71}$$

Multiplying both sides of Eq. (5.71) with ψ_k and taking into account the biorthogonality of the basis sets ψ_k and ϕ_k, as given by Eq. (5.68), the following expression for the expansion coefficients $\beta_{i,k}$ is obtained:

$$\beta_{i,k} = \frac{\lambda_{i,k}}{n_{i,k} \, (1 + \lambda_{i,k})} \, \psi_{i,k}^T \, \mathbf{K}_i^T \, \mathbf{S}_y^{-1} \, \Big[\mathbf{y} - \mathbf{y}_i + \mathbf{K}_i (\mathbf{x}_i - \mathbf{x}_0) \Big] \tag{5.72}$$

Thus, the information operator approach uses *a priori* information in the same statistical sense as the optimal estimation method. However, in the fit process, only those parameters are considered about which there is information actually contained in the measurement.

5.6.3 Numerical aspects

As discussed in Section 5.5.2, for solar occultation measurements, the vertical distributions of the atmospheric trace gas number density, $N_j(r)$, are the parameters of interest. Each parameter is defined at a finite number of layers, r_l, $l = 1, \ldots, \mathcal{L}$. Thus, state vectors $\mathbf{x}_0$ and $\mathbf{x}$, as introduced in Section 5.6.1, are given by

$$\mathbf{x}_0 = \begin{bmatrix} N_1(r_1) \\ \vdots \\ N_1(r_{\mathcal{L}}) \\ \vdots \\ N_j(r_l) \\ \vdots \\ N_J(r_1) \\ \vdots \\ N_J(r_{\mathcal{L}}) \end{bmatrix} \quad \text{and} \quad \mathbf{x} = \begin{bmatrix} N_1(r_1) + \delta N_1(r_1) \\ \vdots \\ N_1(r_{\mathcal{L}}) + \delta N_1(r_{\mathcal{L}}) \\ \vdots \\ N_j(r_l) + \delta N_j(r_l) \\ \vdots \\ N_J(r_1) + \delta N_1(r_1) \\ \vdots \\ N_J(r_{\mathcal{L}}) + \delta N_J(r_{\mathcal{L}}) \end{bmatrix} , \tag{5.73}$$

respectively. Here, J denotes the total number of atmospheric trace gases whose vertical distributions are retrieved. Each state vector, hence, contains $M = \mathcal{L} \times J$ elements. For numerical reasons, the parameters to be estimated are not the number density vertical distributions in absolute units but rather their relative deviations from the *a priori* (mean) values. Using the notations of Section 5.5, the vector of estimated parameters, $\mathbf{p}$, is given by

$$\mathbf{p} = \begin{bmatrix} \delta N_1(r_1)/N_1(r_1) \\ \vdots \\ \delta N_1(r_{\mathcal{L}})/N_1(r_{\mathcal{L}}) \\ \vdots \\ \delta N_j(r_l)/N_j(r_l) \\ \vdots \\ \delta N_J(r_1)/N_J(r_1) \\ \vdots \\ \delta N_J(r_{\mathcal{L}})/N_J(r_{\mathcal{L}}) \end{bmatrix} . \tag{5.74}$$

Thus, in comparison with Section 5.5, the state vector containing J parameters $N_j(r)$ as functions of continuous argument r has to be replaced by the state vector containing the atmospheric trace gas number densities at discrete altitude levels. Hence, the equation for the variation of the radiance measured by the instrument due to the variation of the atmospheric trace gas number densities, as given by Eq. (5.35), has to be rewritten in the discrete form as well. Thus, for any Ψ and λ the following relation is appropriate:

$$\delta\Upsilon(\Psi, \lambda, \mathbf{x}_0) = \sum_{j=1}^{J} \sum_{l=1}^{\mathcal{L}} W_{jl}(\Psi, \lambda, \mathbf{x}_0)\, \delta N_j(r_l)\, q_l \ , \tag{5.75}$$

where q_l are the quadrature coefficients appropriate to the selected integration rule.

The measurement vector $\mathbf{y}$, as introduced in Section 5.6.1, represents the radiance measured by the instrument at a set of discrete wavelengths λ_i, $i = 1, \ldots, \mathcal{I}$ and solar zenith angles, Ψ_k, $k = 1, \ldots, \mathcal{K}$. Thus, the measurement vector, $\mathbf{y}$, containing $L = \mathcal{I} \times \mathcal{K}$ elements is given by

$$\mathbf{y} = \begin{bmatrix} \Upsilon(\Psi_1, \lambda_1) \\ \vdots \\ \Upsilon(\Psi_1, \lambda_\mathcal{I}) \\ \vdots \\ \Upsilon(\Psi_k, \lambda_i) \\ \vdots \\ \Upsilon(\Psi_\mathcal{K}, \lambda_1) \\ \vdots \\ \Upsilon(\Psi_\mathcal{K}, \lambda_\mathcal{I}) \end{bmatrix} \quad \text{and, thus,} \quad \mathbf{y} - \mathbf{y}_0 = \begin{bmatrix} \delta\Upsilon(\Psi_1, \lambda_1) \\ \vdots \\ \delta\Upsilon(\Psi_1, \lambda_\mathcal{I}) \\ \vdots \\ \delta\Upsilon(\Psi_k, \lambda_i) \\ \vdots \\ \delta\Upsilon(\Psi_\mathcal{K}, \lambda_1) \\ \vdots \\ \delta\Upsilon(\Psi_\mathcal{K}, \lambda_\mathcal{I}) \end{bmatrix} . \tag{5.76}$$

Comparing Eqns. (5.75) and (5.49) and taking into account Eqns. (5.76) and (5.74) leads to the following expression for the linear forward model operator, $\mathbf{K}_0$:

$$\mathbf{K}_0 = \begin{bmatrix} \tilde{W}_{11}(\Psi_1, \lambda_1, \mathbf{x}_0)\, q_1 & \ldots & \tilde{W}_{jl}(\Psi_1, \lambda_1, \mathbf{x}_0)\, q_l & \ldots & \tilde{W}_{J\mathcal{L}}(\Psi_1, \lambda_1, \mathbf{x}_0)\, q_\mathcal{L} \\ \vdots & & \vdots & & \vdots \\ \tilde{W}_{11}(\Psi_1, \lambda_\mathcal{I}, \mathbf{x}_0)\, q_1 & \ldots & \tilde{W}_{jl}(\Psi_1, \lambda_\mathcal{I}, \mathbf{x}_0)\, q_l & \ldots & \tilde{W}_{J\mathcal{L}}(\Psi_1, \lambda_\mathcal{I}, \mathbf{x}_0)\, q_\mathcal{L} \\ \vdots & & \vdots & & \vdots \\ \tilde{W}_{11}(\Psi_k, \lambda_i, \mathbf{x}_0)\, q_1 & \ldots & \tilde{W}_{jl}(\Psi_k, \lambda_i, \mathbf{x}_0)\, q_l & \ldots & \tilde{W}_{J\mathcal{L}}(\Psi_k, \lambda_i, \mathbf{x}_0)\, q_\mathcal{L} \\ \vdots & & \vdots & & \vdots \\ \tilde{W}_{11}(\Psi_\mathcal{K}, \lambda_1, \mathbf{x}_0)\, q_1 & \ldots & \tilde{W}_{jl}(\Psi_\mathcal{K}, \lambda_1, \mathbf{x}_0)\, q_l & \ldots & \tilde{W}_{J\mathcal{L}}(\Psi_\mathcal{K}, \lambda_1, \mathbf{x}_0)\, q_\mathcal{L} \\ \vdots & & \vdots & & \vdots \\ \tilde{W}_{11}(\Psi_\mathcal{K}, \lambda_\mathcal{I}, \mathbf{x}_0)\, q_1 & \ldots & \tilde{W}_{jl}(\Psi_\mathcal{K}, \lambda_\mathcal{I}, \mathbf{x}_0)\, q_l & \ldots & \tilde{W}_{J\mathcal{L}}(\Psi_\mathcal{K}, \lambda_\mathcal{I}, \mathbf{x}_0)\, q_\mathcal{L} \end{bmatrix} , \tag{5.77}$$

where $\tilde{W}_{jl}(\Psi_k, \lambda_i, \mathbf{x}_0)$ are the weighting functions appropriate to the relative variation of the corresponding parameters given by

$$\tilde{W}_{jl}(\Psi_k, \lambda_i, \mathbf{x}_0) \equiv W_{jl}(\Psi_k, \lambda_i, \mathbf{x}_0)\, N_j(r_l) . \tag{5.78}$$

The measurement error covariance matrix, $\mathbf{S}_y$, is commonly a diagonal matrix, i.e., the measurement errors at different wavelengths and solar zenith angles are assumed to be uncorrelated. The diagonal elements of $\mathbf{S}_y$ are the squares of the relative random errors of the measured radiances. The *a priori* covariance matrix, $\mathbf{S}_a$, is a block diagonal matrix, i.e., vertical distributions of different atmospheric trace gases are assumed to be uncorrelated. The diagonal elements of $\mathbf{S}_a$ represent the variances of the vertical distribution of atmospheric trace gases and can be derived from climatology. The off-diagonal elements

within each diagonal block are usually approximated by

$$\mathbf{S}_{a,j}^{l'l''} = \sigma_{j,l'}\,\sigma_{j,l''}\,\exp\left(-\frac{|r_{l'} - r_{l''}|}{r_c}\right)\,, \tag{5.79}$$

where

$$j = 1, \ldots, J\,; \quad k = 1, \ldots, \mathcal{L}\,; \quad \text{and} \quad l = 1, \ldots, \mathcal{L}\,. \tag{5.80}$$

Here, index j denotes the number of diagonal block, $\sigma^2_{j,l'}$ and $\sigma^2_{j,l''}$ are the variances which correspond to altitude levels $r_{l'}$ and $r_{l''}$, respectively, and r_c is the correlation length. The commonly used value for the correlation length is 5 km over the whole atmosphere, see, for example, [*Hoogen et al.*, 1999].

Chapter 6

Results

6.1 Simulated spectra

Typical transmission spectra which are expected to be measured by means of the SCIAMACHY instrument in the solar occultation mode are shown in Figs. 6.1 and 6.2. The simulated radiation discussed below is assumed to be the sun-normalized radiation, i.e., the radiation measured by the detector divided by extraterrestrial solar radiation. The simulations were performed using Eq. (5.4) neglecting the field of view effects. This means that the apparatus function, $f(\omega)$, was assumed to be a delta-function, i.e., using the coordinates introduced in Section 3.3, $f(\omega) = \delta(\Theta + \Psi)\,\delta(\varphi)$. All calculations discussed in this chapter were performed using trace gas vertical profiles from MPI [*Brühl and Crutzen*,

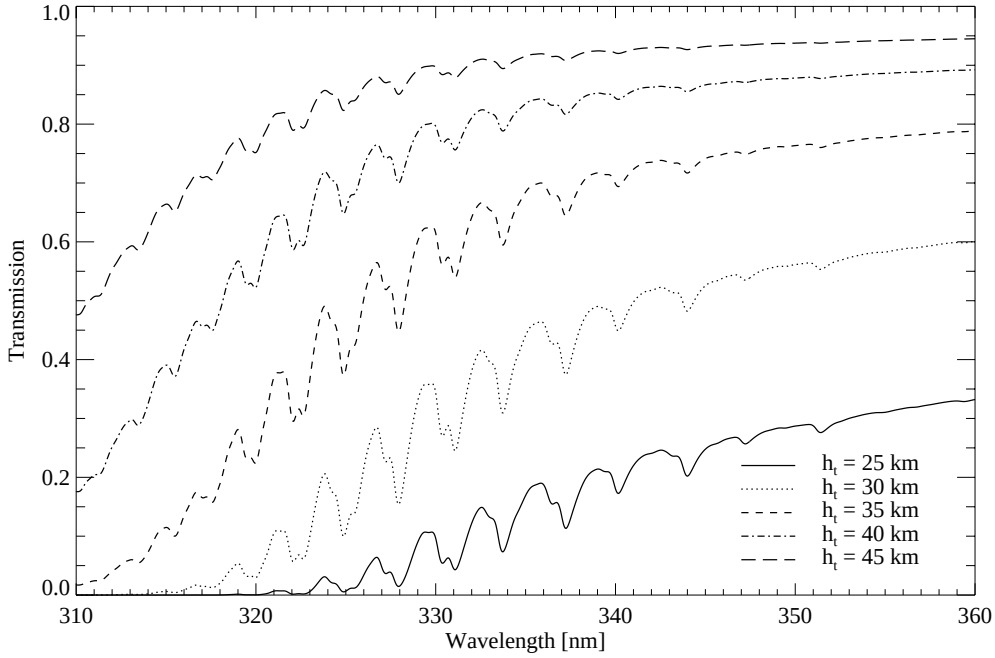

Figure 6.1: Simulated transmission in UV spectral region for different tangent heights.

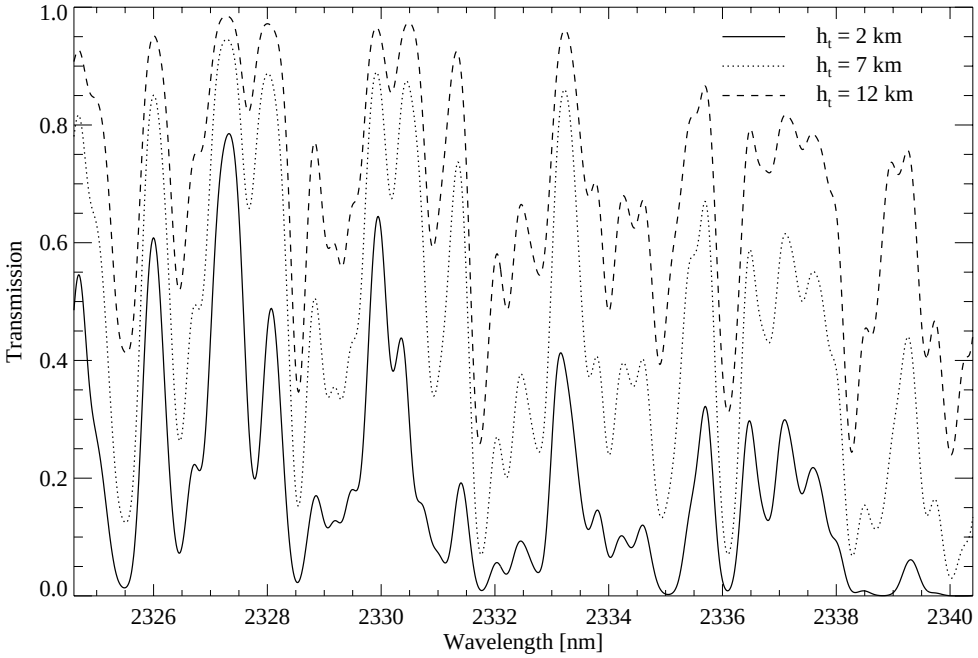

Figure 6.2: Simulated transmission in near IR spectral region for different tangent heights.

1993] (channel 1 to 3 according to Table 2.1) and AGFL-86 [*Anderson*, 1986] (channels 4 to 8 according to Table 2.1) atmospheric models as *a priori* information.

Figure 6.1 shows the simulated radiation in SCIAMACHY channel 2 for five tangent heights, h_t. The attenuation of solar radiation in this spectral region is caused mostly by ozone absorption. Due to strong absorption, there is almost no transmitted radiation for tangent heights below 25 km at wavelengths shorter then 325 nm. Contrastingly, for tangent heights above 45 km, ozone absorption is too weak at wavelengths longer than 330 nm. Thus, in order to obtain information about ozone vertical distribution in both upper and lower stratosphere, multispectral measurements have to be performed. Figure 6.2 shows the simulated radiation in SCIAMACHY channel 8 for three tangent heights. Since main absorbing trace gases in this spectral region are H_2O, CH_4 and CO which are tropospheric components, the strongest absorption features, rapidly decreasing with the tangent height, are observed in the lower troposphere. Thus, maximum sensitivity of the solar occultation measurements in chanel 8 is reached in the lower troposphere.

6.2 Weighting functions

Figures 6.3 and 6.4 show weighting functions of ozone and CO as functions of the altitude at 328 nm and 2333.74 nm, respectively, for different tangent heights. The weighting functions were calculated according to Eqns. (5.78) and (5.45). Similar to the transmission spectra simulations, the field of view effects were neglected. Maximum sensitivity is reached at tangent heights between 30 km and 35 km for ozone and between 5 km and 12 km for

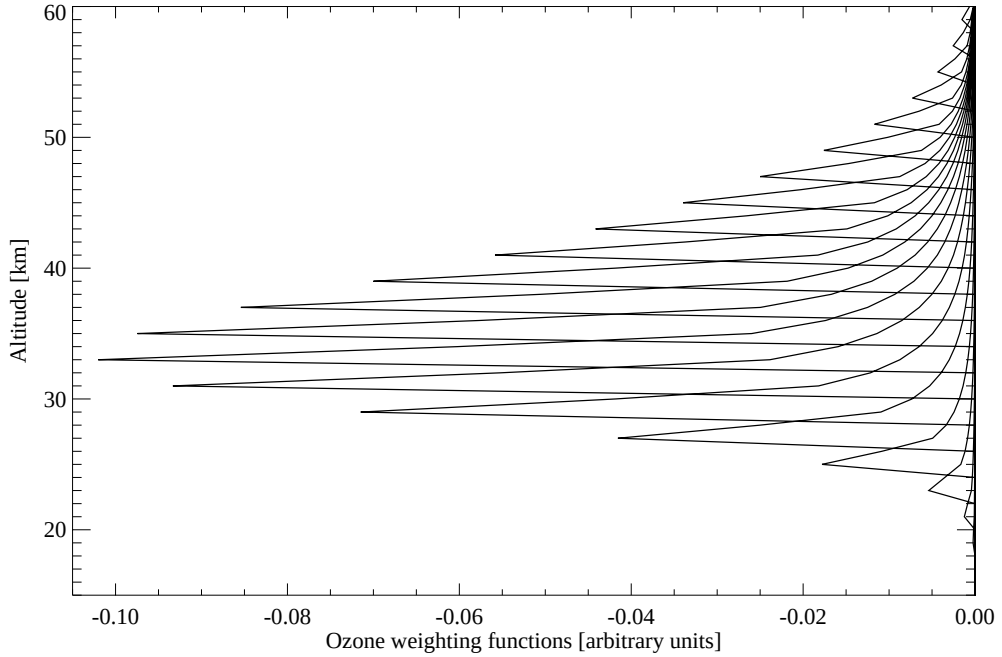

Figure 6.3: Ozone weighting functions at 328 nm for tangent heights from 15 km to 60 km in steps of 2 km.

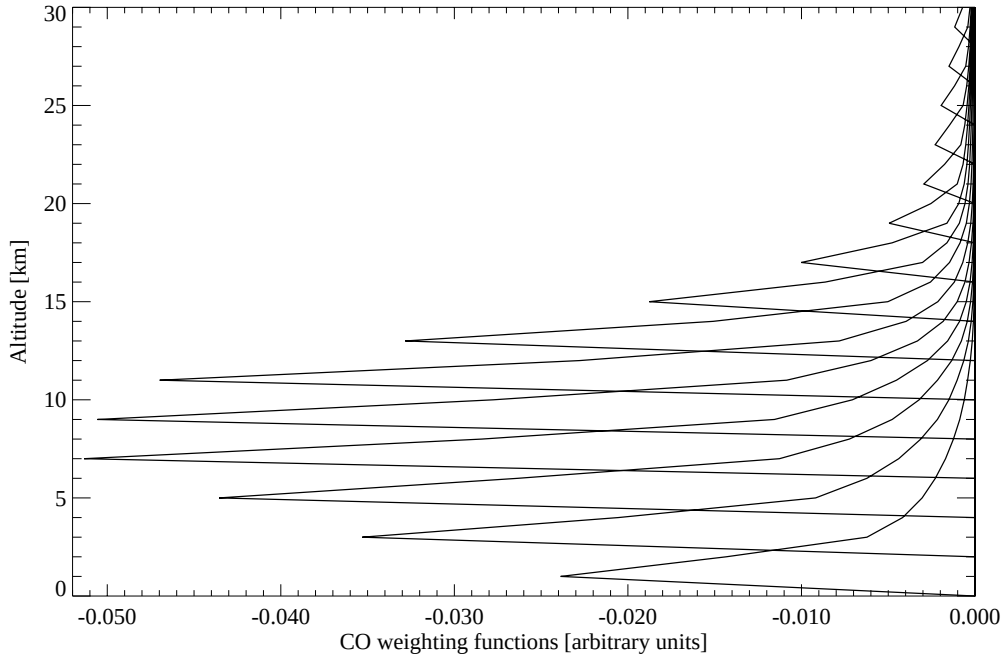

Figure 6.4: CO weighting functions at 2333.74 nm for tangent heights from 1 km to 30 km in steps of 2 km.

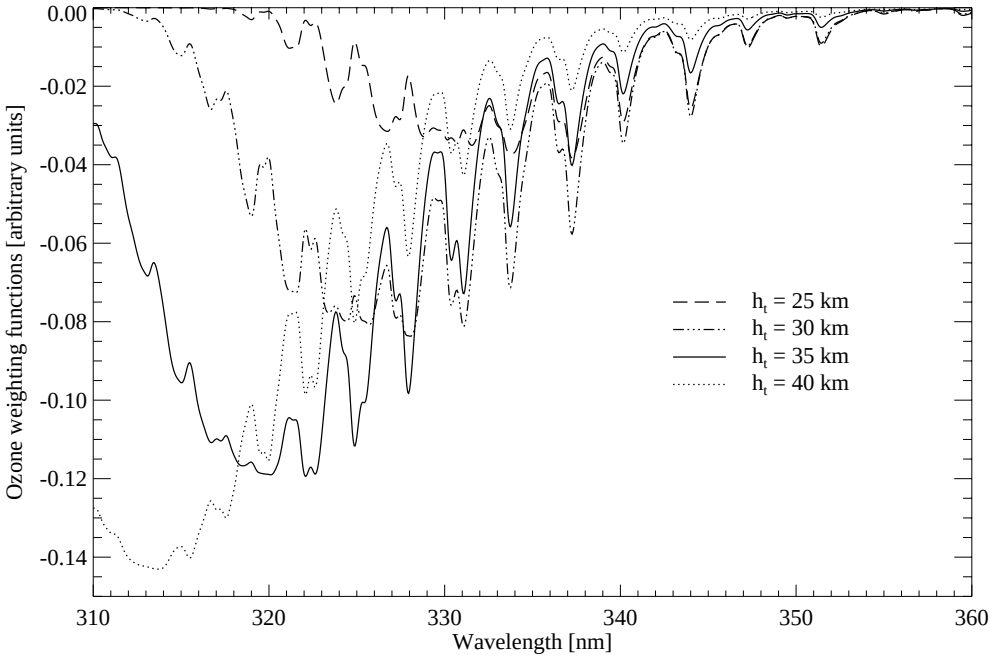

Figure 6.5: Ozone weighting functions as functions of wavelength for different tangent heights.

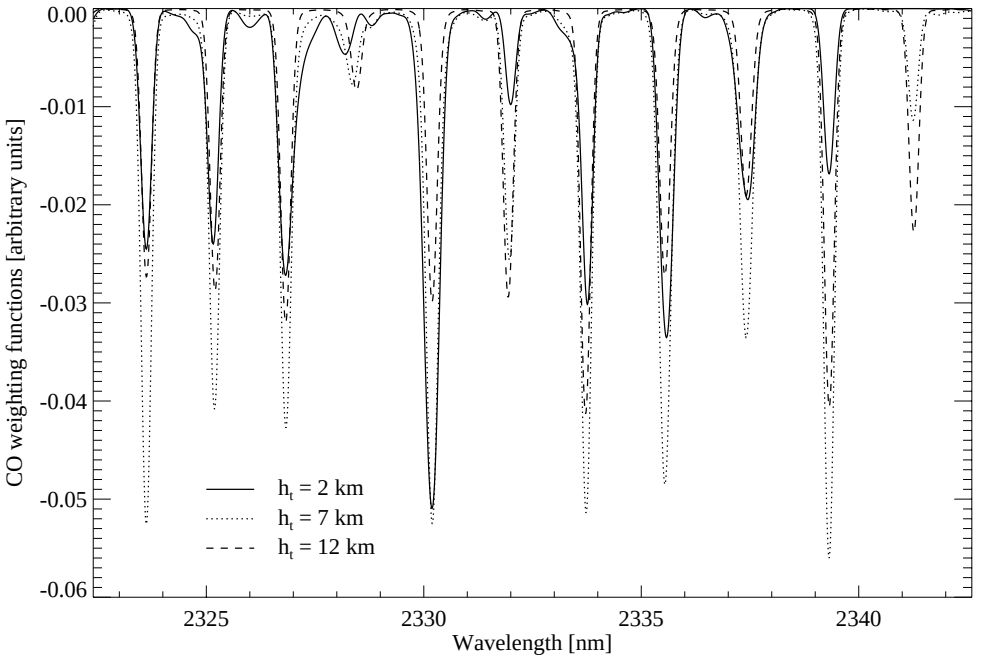

Figure 6.6: CO weighting functions as functions of wavelength for different tangent heights.

CO. All weighting functions are well peaked, uncorrelated, and have their maxima at the altitude which corresponds to the tangent height. The vertical resolution of the occultation measurements can be estimated analyzing the shape of the weighting functions. In the case under consideration, the vertical resolution is limited by the step of the internal altitude grid of the radiative transfer model and is about 1 - 1.5 km.

The spectral behavior of ozone and CO weighting functions for different tangent heights is shown in Figs. 6.5 and 6.6, respectively. At each tangent height and each wavelength, the maximum value of the corresponding weighting function is shown, i.e., according to Figs. 6.3 and 6.4, the value of the weighting function at the altitude corresponding to the tangent height. As clearly seen in Fig. 6.5, the spectral position of the maximum of ozone weighting functions depends strongly on the tangent height. So, for example, ozone weighting function at a tangent height of 40 km has its maximum at about 313 nm and rapidly decreases with the wavelength increasing, whereas the weighting function at a tangent height of 25 km has its maximum at about 331 nm and rapidly decreases with the wavelength decreasing. Thus, employing the multispectral measurements, the accuracy of ozone vertical distribution retrieval can be improved substantially. The strongest maxima of CO weighting functions take place at a tangent height of 7 km for most absorption lines, except for two lines at about 2332 nm and 2341.5 nm where the maximum sensitivity is reached at a tangent height of 12 km. The spectral behavior of CO weighting functions is determined mostly by the strong background absorption by CH_4 and H_2O.

6.3 Averaging kernels

Typical averaging kernels for stratospheric (ozone) and tropospheric (CO) trace gases calculated using Eq. (5.58) are shown in Fig. 6.7. The calculations were performed in spectral regions 310 - 360 nm and 2323 - 2342 nm for ozone and CO, respectively. An appropriate spectral resolution according to Table 2.1 was used in the forward simulations. Signal to noise ratio of 10000 was selected and the noise at different wavelengths was supposed to be uncorrelated. This means that the error covariance matrix, S_y, in Eq. (5.58) is a diagonal matrix with diagonal elements of 10^{-8}. As *a priori* covariance matrix, S_a, a diagonal matrix with diagonal elements of 0.04 was selected. The state vector, hence, was assumed to be *a priori* known with 20% uncertainty and no statistical information on the correlations between the trace gas number densities at different altitude levels was used. The state vector, $\mathbf{x}$, contains, in this case, the ozone or CO number densities at the discrete altitude levels from 0 to 60 km in step of 1 km. To clarify the representation, the averaging kernels are shown only for each third component of the state vector starting from 0 km for CO and from 6 km for ozone. The vertical resolution of the vertical profile retrieval algorithm characterized by the averaging kernel width can be estimated as 1.5 km. Above 50 km for ozone and 20 km for CO, the averaging kernels have relatively strong negative peaks. This means that anti-correlated perturbations are added to the solutions at neighboring altitude levels which lead to oscillations in the resulted vertical profiles. These oscillations can be substantially reduced introducing off-diagonal elements in the *a priori* covariance matrix,

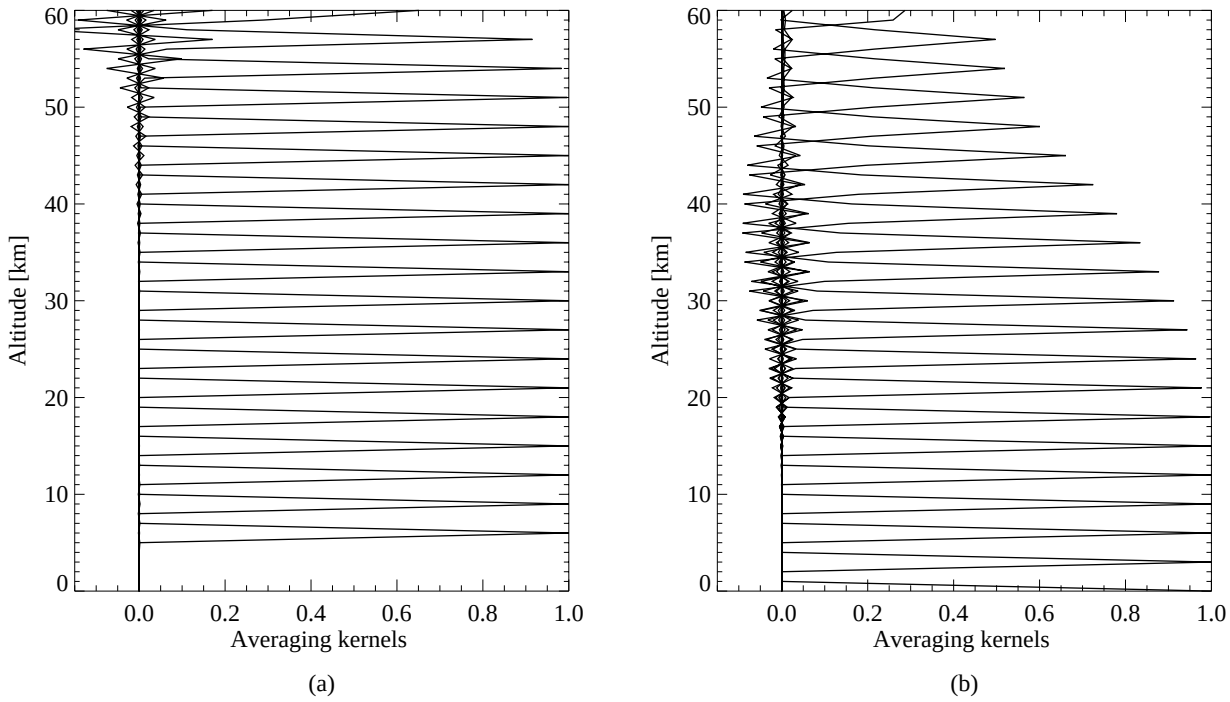

Figure 6.7: Averaging kernels for ozone (a) and CO (b) vertical profile retrieval in the spectral region 310 - 360 nm and 2323 - 2342 nm, respectively.

for example, as given by Eq. (5.79). These off-diagonal elements can also be derived using statistical information if available. At tangent heights above 30 km, the absorption features of CO in the transmission spectra become too weak compared to the noise. This results in loss of sensitivity of the measured radiation to the variations of CO number density and, therefore, the averaging kernels maxima are noticeably less than 1.0 at these altitude levels (see Fig. 6.7 (b)).

6.4 Theoretical precisions

Theoretical precisions of the retrieval of the atmospheric trace gas vertical distributions were computed according to Eqns. (5.55) and (5.56) using the same *a priori* covariance matrix as for the averaging kernels. The calculations were performed for ozone, CO, CH_4, CO_2, HCl, and NO_2.

Figure 6.8 shows ozone vertical distribution and theoretical precisions of ozone vertical profile retrieval. As for averaging kernels, the calculations were performed in the spectral region 310 - 360 nm with an appropriate spectral resolution. The theoretical precisions were computed for three different signal to noise ratios (measurement errors), namely, 10000, 1000, and 100, i.e., diagonal error covariance matrixes with diagonal elements 10^{-8}, 10^{-6}, and 10^{-4}, respectively, were used in Eq. (5.55). As clearly seen in Fig. 6.8 (b), in the absence of systematical errors, ozone vertical distribution can be retrieved with an

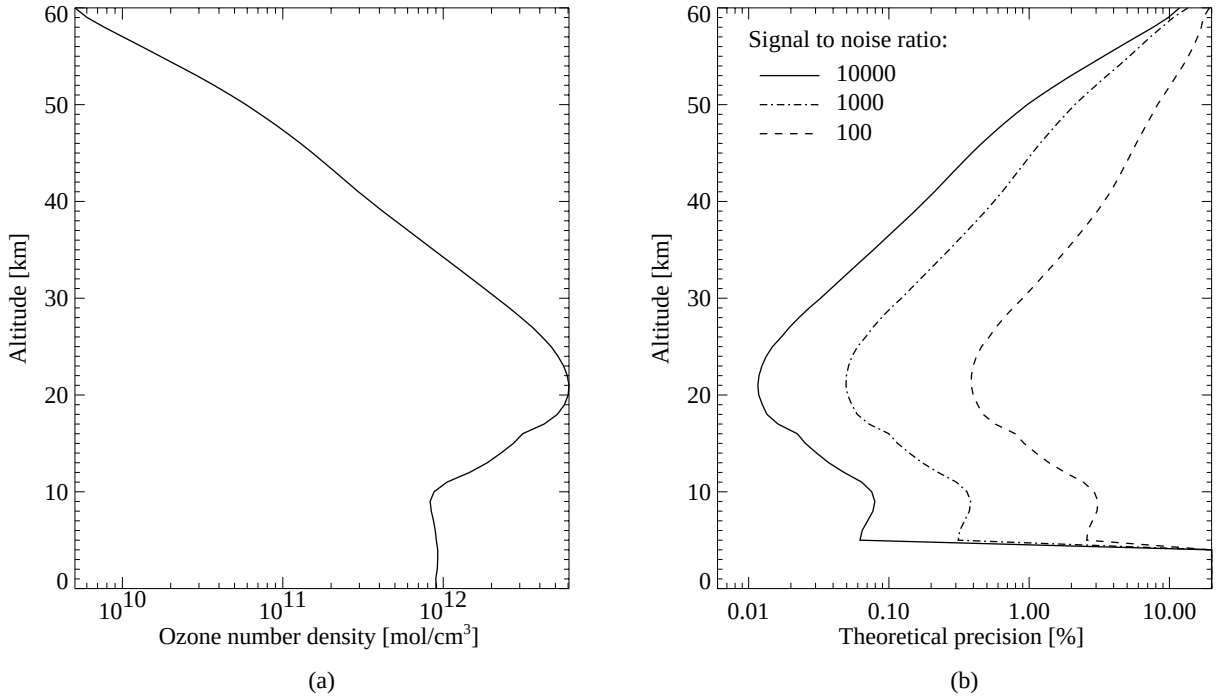

Figure 6.8: Ozone vertical distribution (a) and theoretical precisions of ozone vertical profile retrieval for different measurement errors (b).

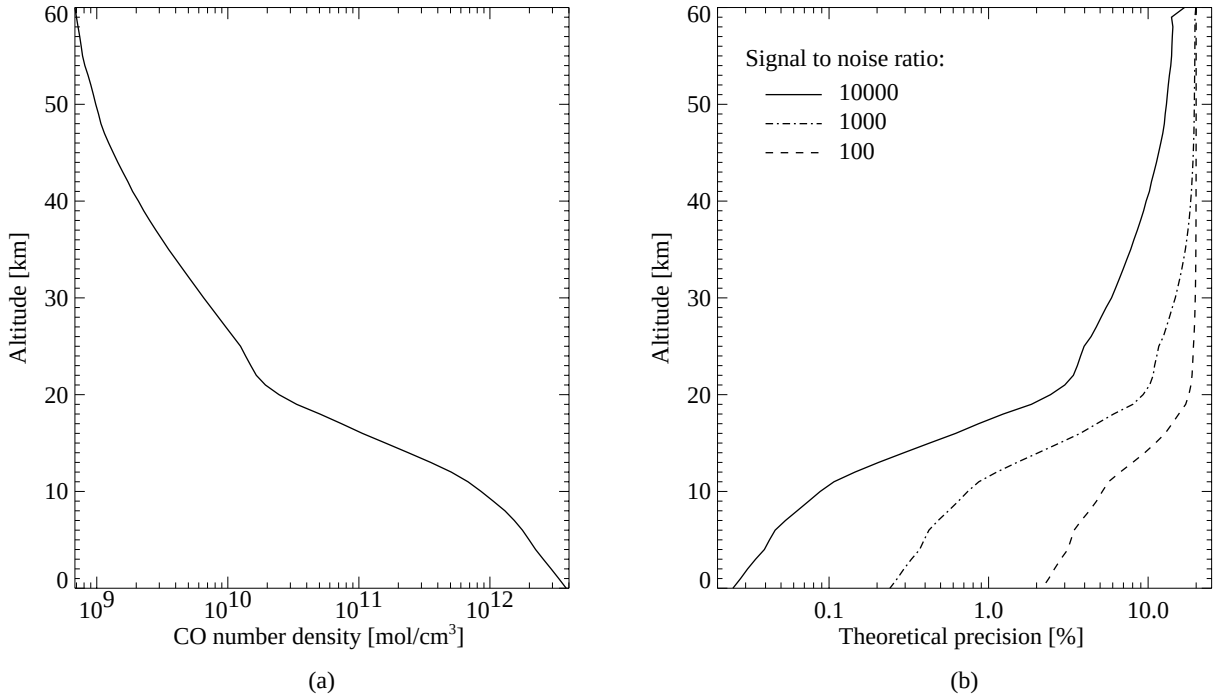

Figure 6.9: CO vertical distribution (a) and theoretical precision of CO vertical profile retrieval for different measurement errors (b).

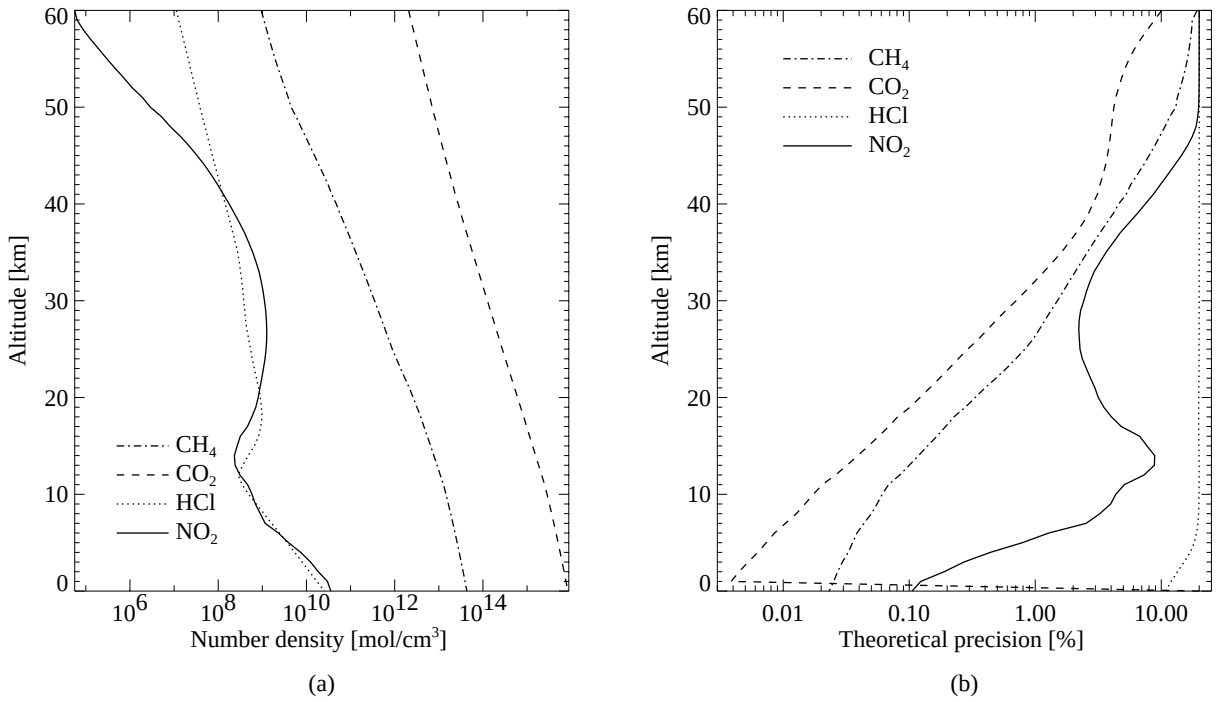

Figure 6.10: Vertical distributions (a) and theoretical precisions of the vertical profile retrieval (b) of some atmospheric trace gases.

accuracy of better than 1% from solar occultation measurements if the measurement error does not exceed 0.01%. Whereas for the measurement error of 1%, the theoretical precision of ozone vertical profile retrieval is expected to be between 0.5% and 10%. Due to strong ozone absorption no additional information about the ozone vertical distribution below 5 km can be obtained from occultation measurements in the selected spectral range.

Similar to Fig. 6.8, vertical distribution and theoretical precisions of the vertical profile retrieval for CO are shown in Fig. 6.9. The same spectral region and the same spectral resolution as for the averaging kernels were used for the calculations. For a signal to noise ratio of 10000, the vertical distribution of CO below 20 km can be retrieved with an accuracy of better than 3%, whereas above 20 km, the theoretical precision of retrieval decreases with the altitude to 15% at 50 km. Because of too weak absorption by CO, for a signal to noise ratio of 100, no additional information about CO vertical distribution above 20 km is obtained from the retrieval.

Vertical distributions and theoretical precisions of the vertical profile retrieval of some other atmospheric trace gases are shown in Fig. 6.10. All calculations were performed using signal to noise ratio of 1000. The following spectral regions were selected for retrieval: 425 - 460 nm, 1725 - 1753 nm, 1950 - 1970 nm, and 2280 - 2300 nm for NO_2, HCl, CO_2, and CH_4, respectively. An appropriate spectral resolution was used in each channel according to Table 2.1. Due to the strong absorption by CO_2 in the selected spectral region its vertical distribution can be retrieved with relatively high accuracy. Theoretical precision of the retrieval is about 0.005% for boundary layer and decreases with altitude to 2-3% at 40 km.

Altitude behavior of the theoretical precision of CH_4 vertical distribution retrieval is similar to that of CO_2 but the precision is lower due to weaker absorption. Vertical distribution of NO_2 can be retrieved with an accuracy better than 1% only in boundary layer, whereas in the altitude region 5 - 40 km a theoretical precision of 1 - 10 % is achieved. Because of too weak absorption, vertical distribution of HCl can not be estimated from solar occultation measurements for the selected signal to noise ratio. Only some information about HCl abundance in boundary layer can be obtained.

Thus, as follows from the discussion above, the theoretical precision of trace gas vertical profile retrieval depends strongly on trace gas abundance, on the strength of its absorption features in the selected spectral region, and on the signal to noise ratio in the measured spectra.

Part III

Scattered solar radiance

Chapter 7

The CDIPI spherical radiative transfer model

7.1 Choice of coordinates

In general, the intensity of the radiation is a function of three spatial variables, which define the point in the medium where the radiance is calculated, and two angular variables, which determine the direction of the radiation. Therefore, two coordinate systems have to be specified to define the spatial position and the local directional orientation.

Since the considered radiative transfer model describes the radiation field in a spherical planetary atmosphere, it is reasonable to use a spherical coordinate system having its center in the center of the planet as spatial (global) coordinate system. The Z-axis of the associated Cartesian coordinate system points towards the Sun. For a spherical shell atmosphere, this leads to an azimuthal symmetric radiation field. The X-axis (or Y-axis) of the coordinate system can be selected arbitrarily. The directional (local) coordinate system, which is also a spherical coordinate system, has to be chosen to set the directional polar axis (z-axis of the associated Cartesian coordinate system) normal to any boundary surface. Thus, the azimuthal plane has to be tangential to any boundary discontinuity surface of the radiance (if any exists). Such a choice of the local coordinate system avoids the discontinuity of intensity as a function of azimuth angle. The x-axis is chosen to be in the plane defined by the Z-axis of the spatial coordinate system and the z-axis of the directional coordinate system. All angles are defined with respect to the radiance direction, thus, the $\Theta = 0^\circ$ direction corresponds to the upward radiance and the $\Theta = 180^\circ$ direction to the downward radiance.

Using these coordinate systems, the set of coordinates r, Ψ, Φ, Θ, and φ at any point in the atmosphere matches the corresponding coordinate set in a plane-parallel radiative transfer model. Thus, the radiances calculated in a spherical and in a plane-parallel atmosphere can be directly compared.

Figure 7.1 depicts the global and the local coordinate systems, selected as discussed above, for two arbitrary points on the instrument line-of-sight. As an illustration, the

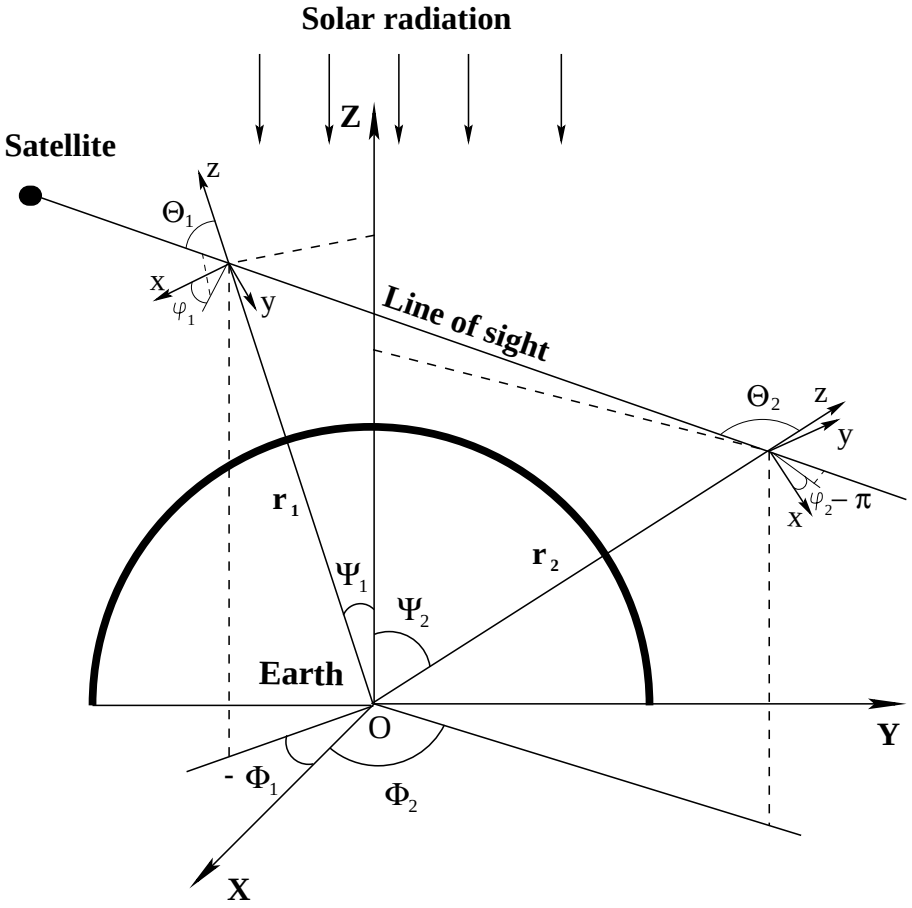

Figure 7.1: Global (XYZ) and local (xyz) spherical coordinate systems.

reorientation of the directional coordinate system along a line-of-sight for limb viewing geometry is shown.

7.2 Numerical aspects of radiative transfer calculation

As discussed in Section 3.1, the radiation field $I(r, \Psi, \Phi, \Theta, \varphi)$ in Eq. (4.41) can be split into two components: the direct radiation, which is never scattered in the atmosphere or reflected from the planetary surface, and the diffuse radiation, which is scattered or reflected at least once. In the coordinates depicted in Fig. 7.1, the intensity of the direct solar radiation given by Eq. (3.18) can be calculated as follows:

$$I_{dir}(r, \Psi, \Phi, \Theta, \varphi) = F_0 \, \delta(\cos\Theta + \cos\Psi, \varphi) \, \exp\left(- \int_0^{s_o} \alpha(\hat{s}) \, d\hat{s} \right) , \qquad (7.1)$$

where F_0 is the incident solar flux and s_o denotes the full path-length along the direct solar beam from the top of the atmosphere to point $\mathbf{r}$.

Rewriting Eq. (4.41), the following equation for the intensity of diffuse radiation can be obtained:

$$I_{dif}(\mathbf{r}, \mathbf{e}_s) = I_{dif}(\mathbf{r}_o, \mathbf{e}_s)\, e^{-\tau(s_c)} + \int_0^{s_c} J(\tilde{\mathbf{r}}, \tilde{\mathbf{e}_s})\, \alpha(\tilde{\mathbf{r}})\, e^{-\tau(s)} ds \;, \tag{7.2}$$

where $I_{dif}(\mathbf{r}_o, \mathbf{e}_s)$ is the diffuse radiance at the end of the characteristic (line-of-sight), i.e., at the boundary (the top or the bottom) of the atmosphere, in direction $\mathbf{e}_s$, s_c is the full length of the characteristic, and $\tau(s)$ is the optical depth given by

$$\tau(s) = \int_0^s \alpha(\tilde{s})\, d\tilde{s} \;. \tag{7.3}$$

According to the boundary conditions, $I_{dif}(\mathbf{r}_o, \mathbf{e}_s)$ is set to zero for the downward radiation at the top of the atmosphere and describes at the bottom of the atmosphere the upward radiation, which is reflected from the Earth's surface. Thus, the first term in Eq. (7.2) is always equal to zero for upwards pointing line-of-sights as well as for downwards pointing line-of-sights which do not intersect the Earth's surface.

As discussed in Section 3.1, Eqns. (3.24)–(3.26), the source function $J(\tilde{r}, \tilde{\Psi}, \tilde{\Phi}, \tilde{\Theta}, \tilde{\varphi})$ in Eq. (7.2) can be split into the multiple scattering and the single scattering source functions. In the selected coordinate system, according to Eqns. (3.64) and (3.65), these source functions are given by

$$J_{ms}(\tilde{r}, \tilde{\Psi}, \tilde{\Phi}, \tilde{\Theta}, \tilde{\varphi}) = \frac{\varpi(\tilde{r}, \tilde{\Psi}, \tilde{\Phi})}{4\pi} \int_0^{2\pi} d\hat{\varphi} \int_0^{\pi} d\hat{\Theta}\, \sin\hat{\Theta}\, p(\tilde{r}, \tilde{\Psi}, \tilde{\Phi}, \gamma)\, I_{dif}(\tilde{r}, \tilde{\Psi}, \tilde{\Phi}, \hat{\Theta}, \hat{\varphi}) \tag{7.4}$$

and

$$J_{ss}(\tilde{r}, \tilde{\Psi}, \tilde{\Phi}, \tilde{\Theta}, \tilde{\varphi}) = \frac{\varpi(\tilde{r}, \tilde{\Psi}, \tilde{\Phi})}{4\pi}\, F_0\, p(\tilde{r}, \tilde{\Psi}, \tilde{\Phi}, \gamma_o)\, \exp\left(- \int_0^{s_t} \alpha(\hat{s})\, d\hat{s} \right) \;, \tag{7.5}$$

respectively, where γ and γ_0 are appropriate scattering angles according to Eqns. (3.66) and (3.67):

$$\gamma = \cos\tilde{\Theta}\, \cos\hat{\Theta} + \sin\tilde{\Theta}\, \sin\hat{\Theta}\, \cos(\tilde{\varphi} - \hat{\varphi}) \tag{7.6}$$

and

$$\gamma_o = -\cos\tilde{\Theta}\, \cos\tilde{\Psi} + \sin\tilde{\Theta}\, \sin\tilde{\Psi}\, \cos\tilde{\varphi} \;. \tag{7.7}$$

The angle between the direct solar beam and the characteristic, γ_o, is constant along the characteristic in any atmospheric model which neglects refraction effects. The integration in Eq. (7.5) is performed along the direct solar beam and s_t, hence, denotes the full length of the integration line from point **r** to the top of the atmosphere along the beam.

Neglecting the refraction effects, the spatial coordinates of any point on the characteristic, $\tilde{r}, \tilde{\Psi}$ and $\tilde{\Phi}$, and the local direction of the radiance in this point, defined by $\tilde{\Theta}$ and $\tilde{\varphi}$, can be calculated from the initial set of variables r, Ψ, Φ, Θ and φ using the following formulas (details are given in the Appendix B):

$$\tilde{r} = \sqrt{r^2 - 2\,r\,s\,\cos\Theta + s^2}\;, \tag{7.8}$$

$$\cos\tilde{\Theta} = \frac{r\,\cos\Theta - s}{\tilde{r}}\;, \tag{7.9}$$

$$\cos\tilde{\Psi} = \frac{r\,\cos\Psi - s\,\zeta_0}{\tilde{r}}\;, \tag{7.10}$$

$$\cos\tilde{\Phi} = \frac{r\sin\Psi}{\tilde{r}\sin\tilde{\Psi}}\cos\Phi - \frac{s}{\tilde{r}\sin\tilde{\Psi}}\,\eta_0\;, \tag{7.11}$$

$$\cos\tilde{\varphi} = \frac{\cos\tilde{\Psi}\,\cos\tilde{\Theta} - \zeta_0}{\sin\tilde{\Psi}\,\sin\tilde{\Theta}}\;, \tag{7.12}$$

where

$$\eta_0 = \cos\Psi\cos\Phi\sin\Theta\cos\varphi - \sin\Phi\sin\Theta\sin\varphi + \sin\Psi\cos\Phi\cos\Theta\;,$$

and

$$\zeta_0 = \cos\Psi\,\cos\Theta - \sin\Psi\,\sin\Theta\,\cos\varphi\;.$$

The set of variables $\hat{\Theta}$ and $\hat{\varphi}$ is chosen according to the numerical integration rule selected to calculate the angular integral in Eq. (7.4), for example, Gaussian quadrature for $\cos\hat{\Theta}$ and evenly spaced azimuth angles $\hat{\varphi}$. A commonly used approach to perform angular integration is to employ the Fourier expansion with respect to azimuth angle, as it was done in [*Rozanov et al.*, 1997], or spherical harmonics, as it was done in [*Evans*, 1998]. Such methods are very efficient in the plane-parallel case but are too slow for spherical geometry because of the change of all angles along the integration line [*Balluch*, 1996]. In the CDIPI model the optimal set of nodes $\hat{\Theta}$ and $\hat{\varphi}$, as proposed by *Steinacker et al.* [1996], has been used to calculate the angular integral in Eq. (7.4). This set of nodes enables the integration to be performed with a minimum number of nodes for a given accuracy. The nodes and the corresponding integration weights have been supplied by J. Steinacker, MPG Research Unit "Dust in Star–Forming Regions", Jena, Germany.

Since the multiple scattering source function $J_{ms}(\tilde{r}, \tilde{\Psi}, \tilde{\Phi}, \tilde{\Theta}, \tilde{\varphi})$ is a functional of generally unknown function $I_{dif}(\tilde{r}, \tilde{\Psi}, \tilde{\Phi}, \tilde{\Theta}, \tilde{\varphi})$, the Picard iterative approximation (as discussed in Section 4.2) is applied to solve the radiative transfer equation for diffuse radiance (Eq. (7.2)). Rewriting the equation for the Picard iterative approximation, Eq. (4.47), the

following iterative scheme is obtained:

$$I_{dif}^{(n)}(\hat{r},\hat{\Psi},\hat{\Phi},\hat{\Theta},\hat{\varphi}) \xrightarrow{\text{interpolation}} I_{dif}^{(n)}(\tilde{r},\tilde{\Psi},\tilde{\Phi},\hat{\Theta},\hat{\varphi}) \tag{7.13}$$

$$\downarrow$$

$$J_{ms}^{(n)}(\tilde{r},\tilde{\Psi},\tilde{\Phi},\tilde{\Theta},\tilde{\varphi}) = \mathrm{L_a} I_{dif}^{(n)}(\tilde{r},\tilde{\Psi},\tilde{\Phi},\hat{\Theta},\hat{\varphi}) \tag{7.14}$$

$$\downarrow$$

$$I_{dif}^{(n+1)}(\hat{r},\hat{\Psi},\hat{\Phi},\hat{\Theta},\hat{\varphi}) = \mathfrak{I}(\hat{r},\hat{\Psi},\hat{\Phi},\hat{\Theta},\hat{\varphi}) + \mathrm{L_s^{sp}} J_{ms}^{(n)}(\tilde{r},\tilde{\Psi},\tilde{\Phi},\tilde{\Theta},\tilde{\varphi})\ . \tag{7.15}$$

Here, $\mathfrak{I}(\hat{r},\hat{\Psi},\hat{\Phi},\hat{\Theta},\hat{\varphi})$ contains all terms of the radiative transfer equation, which require no iteration to be calculated and remain unchanged during the iterations. The variables $\hat{r}$, $\hat{\Psi}$, and $\hat{\Phi}$ in Eqns. (7.13)–(7.15) denote spatial grid values, and the variables $\hat{\Theta}$ and $\hat{\varphi}$ are integration nodes, as described above. According to Eqns. (4.48)–(4.50), the intensity of diffuse radiation calculated in a pseudo-spherical atmosphere is used as an initial guess. This pseudo-spherical intensity is computed using the GOMETRAN radiative transfer model [*Rozanov et al.*, 1997] which, as discussed is Section 3.5, assumes a plane-parallel atmosphere for diffuse radiation and a spherical atmosphere for direct solar radiation. Using such an initial estimate of the radiation field, convergence can be achieved after a few iterations.

In fact, for most applications, not the complete radiation field but only the intensity of the radiation at certain points in certain directions (r', Ψ', Φ', Θ', φ'), which are usually defined by the user, is required. These user–defined coordinates and directions do not have to match the spatial grid values $\hat{r}$, $\hat{\Psi}$, and $\hat{\Phi}$ as well as integration nodes $\hat{\Theta}$ and $\hat{\varphi}$, which are chosen to achieve maximum computational efficiency for a given accuracy. This means that additional integrations have to be done for user–defined line-of-sights and the iteration scheme given by Eqns. (7.13)–(7.15) can be rewritten as follows:

$$I_{dif}^{(n)}(\hat{r},\hat{\Psi},\hat{\Phi},\hat{\Theta},\hat{\varphi}) \xrightarrow{\text{interpolation}} I_{dif}^{(n)}(\tilde{r},\tilde{\Psi},\tilde{\Phi},\hat{\Theta},\hat{\varphi}) \tag{7.16}$$

$$\downarrow$$

$$J_{ms}^{(n)}(\tilde{r},\tilde{\Psi},\tilde{\Phi},\tilde{\Theta},\tilde{\varphi}) = \mathrm{L_a} I_{dif}^{(n)}(\tilde{r},\tilde{\Psi},\tilde{\Phi},\hat{\Theta},\hat{\varphi}) \tag{7.17}$$

$$\downarrow$$

$$I_{dif}^{(n+1)}(r',\Psi',\Phi',\Theta',\varphi') = \mathfrak{I}(r',\Psi',\Phi',\Theta',\varphi') + \mathrm{L_s^{sp}} J_{ms}^{(n)}(\tilde{r},\tilde{\Psi},\tilde{\Phi},\tilde{\Theta},\tilde{\varphi}) \tag{7.18}$$

$$I_{dif}^{(n+1)}(\hat{r},\hat{\Psi},\hat{\Phi},\hat{\Theta},\hat{\varphi}) = \mathfrak{I}(\hat{r},\hat{\Psi},\hat{\Phi},\hat{\Theta},\hat{\varphi}) + \mathrm{L_s^{sp}} J_{ms}^{(n)}(\tilde{r},\tilde{\Psi},\tilde{\Phi},\tilde{\Theta},\tilde{\varphi}) \tag{7.19}$$

In order to achieve convergence of the radiance at the user–defined points in the user–defined directions, only convergence of the source function along the user-defined line-of-sights is required, whose sensitivity to the radiation field in remote points of the atmosphere is rejected by the exponential term in the integral operator L_s^{sp}. Therefore, the convergence criteria can be substantially loosened. Once the convergence has been achieved, the last

step given by Eq. (7.19) needs no longer to be performed. This makes the last iteration much less computer–time consuming than the previous ones.

The number of iterations needed to obtain convergence was found to be weakly dependent on viewing geometry, selected model atmosphere, wavelength, and so on. Therefore, the required number of iterations can be once determined and then used as model input parameter. Using this approach, the step given by Eq. (7.18) can be skipped for any intermediate iteration and the step given by Eq. (7.19) needs not to be performed for the last iteration. This makes the radiative transfer model two times faster for commonly used viewing geometries and model atmospheres.

The iteration, which involves the steps given by Eqns. (7.16), (7.17), and (7.19) will be further called "global iteration", in contrast to the last iteration, which involves the steps given by Eqns. (7.16), (7.17), and (7.18). Solving only the system of equations (7.16)–(7.18), i.e., performing no global iteration, leads to the Combined Differential–Integral (CDI) approach described in [*Rozanov et al.*, 2000a].

In the present version of the radiative transfer model, the dependence of the radiance, the source function, and all atmospheric parameters on global azimuth angle Φ is neglected, i.e., a spherical shell atmosphere is considered. No refraction effects were taken into account.

7.3 Simulated radiance

Typical spectra of Sun-normalized diffuse radiation at the top of the atmosphere for different tangent heights are shown in Fig. 7.2. The spectra were simulated for a solar zenith angle of 30° and an azimuth angle of 90° with the CDIPI model performing one global iteration; that is, following the notation in Section 7.2, $I_{dif}^{(2)}$ was calculated. The incident solar flux was assumed to be equal π. All angles refer to the top of the atmosphere. The computations were done including the absorption by ozone, NO_2, and O_4 as well as aerosol and Rayleigh scattering. The 1976 US Standard model atmosphere [*NASA*, 1976] with the top of the atmosphere set at 100 km was used. A maritime aerosol in the boundary layer and a background aerosol in the stratosphere according to the LOWTRAN/MODTRAN aerosol parameterization [*Kneizys et al.*, 1996] was selected. The calculations were performed using a surface albedo of 0.3.

The diffuse radiation at the top of the atmosphere as a function of tangent height is shown in Fig. 7.3. The calculations were carried out at 500 nm at a solar zenith angle of 80° for two azimuth angles. The radiation was computed for two atmospheric scenarios: (a) including only Rayleigh scattering and ozone absorption and (b) including aerosol and Rayleigh scattering as well as ozone absorption. Figure 7.3 clearly illustrates the increase of the intensity of diffuse radiation, as well as the peak in the troposphere, for an azimuth angle of 0° caused by the forward scattering at aerosol particles. Assuming an aerosol–free atmosphere, a small descent takes place below a tangent height of 10 km. For an azimuth angle of 180°, the behavior of both curves is determined by the back scattering properties of aerosol particles or molecules. Since, for the back scattering, the Henyey–Greenstein phase

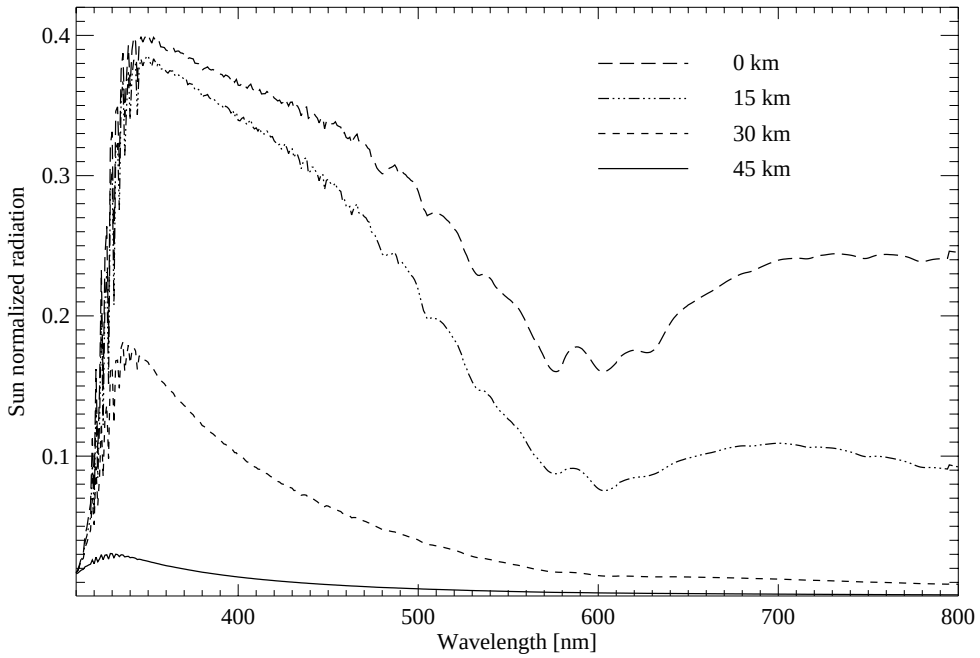

Figure 7.2: Sun-normalized diffuse radiation at the top of the atmosphere at a solar zenith angle of 30° and an azimuth angle of 90° for different tangent heights.

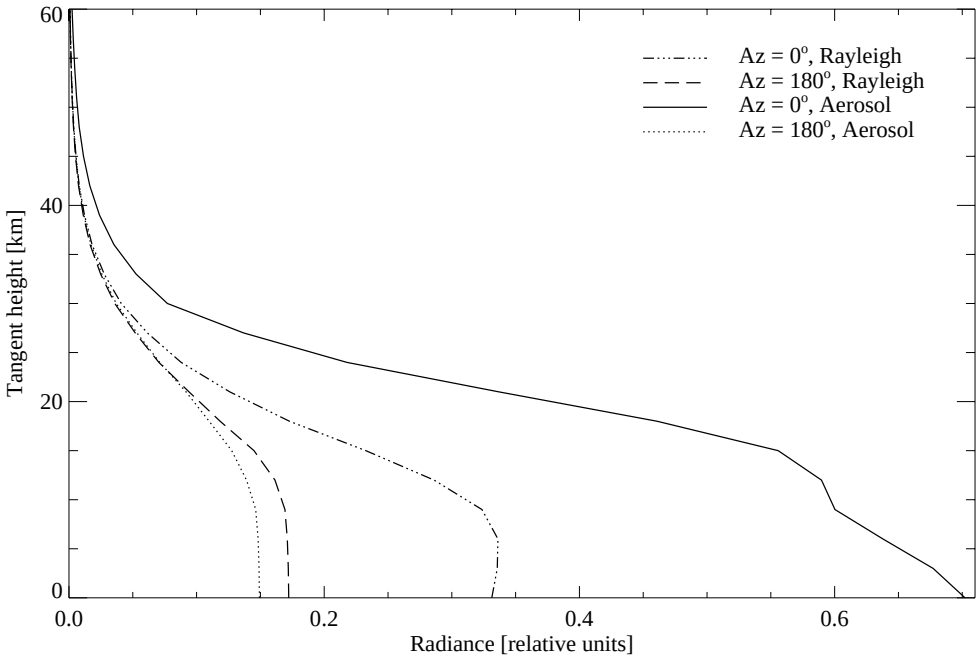

Figure 7.3: Diffuse radiation at the top of the atmosphere at a solar zenith angle of 80° for azimuth angles of 0° and 180° as a function of tangent height with and without aerosol scattering.

function, which was used here to describe the aerosol scattering properties, is similar to the Rayleigh phase function, both curves show a similar dependence on the tangent height. The radiation calculated including aerosols is, however, weaker because of additional aerosol extinction.

7.4 Convergence of the iterative scheme

As mentioned previously, using the pseudo-spherical radiative field as an initial guess causes the iterative scheme to converge rapidly, i.e., after 1–2 global iterations. In order to estimate the accuracy achieved after each iteration, the solutions after the first and the second global iteration were compared.

The relative difference between the CDIPI solutions performing two and one global iterations, i.e., $(I_{dif}^{(3)}/I_{dif}^{(2)} - 1) * 100\%$, as a function of wavelength for different tangent heights is shown in Fig. 7.4. The computations were done at a solar zenith angle of 30° and an azimuth angle of 90° for the same atmospheric scenario as for Fig. 7.2.

The same relative difference as a function of tangent height at solar zenith angles of 30° and of 80° is shown in Fig. 7.5 and Fig. 7.6, respectively. The calculations were performed at 500 nm for three azimuth angles with and without aerosol scattering. The atmospheric scenarios as in Fig. 7.3 were used. The difference between the solutions never exceeds 0.2% and depends only slightly on the selected atmospheric scenario, solar zenith angle, and azimuth angle.

Figure 7.7 shows the relative difference as a function of solar zenith and azimuth angle at a tangent height of 30 km. The calculations were carried out for 19 azimuth angles (0°–180° in steps of 10°) and 11 solar zenith angles (0°–90° in steps of 10° and 95°). As will be explained in Section 7.6.4, azimuth angles between 140° and 180° at a solar zenith angle of 90° and between 70° and 180° at a solar zenith angle of 95° have not been considered. The computations were performed including ozone absorption and Rayleigh scattering.

The relative difference shown in Figs. 7.4–7.7 never exceeds 0.2%. Thus, performing only one global iteration yields a spherical solution with an accuracy sufficient for most applications.

7.5 The CDI solution for the limb viewing geometry

As mentioned in Section 7.2, performing no global iteration leads to the CDI solution, i.e., $I_{dif}^{(1)} \equiv I_{dif}^{CDI}$. For non-limb viewing geometry, as shown in [*Rozanov et al.*, 2000a], the CDI and the spherical solutions differ by less than 2%. Although the CDI approach was developed to simulate off-nadir measurements, it can be also used to obtain a fast approximation for scattered solar radiation in limb viewing geometry. Similar approaches which involve an accurate consideration of the single scattering term and an approximation for the multiple scattering term have already been used for modeling of scattered solar radiation in the Earth's atmosphere [*Naudet and Thomas*, 1987; *Anderson and Lloyd*, 1990; *McLinden et al.*, 1999; *Abreu et al.*, 1989]. Thus, it is of interest to estimate the

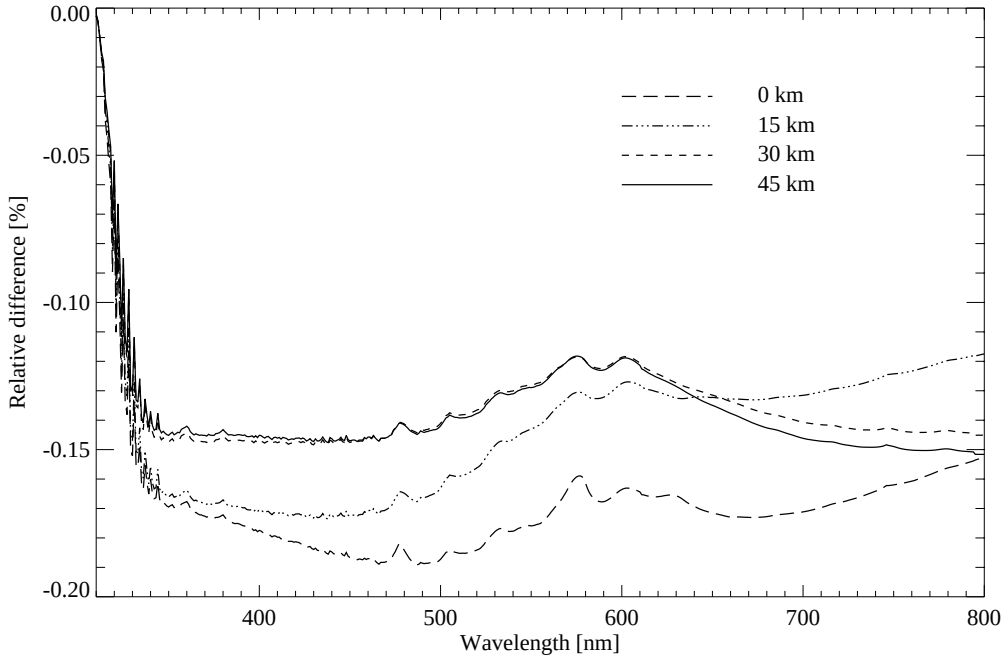

Figure 7.4: Relative difference between the CDIPI solutions performing three and two iterations, i.e., $(I_{dif}^{(3)}/I_{dif}^{(2)} - 1) * 100\%$, as a function of wavelength at a solar zenith angle of 30° and an azimuth angle of 90° for different tangent heights.

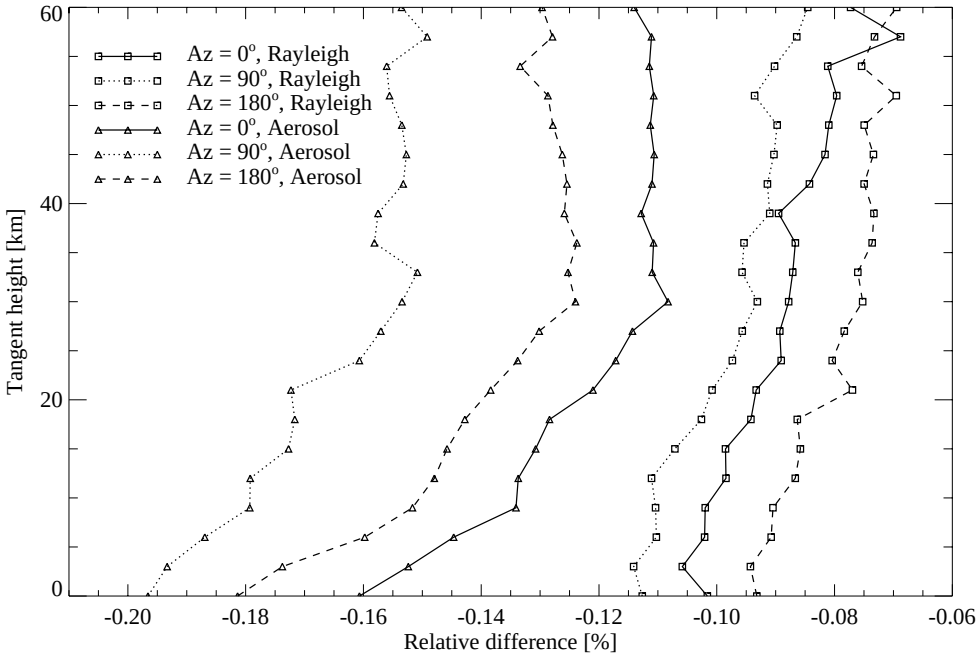

Figure 7.5: Relative difference between the CDIPI solutions performing three and two iterations as a function of tangent height for a solar zenith angle of 30° and three azimuth angles with and without aerosol scattering.

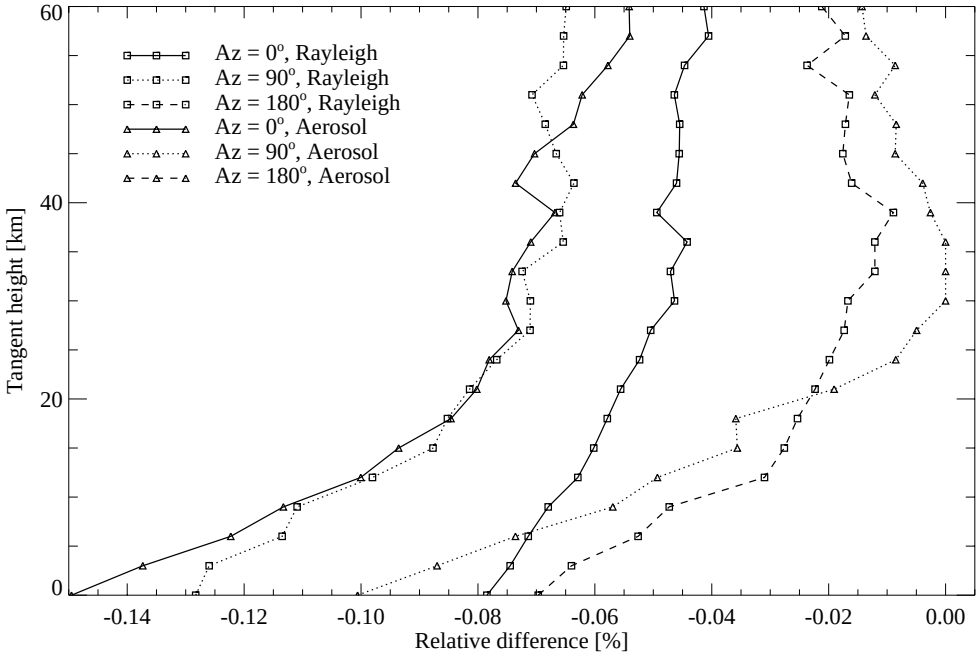

Figure 7.6: As Fig. 7.5, but for a solar zenith angle of 80°.

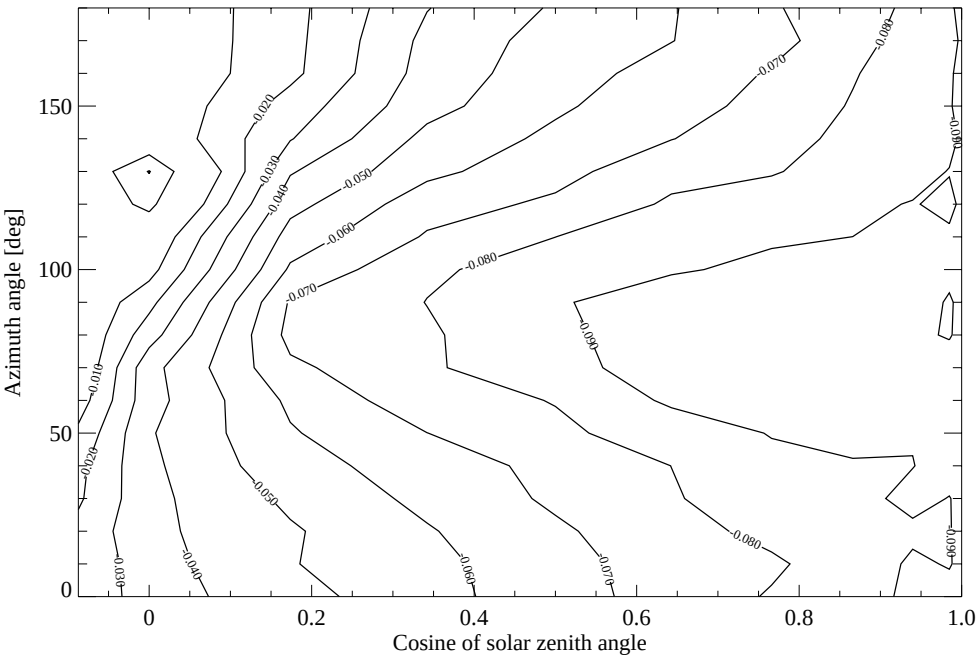

Figure 7.7: Relative difference between the CDIPI solutions performing three and two iterations, i.e., $(I_{dif}^{(3)}/I_{dif}^{(2)} - 1) * 100\%$, as a function of solar zenith angle and azimuth angle at 30 km tangent height.

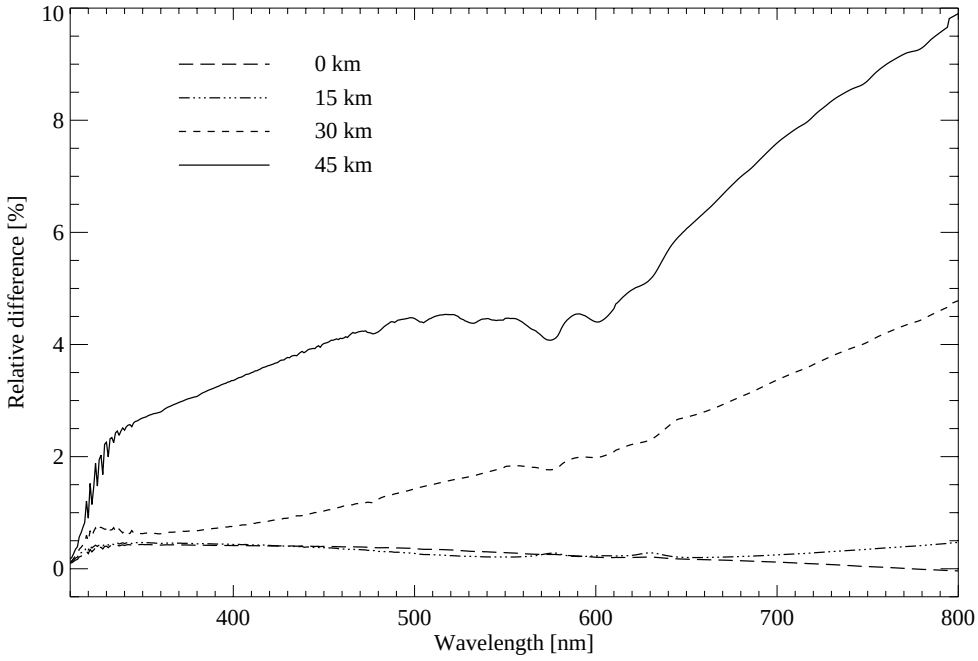

Figure 7.8: Relative difference between the CDI and the spherical solutions, i.e., $(I_{dif}^{(1)}/I_{dif}^{(2)} - 1) * 100\%$, as a function of wavelength at a solar zenith angle of 30° and an azimuth angle of 90° for different tangent heights.

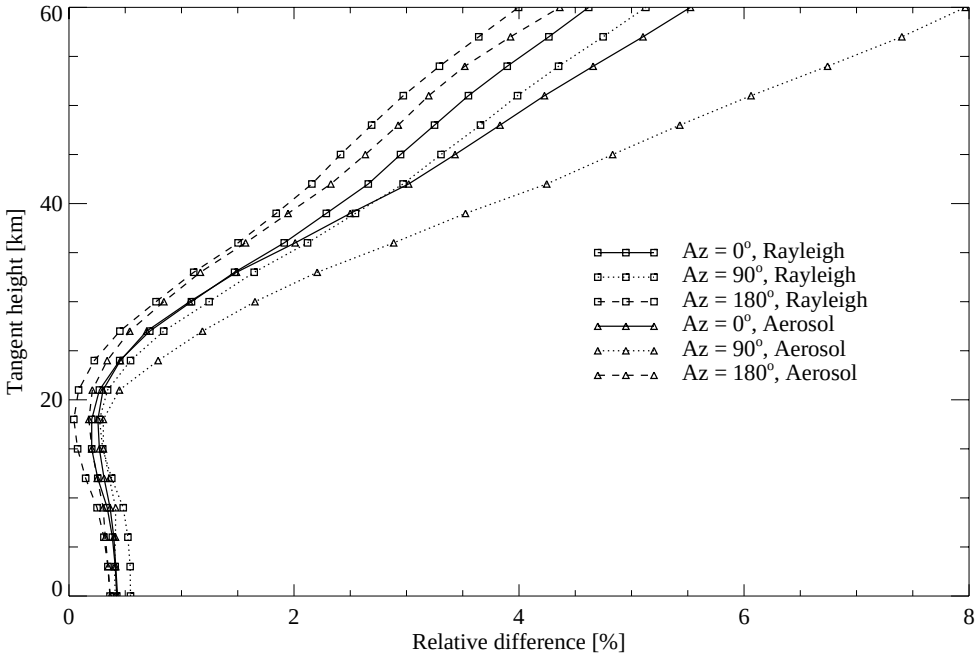

Figure 7.9: Relative difference between CDI and CDIPI, i.e., $(I_{dif}^{(1)}/I_{dif}^{(2)} - 1) * 100\%$, as a function of tangent height for a solar zenith angle of 30° and three azimuth angles with and without aerosol scattering.

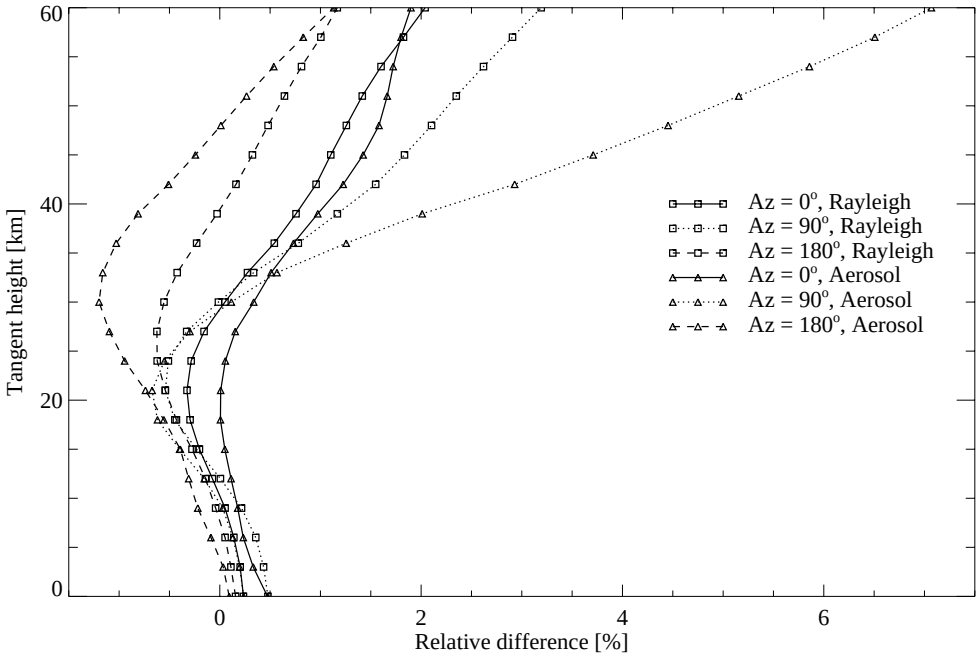

Figure 7.10: As Fig. 7.9, but for a solar zenith angle of 80°.

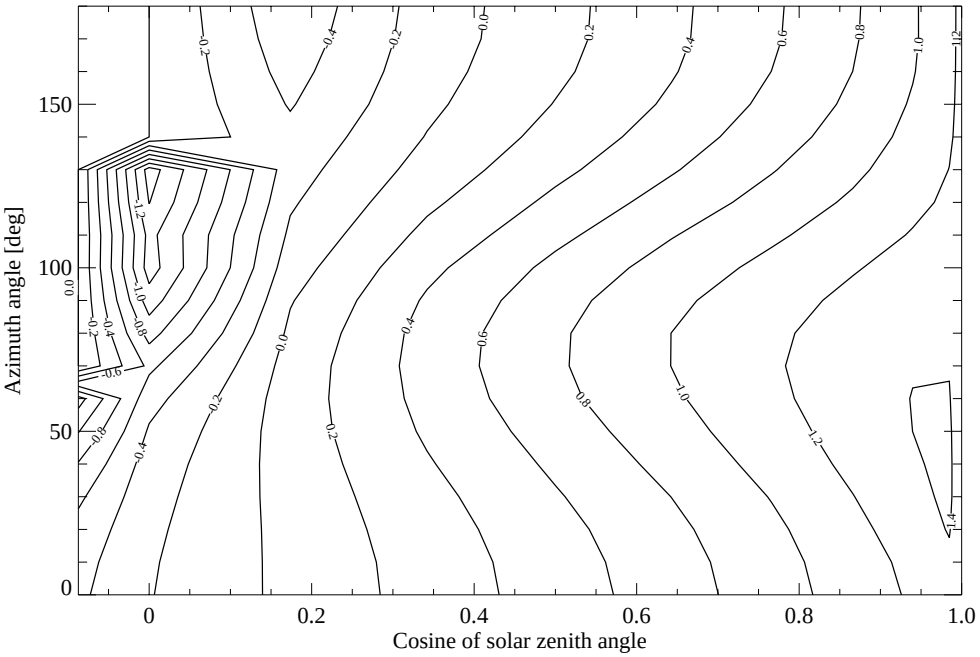

Figure 7.11: Relative difference between CDI and CDIPI, i.e., $(I_{dif}^{(1)}/I_{dif}^{(2)} - 1) * 100\%$, as a function of solar zenith angle and azimuth angle at 30 km tangent height.

accuracy of the diffuse radiation computed with the CDI radiative transfer model in limb viewing geometry.

The relative difference between the CDI and the spherical solution, i.e., $(I_{dif}^{(1)}/I_{dif}^{(2)} - 1) * 100\%$, as a function of wavelength for different tangent heights is shown in Fig. 7.8. The computations were done at a solar zenith angle of 30° and an azimuth angle of 90° for the same atmospheric scenario as in Fig. 7.2. The relative difference increases with wavelength and tangent height to 10% at 800 nm and a tangent height of 45 km.

The same relative difference as a function of tangent height at solar zenith angles of 30° and of 80° is shown in Fig. 7.9 and Fig. 7.10, respectively. The calculations were performed at 500 nm for three azimuth angles with and without aerosol scattering. The atmospheric scenarios as in Fig. 7.3 were used. For tangent heights below 25 km at a solar zenith angle of 30° and below 30 km at a solar zenith angle of 80°, the CDI and the spherical solutions agree within 1% for most scenarios. For a solar zenith angle of 30°, starting from the tangent height about of 25 km, the relative difference increases almost linearly with the tangent height and reaches in the worst case 8% at a tangent height of 60 km. The inclination of the curve depends on the selected atmospheric scenario and the azimuth angle. For a solar zenith angle of 80°, the relative difference for azimuth angles of 0° and 180° does not exceed 2% for tangent heights up to 60 km. Both curves for an azimuth angle of 90° show similar behavior as for a solar zenith angle of 30°.

Figure 7.11 shows the relative difference as a function of solar zenith and azimuth angle at a tangent height of 30 km. The calculations were performed for the same set of solar zenith and azimuth angles and the same atmospheric scenario as in Fig. 7.7.

7.6 Model validation

7.6.1 Pre-validation

As a first step to validate the newly developed radiative transfer model, the pseudo-spherical diffuse radiation field calculated using the GOMETRAN radiative transfer model has been validated, which is used as an initial guess for the iterative scheme. In [*Rozanov et al.*, 1997] the diffuse radiances at the top of the atmosphere for the nadir viewing geometry calculated using GOMETRAN and DISORT [*Stamnes et al.*, 1988] were compared. The agreement between both models was found to be better than 0.5%. In [*Blindauer et al.*, 1996] the simulated pseudo-spherical radiance in the middle of the atmosphere was compared with balloon–born measurements. Simulated and measured radiances were found to be in good agreement within the experimental error. The UV indices, which characterize the radiation field at the bottom of the atmosphere, simulated using 6 different multiple scattering pseudo-spherical radiative transfer models were compared in [*Koepke et al.*, 1998]. The UV index calculated using GOMETRAN was found to be in good agreement with the indices calculated using other radiative transfer models. This shows that the pseudo-spherical radiance as calculated with GOMETRAN is adequately validated and is a sufficiently accurate initial guess for the iterative scheme.

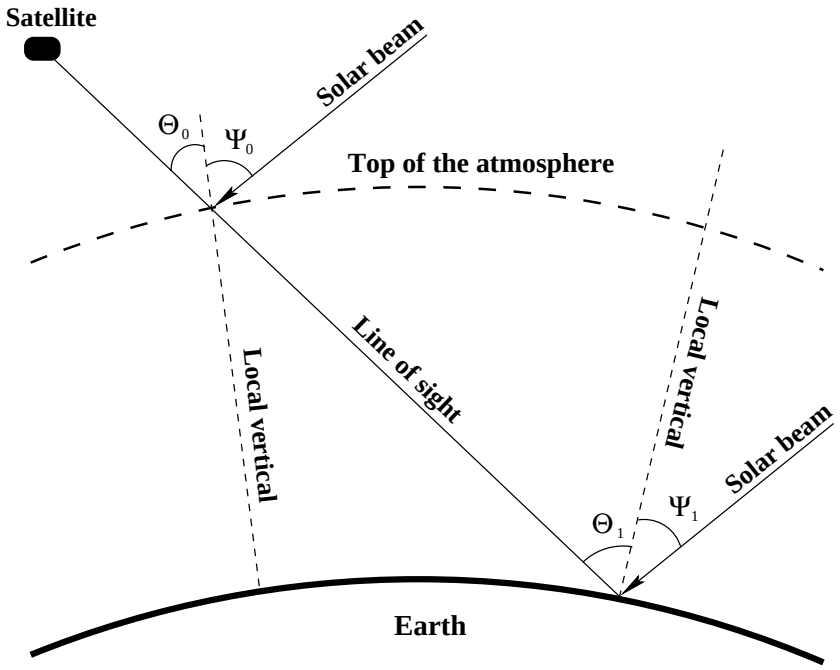

Figure 7.12: Definition of the solar zenith angle Ψ and the viewing angle Θ in different models.

7.6.2 Self consistence tests

As a self-consistence test for the considered radiative transfer model, the diffuse radiation for zenith and nadir viewing geometry was calculated performing no global iteration and compared to the corresponding radiation calculated with GOMETRAN. The intensities in this case are expected to coincide because the pseudo-spherical source function in Eq. (7.18) is used and the spherical operator L_s^{sp} for such geometries has to result in the same intensities as the pseudo-spherical one (i.e., L_s^{pp}). In fact, these intensities were found to be in agreement within better than 1%. As a test for the iterative scheme, the model was run using an Earth's radius increased by a factor of 1000. The corresponding results were compared with the pseudo-spherical model. Both models were found to agree to less than 2%. The remaining difference between these test–solutions appears to be caused by solving different types of equations, i.e., the integro-differential equation in GOMETRAN and the integral equation in CDIPI.

7.6.3 Off-nadir viewing geometry

To verify the CDI solution in non-limb viewing geometry, a series of comparisons to an independent fully spherical model were performed. Radiances at the top of the atmosphere calculated with the CDI approach and with the Gauss-Seidel spherical (GSS) radiative transfer model were compared. Since CDI is a scalar and GSS a vector radiative transfer model, direct comparison between both models can not be performed. In order to reduce

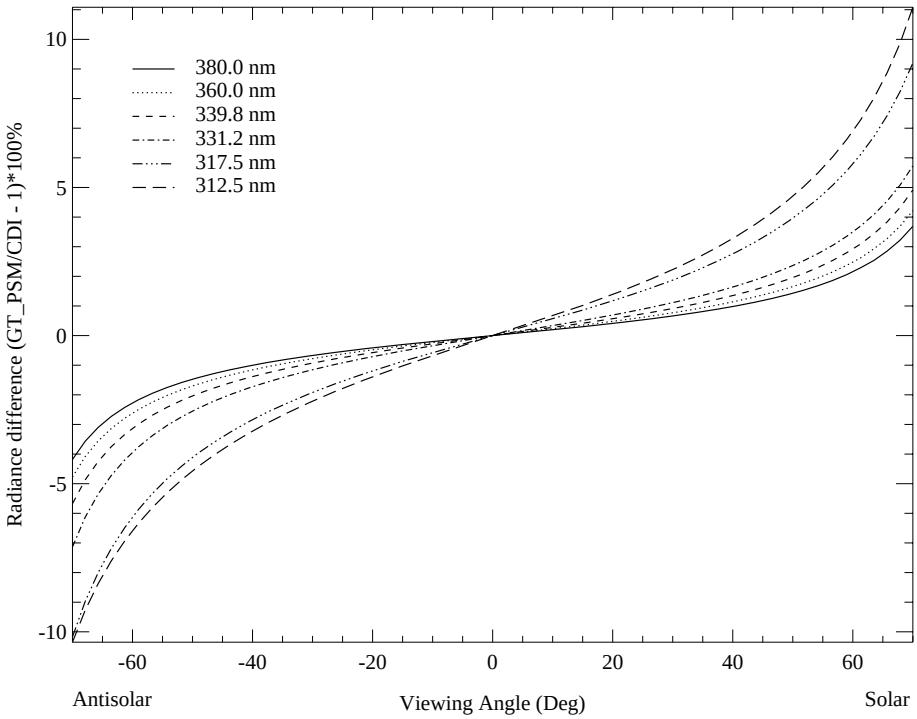

Figure 7.13: Relative differences between the radiances at TOA calculated with GT_PSM and with CDI for six wavelengths at a solar zenith angle of 85°.

the influence of polarization effects which are included in GSS and neglected in CDI, the corresponding ratios of the pseudo-spherical to the spherical solution were compared, namely, GT_PS/CDI and MPS/GSS. Here, MPS denotes the Mateer pseudo-spherical model (vector model) which was used to analyze the ratio MPS/GSS in [*Caudill et al.*, 1997] and GT_PSM is the GOMETRAN pseudo-spherical model (scalar model) with MPS-like input angle definition. Figure 7.12 shows the solar zenith angle and the viewing angle definitions used in different models. In the CDI and GSS radiative transfer models the solar zenith angle and the viewing angle at the top of the atmosphere (Ψ_0, Θ_0) are used as model input. Whereas in the MPS and GT_PSM models, the solar zenith angle and the viewing angle at the point where the line-of-sight intersects the Earth's surface (Ψ_1, Θ_1) are used as input parameters. The corresponding values of Ψ_1 and Θ_1 can be calculated from given Ψ_0 and Θ_0 using Eq. (7.10) and (7.9), respectively.

The solar zenith angle and the viewing angle in a pseudo-spherical model are assumed not to change along the line-of-sight. Therefore, a single effective value has to be chosen to describe the source function. Since the simulated radiation is more sensitive to scattering processes near the bottom of the atmosphere than to the scattering processes near the top of the atmosphere, it is more accurate to define the input angles for pseudo-spherical models as in MPS and GT_PSM. However, all angle variables below refer to the top of the atmosphere and were appropriately converted when being used as input angles for MPS and GT_PSM models.

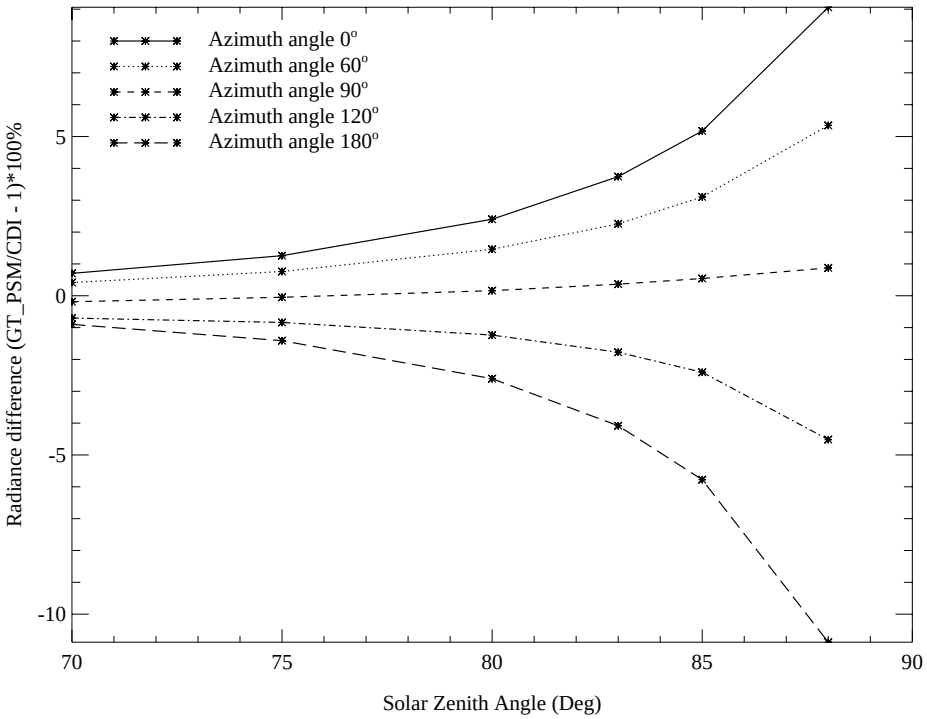

Figure 7.14: Relative differences between the radiances at TOA calculated with GT_PSM and with CDI at 317.5 nm for a viewing angle of 55° and five azimuth angles.

All calculations were carried out including ozone absorption and Rayleigh scattering. A surface albedo of 0.1 was selected. The comparison was performed at six wavelengths for a variety of viewing angles using the high-latitude 325 DU ozone profile and the same ozone cross sections as used in [*Caudill et al.*, 1997].

The relative differences between the radiances at TOA calculated with GT_PSM and with CDI for six wavelengths at a solar zenith angle of 85° are shown in Fig. 7.13. Positive values for the viewing angle correspond to the azimuth angle of 0° and negative values to the azimuth angle of 180°. The azimuth angle of 0° corresponds to the line-of-sight pointing towards the sun. The differences depict the influence of spherical effects on the calculated radiance. In Fig. 7.14 the relative difference between the GT_PSM and CDI models at 317.5 nm is shown as a function of solar zenith angle for a viewing angle of 55° and a set of azimuth angles. The dependence of the relative difference on solar zenith angle, viewing angle, azimuth angle, and wavelength is in good qualitative agreement with the results published in [*Caudill et al.*, 1997]. This agreement demonstrates that spherical effects in the CDI approach are taken into account correctly. Nevertheless, it is necessary to examine whether despite the neglect of spherical features of the multiple scattering source function in the CDI model sufficiently accurate solutions result. In order to estimate the quantitative difference between the CDI approach and the fully spherical GSS model, the relative differences (GT_PSM/CDI - 1)∗100% were compared with the relative differences (MPS/GSS - 1)∗100%. The comparison was performed for six wavelengths at a solar zenith

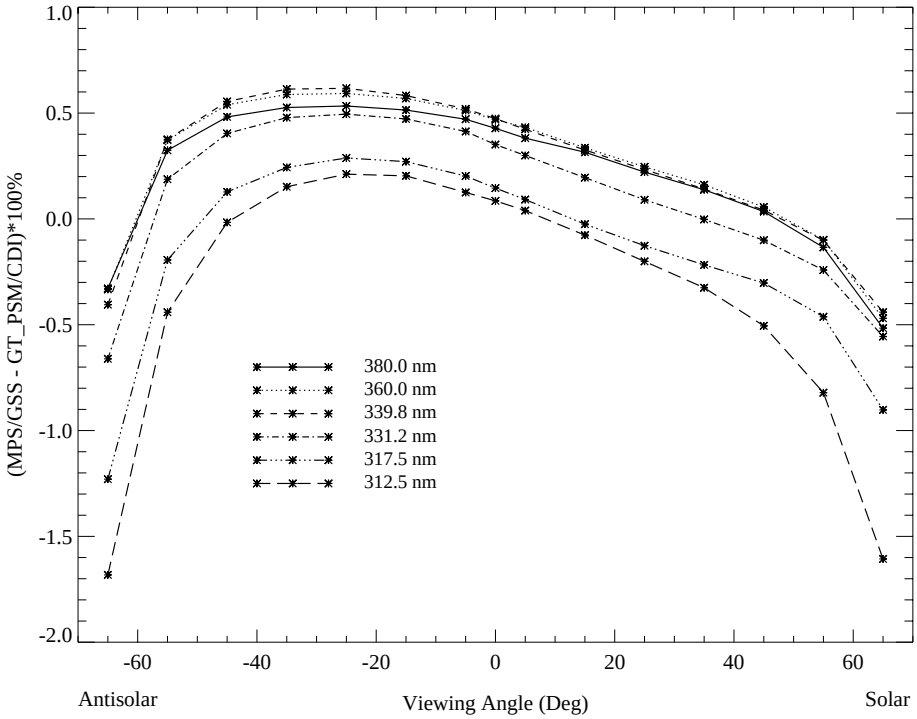

Figure 7.15: Differences between ratios GT_PSM/CDI and MPS/GSS for six wavelengths at a solar zenith angle of 85°.

angle of 85°. The results of the comparison are shown in Fig. 7.15. The differences do not exceed the values typical for the comparison of independent radiative transfer models (1–2%). The small increase of the differences at short wavelengths and large viewing angles appears to arise from the inclusion of the polarization effects in the MPS and GSS and their neglect in the CDI and GT_PSM models. This means that the CDI approach treats spherical features of the atmosphere accurately enough for the viewing geometries under consideration.

7.6.4 Limb viewing geometry

It is obvious that the largest effect of the sphericity of the Earth's atmosphere is to be expected in limb viewing geometry. Therefore, in order to verify the developed approach, a comparison with the Monte–Carlo radiative transfer model, Siro, [*Oikarinen et al.*, 1999] for limb viewing geometry was performed. The outgoing radiation at 500 nm at the top of the atmosphere was calculated using both radiative transfer models. The accuracy of the Siro model radiance is reported to be better than 1% (the Siro model radiance and accuracy estimations were provided by L. Oikarinen, Finnish Meteorological Institute, Helsinki, Finland). All calculations were carried out including Rayleigh scattering and ozone absorption. The same model atmosphere and surface albedo as discussed in Section 7.3 were used. As in the previous sections, all angles refer to the top of the atmosphere.

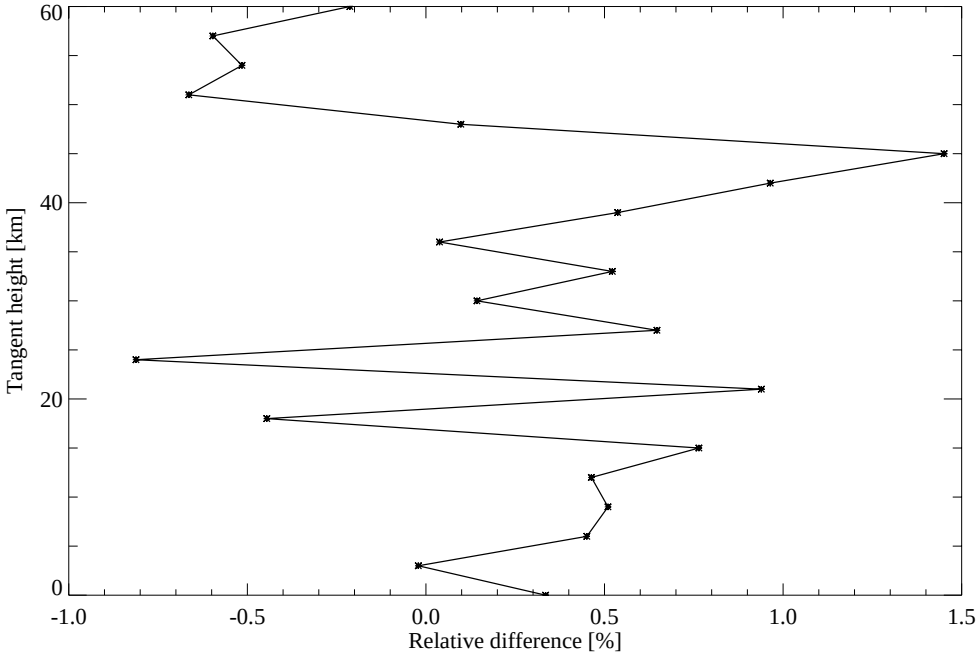

Figure 7.16: Relative difference between CDIPI and Siro, i.e., $(\text{CDIPI/Siro} - 1) * 100\%$, as a function of tangent height at a solar zenith angle of 30° and an azimuth angle of 90°.

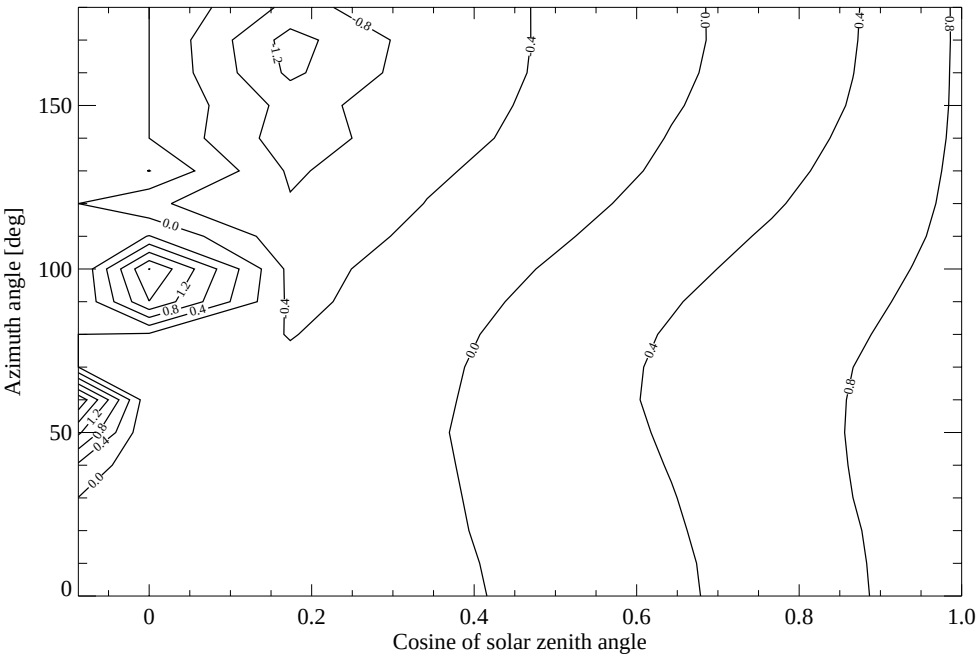

Figure 7.17: Relative difference between CDIPI and Siro, i.e., $(\text{CDIPI/Siro} - 1) * 100\%$, as a function of solar zenith angle and azimuth angle at 10 km tangent height.

Simulations using the CDIPI radiative transfer model were carried out performing one global iteration, i.e., $I_{dif}^{(2)}(r_t, \Psi, \Theta, \varphi)$ was used as the output intensity of the diffuse radiation, where r_t denotes the top of the atmosphere. The radiation field in CDIPI was calculated for solar zenith angles between 0° and 98° and set to zero for solar zenith angles larger than 98°. Therefore, the comparison was carried out only for line-of-sights with the solar zenith angle at the tangent point less than 98°. Thus, for line-of-sights starting at a solar zenith angle of 90° at the top of the atmosphere, the largest azimuth angle included in the comparison was 140°. For this line-of-sight, the solar zenith angle at the tangent point is 97.3°. For line-of-sights starting at a solar zenith angle of 95° at the top of the atmosphere, only azimuth angles between 0° and 60° were included in the comparison, because for larger azimuth angles most of the line-of-sight is in the shadow region and the error caused by neglect of radiance at solar zenith angles larger than 98° can be relevant.

The relative difference between CDIPI and Siro, i.e., (CDIPI/Siro − 1) ∗ 100%, as a function of tangent height at a solar zenith angle of 30° and an azimuth angle of 90° is shown in Fig. 7.16. As can be seen, the relative difference never exceeds 1.5% and is less than 1% for all tangent heights excluding 45 km. The same relative difference as a function of solar zenith angle and azimuth angle at a tangent height 10 km is shown in Fig. 7.17. For most points the difference does not exceed 1%. The two points with a maximum difference of 2.3%, at a solar zenith angle of 95° and an azimuth angle of 60°, and of 1.9%, at a solar zenith angle of 90° and an azimuth angle of 140°, are closest to the excluded region of solar zenith and azimuth angles. Thus, the results at these points can also be affected by neglect of radiance at solar zenith angles larger than 98°.

7.7 Computational efficiency

As mentioned in the introduction, one of the most important features, which has to be incorporated in a spherical radiative transfer model, is its computational efficiency. The required computer time obviously depends on the computer system architecture and its performance. The estimation of computer time (user time) needed to simulate the intensities for the comparison shown in Fig. 7.17 (a set of 209 user-defined variables was used: 11 solar zenith angles and 19 azimuth angles) was performed for three different computer systems. The calculations using CDIPI with 1127 spatial grid points (49 height grid layers and 23 solar zenith angles) and 100 integration nodes took approximately 10 min at a SUN Sparc Ultra 2, 6.5 min at a Silicon Graphics Origin 10000, 6 min for 1 CPU and about 1 min using 8 CPUs of a CRAY J90se. The same calculations made by Siro using a Silicon Graphics Origin 2000 took about 13 hours (L. Oikarinen, Finnish Meteorological Institute, Helsinki, Finland, private communications, 1999).

Chapter 8

Applications of the new spherical radiative transfer model

8.1 Differential approach involving the CDI model

Since the fully spherical CDIPI model is relatively slow, some approximation has to be found to perform forward simulations for the interpretation of large amount of multi-spectral measurements in limb viewing geometry. Using the approximative CDI approach instead of the fully spherical model, forward simulations can be performed much faster. Unfortunately, as discussed in Section 7.5, the Sun-normalized radiation calculated using the CDI model in limb viewing geometry is not accurate enough at tangent heights above 30 km.

One of the commonly used methods to reduce the influence of systematical errors in the measured spectra on retrieved parameters is using the differential approach; that is, the differential optical depth (DOD) instead of the radiation is used for the retrieval. This approach is also employed to avoid the influence of instrument calibration errors.

The differential optical depth is commonly defined by

$$\tau(\lambda) = \ln I(\lambda) - \sum_{k=0}^{N} a_k \lambda^k \,, \tag{8.1}$$

where $I(\lambda)$ is the Sun-normalized radiation, λ is the wavelength, a_k are polynomial coefficients and N is the polynomial order. It is the differential optical depth given by Eq. (8.1), which is used in the DOAS retrieval to estimate atmospheric trace gas vertical distributions or vertical column densities.

Accuracy of differential optical depth simulated with the CDI radiative transfer model for different scenarios is investigated below. Accuracy was estimated comparing the differential optical depths resulting from the approximative CDI approach and the fully spherical CDIPI model. Two spectral windows were selected for the comparison, namely, 310 – 340 nm and 425 – 455 nm, which can be used for the vertical profile retrieval of ozone and NO_2, respectively, from the SCIAMACHY limb measurements.

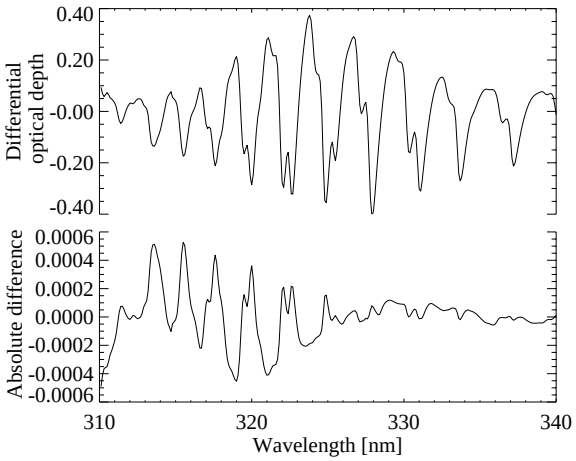

Figure 8.1: Differential optical depth and absolute difference between spherical and CDI differential optical depths.

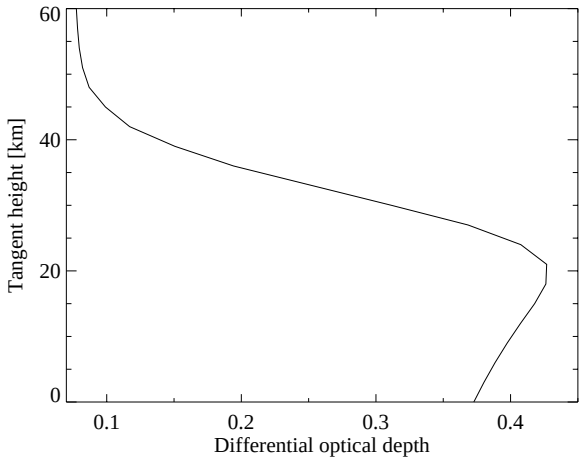

Figure 8.2: Typical dependence of the maximum DOD in the spectral region 310 – 340 nm on the tangent height.

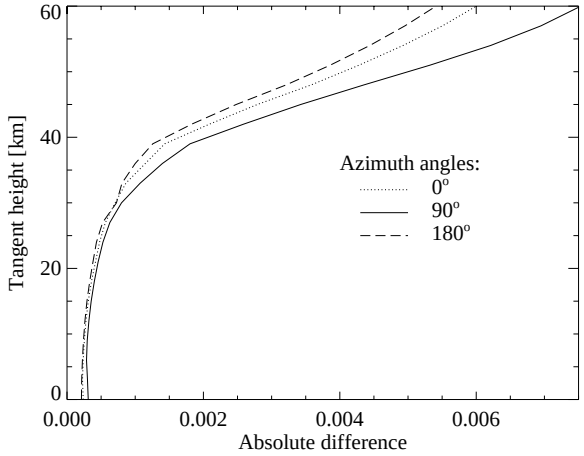

Figure 8.3: Maximum absolute difference between spherical and CDI DODs at a solar zenith angle of 30° for different azimuth angles.

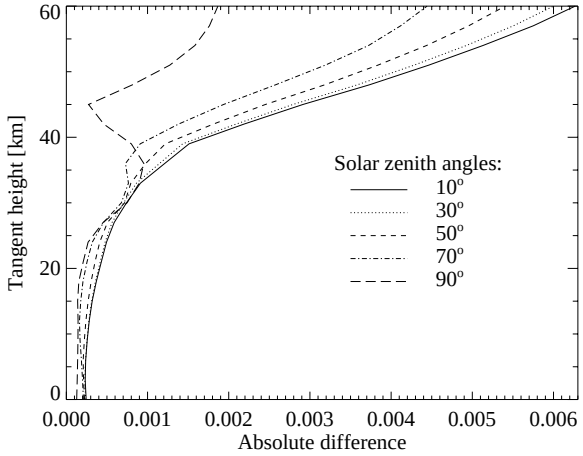

Figure 8.4: As Fig. 8.3, but at an azimuth angle of 0° for different solar zenith angles.

All calculations below were done including the absorption by ozone, NO_2 and O_4 as well as aerosol and Rayleigh scattering. A background aerosol scenario was selected. The computations were performed using a surface albedo of 0.3, except for Figs. 8.5 and 8.10. All angles are defined at the top of the atmosphere.

Figure 8.1 shows the differential optical depth and the absolute difference between spherical and CDI differential optical depths, i.e., $\tau(\lambda)^{sph} - \tau(\lambda)^{CDI}$, in the spectral region 310 – 340 nm at a tangent height of 24 km, a solar zenith angle of 30° and an azimuth angle of 90°. Typical dependence of the maximum differential optical depth (MDOD) in the

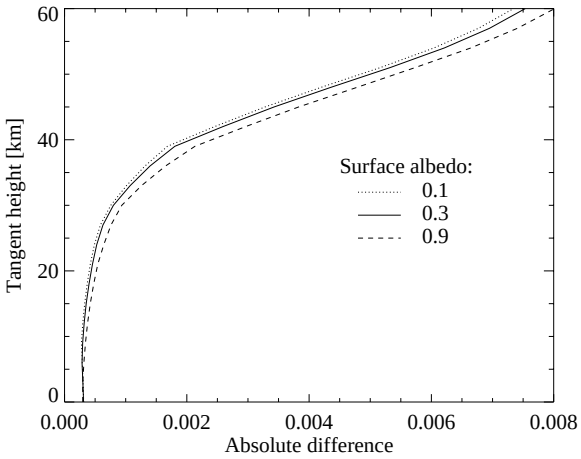

Figure 8.5: As Fig. 8.3, but at a solar zenith angle of 90° and an azimuth angle of 90° for different surface albedo.

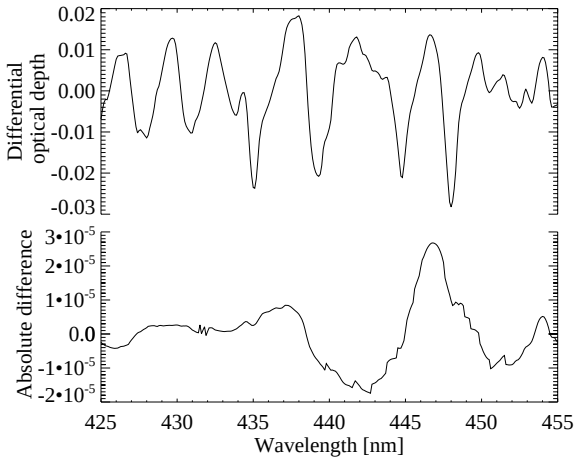

Figure 8.6: As Fig. 8.1, but in a spectral region used for NO_2 vertical profile retrieval.

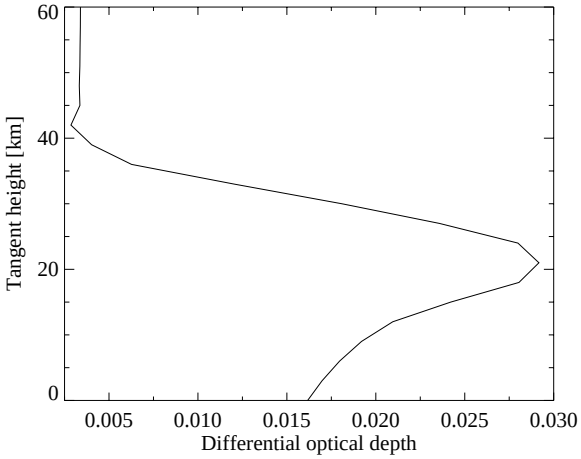

Figure 8.7: As Fig. 8.2, but in the spectral region 425 – 455 nm.

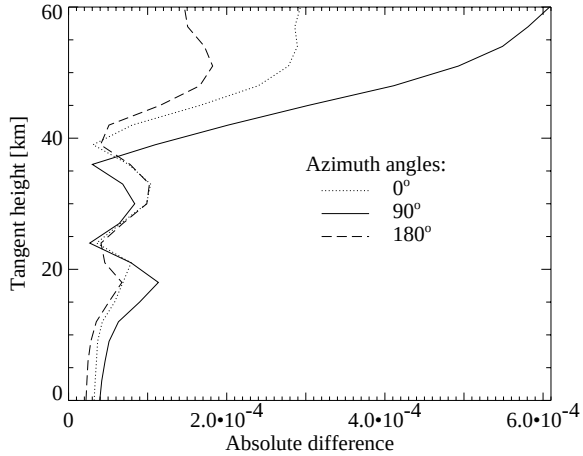

Figure 8.8: As Fig. 8.3, but in the spectral region 425 – 455 nm.

selected spectral region on the tangent height is shown in Fig. 8.2. Since MDOD is found to be only weakly dependent on the selected viewing geometry and surface albedo, only the values at solar zenith angle of 10° and azimuth angle of 0° are shown. Figures 8.3–8.5 show the maximum value in the selected spectral interval of the absolute difference between spherical and CDI differential optical depths as a function of tangent height for different solar zenith and azimuth angles as well as different surface albedo. For tangent heights below 40 km, the absolute difference never exceeds 0.002 and the relative difference is less than 1.5%. Typically, the difference increases with increasing surface albedo and, above 20 km, with the tangent height.

Similar to Fig. 8.1, Fig. 8.6 shows the differential optical depth and the absolute dif-

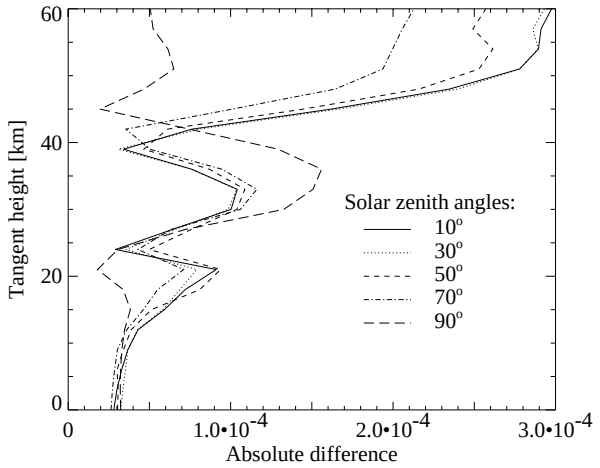

Figure 8.9: As Fig. 8.4, but in the spectral region 425 – 455 nm.

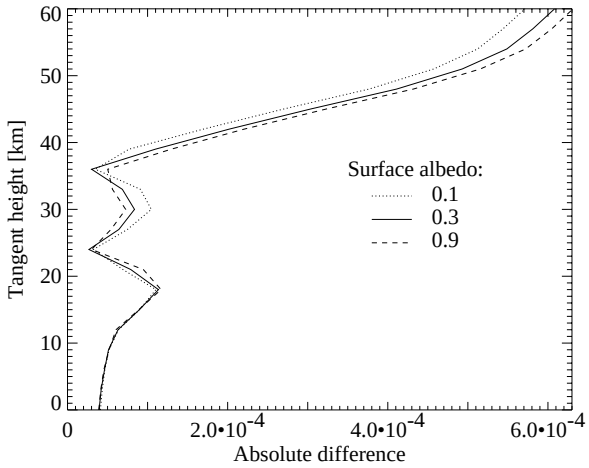

Figure 8.10: As Fig. 8.5, but in the spectral region 425 – 455 nm.

ference between spherical and CDI differential optical depths in the spectral region 425 – 455 nm. Figure 8.7, similar to Fig. 8.2, shows a typical dependence of the maximum differential optical depth in this spectral region on the tangent height. Figures 8.8–8.10 show the same dependencies as Fig. 8.3–8.5, but for the spectral region 425 – 455 nm. The absolute difference is typically less then $2 \cdot 10^{-4}$ and never exceeds $7 \cdot 10^{-4}$, whereas the noise level in DOD spectra derived from the measurements is unlikely to be less then 10^{-3}.

Thus, using the differential approach, an acceptable accuracy of ozone and NO_2 vertical profile retrieval can be achieved performing forward calculations with the CDI model, which is substantially faster than a spherical model.

8.2 Air mass factors for off-axis measurements

DOAS interpretation of ground-based zenith-sky measurements is one of the commonly used methods to obtain information about vertical distribution or total column abundance of such atmospheric constituents as ozone, NO_2, BrO, etc. Air mass factors needed for DOAS retrieval are well studied for zenith-viewing geometry, see, for example [*Solomon et al.*, 1987; *Perliski and Solomon*, 1993]. They are found to be weakly dependent on atmospheric parameters and can be calculated using a single scattering radiative transfer model, as long as the abundance of the species in question is small in the troposphere, [*Mount et al.*, 1987] or with a pseudo-spherical radiative transfer model [*Ridley et al.*, 1984]. To obtain additional information about atmospheric trace gas abundances in the troposphere, so-called "off-axis" measurements are carried out, i.e., ground-based measurements at line-of-sight angles about several degrees above the horizon. In this Section, the sensitivity of the air mass factors for off-axis geometry to atmospheric parameters is investigated. The suitability of pseudo-spherical models for the interpretation of the off-axis measurements is discussed as well.

Table 8.1: Solar zenith (SZA) and relative azimuth (RAA) angles for the selected off-axis measurement sequence.

sunset SZA/RAA	65.4°/131.3°	65.8°/123.1°	66.4°/115.1°	67.2°/107.1°	68.2°/99.2°
	69.2°/91.3°	70.5°/83.5°	71.8°/75.8°	73.2°/68.2°	74.6°/60.7°
	76.0°/53.2°	77.5°/45.7°	78.9°/38.3°	80.3°/30.9°	81.6°/23.5°
	82.7°/16.6°	86.6°/18.1°	87.0°/25.6°	87.1°/31.9°	
sunrise SZA/RAA	87.5°/36.0°	87.4°/43.5°	87.1°/50.9°	86.6°/58.5°	85.9°/65.9°
	85.1°/73.4°	84.1°/80.9°	83.0°/88.3°	81.8°/96.0°	80.4°/03.2°
	79.1°/10.6°	77.6°/18.0°	76.2°/25.4°	74.7°/32.8°	73.5°/39.2°
	66.4°/71.8°	65.8°/63.7°	65.4°/55.6°		

8.2.1 Measurement technique

The air mass factors discussed below were calculated to interprete the zenith-sky (line-of-sight angle 0°) and off-axis (line-of-sight angle 86°) measurements performed in Ny-Ålesund, Spitsbergen (79°N, 12°E) during a selected day in spring 1999. The measurements were carried out in the spectral range from 330 nm to 490 nm at solar zenith angles from 65° to 87° using a Czerny-Turner spectrograph. Details on the instrument and observation modes can be found in [*Wittrock et al.*, 1999]. Performing the off-axis measurements, the azimuth angle of the instrument line-of-sight was fixed relative to North pole and the relative azimuth between the line-of-sight and the direct solar beam, hence, was changing during the measurements. The corresponding values for solar zenith (SZA) and relative azimuth (RAA) angles for the selected off-axis measurement sequence are presented in Table 8.1.

8.2.2 Air mass factors

The air mass factors are calculated using the intensity of the radiation simulated with a radiative transfer model in an appropriate viewing geometry as follows [*Solomon et al.*, 1987]:

$$A = \frac{\ln(I_-/I_+)}{\tau}\,, \tag{8.2}$$

where τ is the vertical optical depth of the targeted trace gas. I_+ and I_- are the intensities with and without absorption by the trace gas under consideration, respectively.

In order to investigate the applicability of pseudo-spherical radiative transfer models for off-axis viewing geometry, intensities I_+ and I_- were calculated using the SCIATRAN pseudo-spherical radiative transfer model [*Rozanov et al.*, 2000b] and the CDIPI spherical radiative transfer model discussed in Chapter 7. The simulated slant columns were obtained

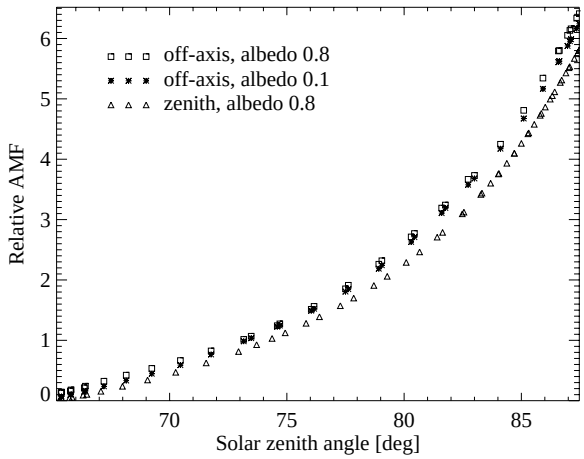

Figure 8.11: Relative air mass factors for ozone at 337.2 nm for off-axis and zenith viewing geometry.

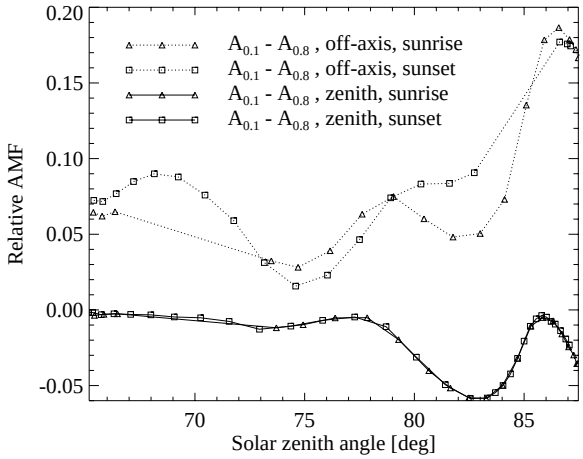

Figure 8.12: Absolute difference between ozone air mass factors at 337.2 nm for surface albedo of 0.1 and 0.8.

applying the same DOAS retrieval algorithm to the synthetic spectra as used to interprete experimental data. In order to estimate the variability of air mass factors with atmospheric parameters, a set of air mass factors for ozone, NO_2, and O_4 was calculated using various aerosol scenarios, surface albedo (ozone only) and model atmospheres (NO_2 only).

The DOAS fit is commonly applied to relative spectra, i.e., twilight spectra are usually divided by a reference spectrum. A spectrum measured at noon is commonly used as a reference. Therefore, the relative air mass factors are of interest rather than absolute ones. As clearly seen from Eq. 8.2, the relative air mass factor is given by

$$A_{rel} = A_{abs} - A_{ref} \; . \tag{8.3}$$

The relative air mass factors for ozone at 337.2 nm for zenith and off-axis viewing geometry calculated with the CDIPI model are shown in Fig. 8.11. All air mass factors discussed below are supposed to be the relative air mass factors according to Eq. 8.3. As a reference spectrum in both zenith and off-axis viewing geometries a zenith-sky spectrum at the smallest solar zenith angle is used.

Figure 8.12 and 8.13 show the absolute differences between ozone air mass factors calculated for two different surface albedo and aerosol scenarios, respectively. The absolute differences between ozone air mass factors calculated with the SCIATRAN pseudo-spherical and CDIPI spherical radiative transfer models are shown in Fig 8.14. Although the dependence of ozone air mass factors on atmospheric parameters is much stronger for off-axis than for zenith viewing geometry, the relative difference in all cases does not exceed 3% for air mass factors larger than 2.

Figure 8.15 shows NO_2 air mass factors calculated with the CDIPI model for two different atmospheric models, namely, for the US Standard (USS) model atmosphere containing only a small amount of NO_2 in the troposphere and for the MPI model atmosphere yielding an additional peak of NO_2 vertical profile in the troposphere. As clearly seen, air mass

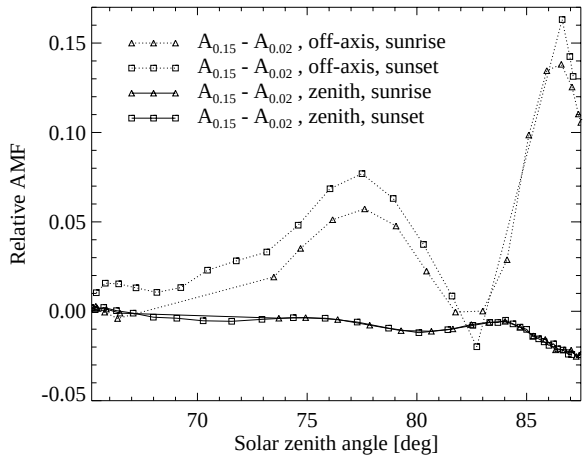

Figure 8.13: Absolute difference between ozone air mass factors at 337.2 nm calculated for aerosol optical depth of 0.15 and 0.02.

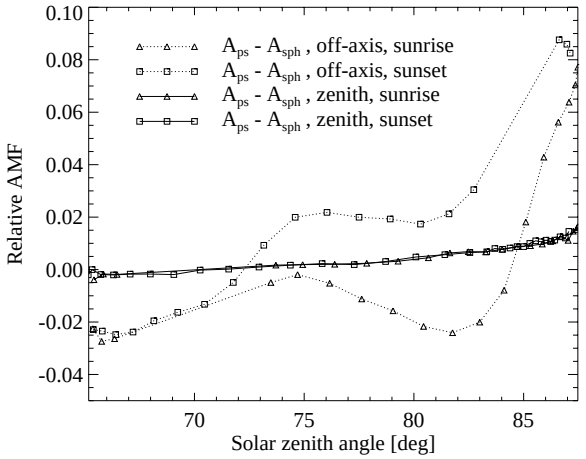

Figure 8.14: Absolute difference between ozone air mass factors at 337.2 nm calculated using pseudo-spherical and spherical radiative transfer models.

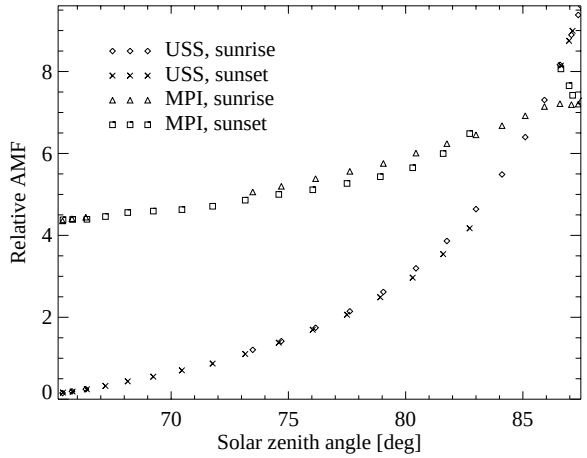

Figure 8.15: Relative air mass factors for NO_2 at 435 nm for off-axis viewing geometry calculated using the US Standard and MPI model atmospheres.

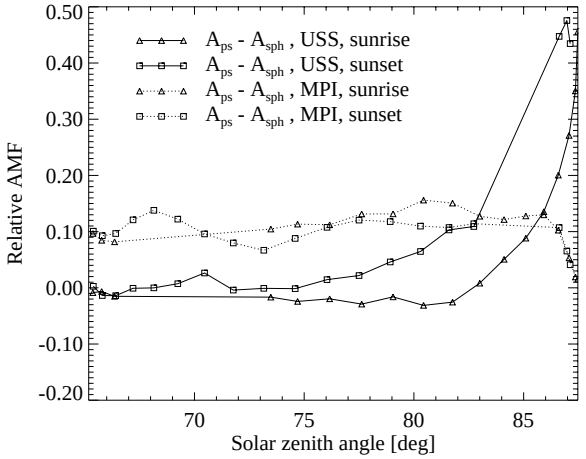

Figure 8.16: Absolute difference between NO_2 air mass factors at 435 nm calculated using pseudo-spherical and spherical radiative transfer models.

factors calculated using different model atmospheres show quite different dependencies on the solar zenith angle. Thus, an additional study of NO_2 vertical profile structure has to be carried out before the air mass factor computations. Figure 8.16 shows absolute differences of NO_2 air mass factors calculated using the SCIATRAN pseudo-spherical and CDIPI spherical radiative transfer models. The relative difference between the pseudo-spherical and spherical air mass factors for the US Standard model atmosphere has its maximum value of about 7% at higher solar zenith angles, whereas for the MPI atmosphere the relative difference is about 2% almost independent of the solar zenith angle. This means

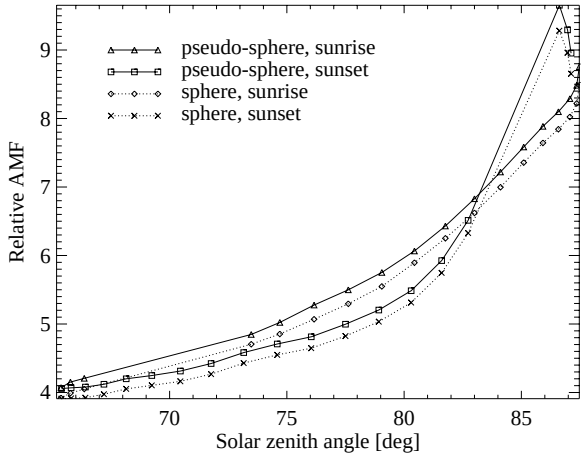

Figure 8.17: O_4 air mass factors at 477.1 nm for off-axis viewing geometry calculated using pseudo-spherical and spherical radiative transfer models.

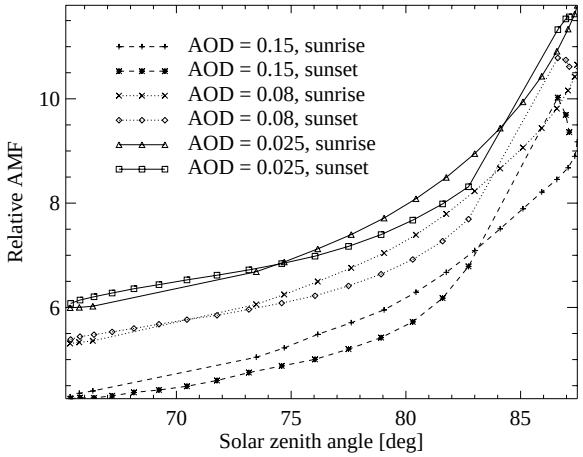

Figure 8.18: O_4 air mass factors at 477.1 nm for off-axis viewing geometry calculated for aerosol optical depth of 0.15, 0.08, and 0.025.

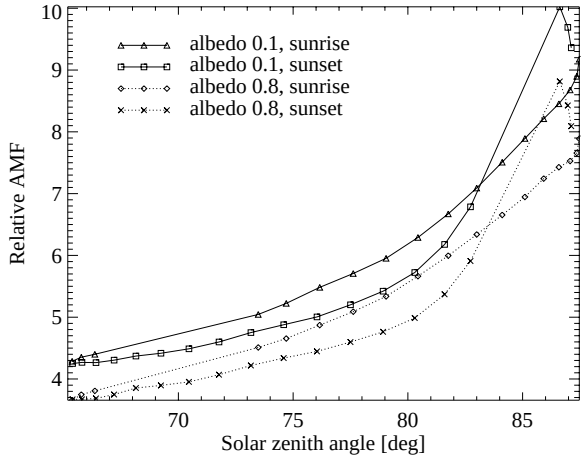

Figure 8.19: O_4 air mass factors at 477.1 nm for off-axis viewing geometry calculated for surface albedo of 0.1 and 0.8.

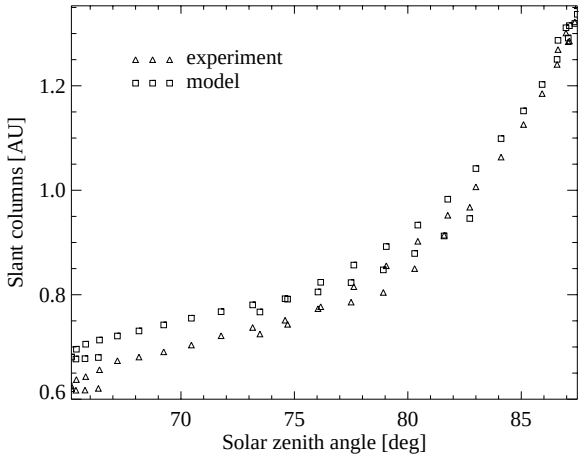

Figure 8.20: Comparison between slant columns retrieved from experimental data and simulated spectra.

that a spherical radiative transfer model needs to be used to retrieve NO_2 vertical columns accurately enough.

The relative air mass factors of O_4 calculated with SCIATRAN pseudo-spherical and CDIPI spherical radiative transfer models are shown in Fig 8.17. The pseudo-spherical and spherical air mass factors differ by 3–5% in the relevant range of the solar zenith angles. Figure 8.18 and 8.19 show O_4 air mass factors calculated for three different aerosol scenarios and two surface albedo, respectively. As clearly seen, the air mass factors are strongly sensitive to the selected atmospheric parameters.

A comparison of simulated O_4 slant columns with experimental data is presented in

Fig. 8.20 . As clearly seen, the measured dependence of O_4 slant column on azimuth and solar zenith angle is reproduced by the radiative transfer model. The better agreement between experimental and model curves can be achieved using an appropriate fit procedure. Since the vertical column of O_4 can be calculated if vertical profiles for pressure and temperature are known, such a comparison can be used in controlling if the selected atmospheric model can reproduce real atmospheric processes accurately enough.

8.3 Interpretation of zenith-sky measurements considering NO_2 photochemistry

As mentioned in Section 8.2, the radiative transfer models commonly used to calculate air mass factors for zenith-sky measurements consider either multiple scattered radiation in a plane-parallel atmosphere assuming a constant vertical distribution of atmospheric trace gases (pseudo-spherical models) or take into account only single scattered radiation (single scattering models). Although such simplified models are sufficient for most situations, they can not be used to interpret zenith-sky measurements for the species in great abundance in the troposphere whose vertical distribution in the stratosphere varies with the solar zenith angle. To investigate the accuracy of different approaches, NO_2 was selected as a target atmospheric constituent. The corresponding measurements were carried out in Ny-Ålesund, Spitsbergen (79°N,12°E) in spring 1997 in the spectral range 435 – 480 nm [*Wittrock et al.*, 1999].

8.3.1 Slant column simulations

The slant columns of NO_2 as functions of solar zenith angle were simulated using three different radiative transfer models:
(a) the GOMETRAN pseudo-spherical radiative transfer model,
(b) the CDIPI spherical radiative transfer model, and
(c) a single scattering (SS) radiative transfer model which was derived from the CDIPI model by switching off the multiple scattering calculations.

Using each radiative transfer model, the intensities of the zenith-sky radiation with and without NO_2 absorption ($I_+(\Psi)$ and $I_-(\Psi)$, respectively) were simulated as functions of solar zenith angle. Then the slant columns were calculated as follows:

$$S(\Psi) = \frac{1}{\sigma} \ln \left[\frac{I_-(\Psi)}{I_+(\Psi)} \right] , \tag{8.4}$$

where σ is NO_2 cross section at the selected wavelength. The dependence of I_+ on the solar zenith angle, Ψ, in GOMETRAN is caused only by radiative transfer geometry, whereas this dependence in the CDIPI and the single scattering models is also due to the change of NO_2 vertical distribution with the solar zenith angle.

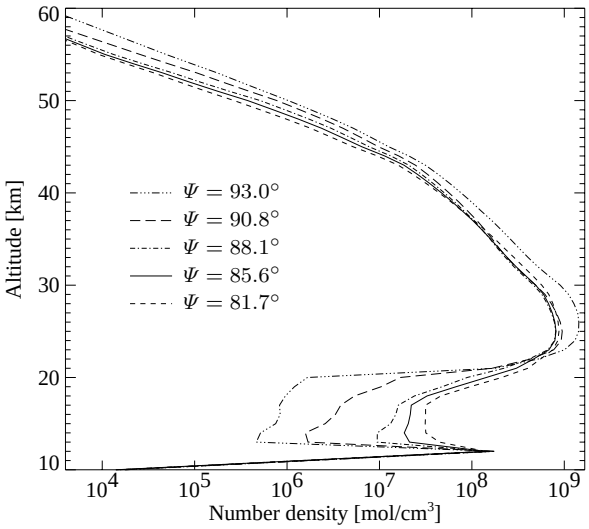

Figure 8.21: NO_2 vertical profiles for different solar zenith angles simulated with BRAPHO (Ny-Ålesund, sunrise, spring 1997).

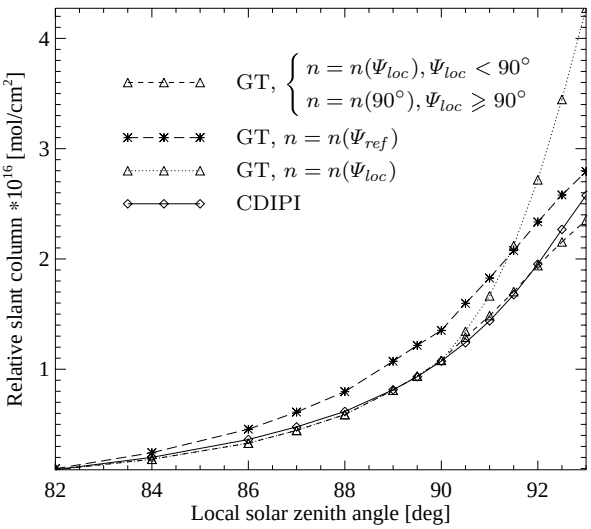

Figure 8.22: NO_2 slant columns calculated using the CDIPI spherical and the GOME-TRAN pseudo-spherical radiative transfer models.

From measured spectra, the slant columns were derived employing the DOAS fit:

$$\ln\left[\frac{I(\lambda,\Psi)}{I(\lambda,\Psi_{ref})}\right] \xrightarrow{\text{DOAS fit}} S_{exp}(\Psi)\ , \tag{8.5}$$

where subscript ref denotes the reference spectrum and λ is the wavelength. Similar to the measured values, the relative slant columns were simulated, which are defined by

$$\hat{S}(\Psi) = S(\Psi) - S(\Psi_{ref})\ , \tag{8.6}$$

where Ψ_{ref} is the solar zenith angle corresponding to the reference spectrum used in DOAS fit.

8.3.2 Slant column comparison

All calculations discussed below were performed for spring 1997 for Ny-Ålesund using a surface albedo of 0.8.

Figure 8.21 shows typical NO_2 vertical profiles, $n(\Psi)$, for different solar zenith angles calculated using the BRAPHO atmospheric photochemical model [*Sinnhuber et al.*, 1999] for sunrise conditions. The simulated vertical distribution of NO_2 shows a strong dependence on the local solar zenith angle in the altitude range 12 – 40 km. Since the BRAPHO model can only simulate the vertical distribution in the stratosphere, the dependence of the tropospheric NO_2 on the solar zenith angle could not be taken into account.

Figure 8.22 shows NO_2 slant columns calculated according to Eq. (8.4) as function of the local solar zenith angle, i.e., the solar zenith angle at instrument position. The slant

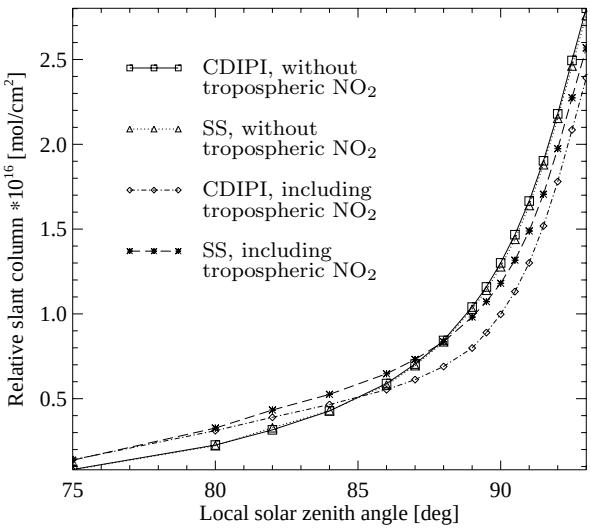

Figure 8.23: Simulated NO_2 slant columns for pure stratospheric and for stratospheric-tropospheric NO_2.

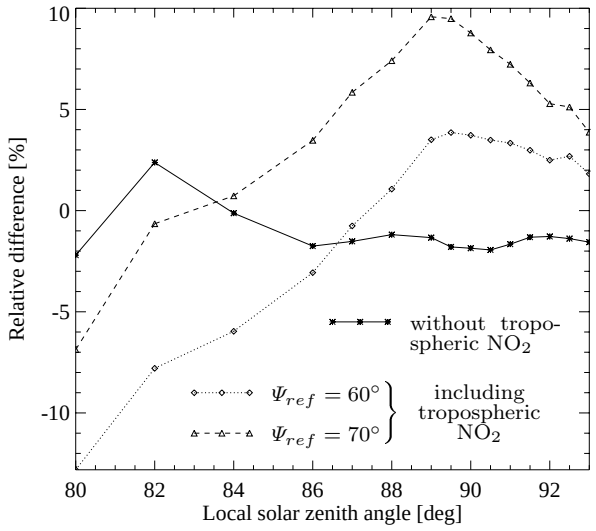

Figure 8.24: Relative difference between NO_2 slant columns calculated using the CDIPI and the SS models.

columns were calculated as follows:
(a) with the CDIPI spherical model (the results of this simulation were treated as "true" values),
(b) with the GOMETRAN pseudo-spherical model assuming the NO_2 vertical distribution to be independent of the solar zenith angle, i.e., $n = n(\Psi_{ref})$,
(c) similar to (b), but running the GOMETRAN model separately for each solar zenith angle using an appropriate (local) NO_2 vertical distribution, i.e., $n = n(\Psi_{loc})$, and
(d) similar to (c), but using the NO_2 vertical distribution at 90° for local solar zenith angles larger than 90°.

Thus, neglecting the dependence of NO_2 vertical distribution on the solar zenith angle leads to an overestimation of NO_2 slant column by 10 to 25 %. Better accuracy can be achieved with a pseudo-spherical radiative transfer model calculating the slant columns using vertical distribution at local solar zenith angle, i.e., at the instrument position. However, as seen from Fig. 8.22, this approach is inappropriate for solar zenith angles large than 91°. For these solar zenith angles a vertical distribution at 90° should be used instead of local vertical distribution. Using this approach, NO_2 slant columns can be calculated with an accuracy better than 5% for solar zenith angles up to 92.5° employing a pseudo-spherical model.

Figure 8.23 shows NO_2 slant columns calculated using the CDIPI and the single scattering models for pure stratospheric NO_2 and including tropospheric NO_2. The tropospheric part of NO_2 vertical profile was selected according to the MPI atmospheric model [*Brühl and Crutzen*, 1993] for an appropriate season and latitude (March, 75°N) and supposed to be independent of the local solar zenith angle. The relative differences between the slant columns calculated using the CDIPI and the single scattering models, i.e., (SS/CDIPI -

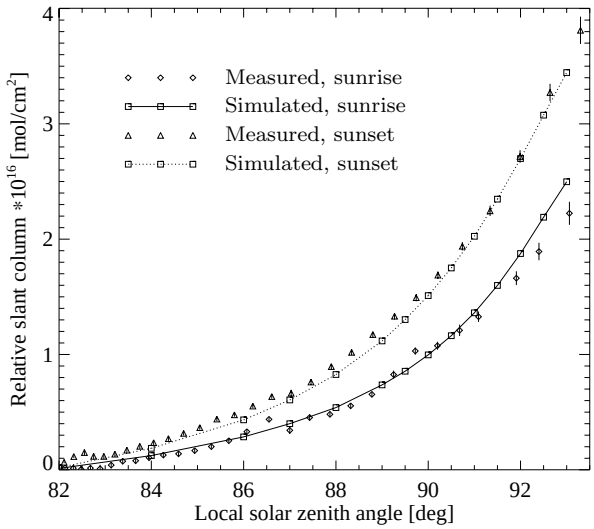

Figure 8.25: Measured and simulated (CDIPI) NO_2 slant columns at sunrise and sunset.

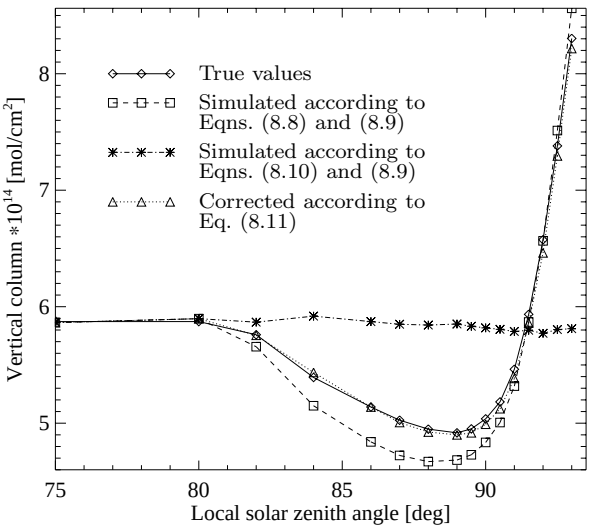

Figure 8.26: True NO_2 local vertical columns and vertical columns derived from the simulated spectra.

1)*100%, are shown in Fig. 8.24. If tropospheric NO_2 is included, the slant columns differ even at small solar zenith angles. Thus, accuracy of the slant columns calculated using a single scattering model is strongly dependent on the selected reference spectrum, whereas the differences between slant columns for pure stratospheric NO_2 are independent thereof.

Figure 8.25 shows measured and simulated (CDIPI) NO_2 slant columns at sunrise and sunset. The measured and simulated slant columns are in good agreement for all solar zenith angles at sunset and for solar zenith angles up to 91.5° at sunrise. Differences between measured and simulated slant columns for solar zenith angles larger than 91.5° at sunrise are believed to be caused by the BRAPHO model.

8.3.3 Vertical columns

A commonly used approach to obtain vertical columns of atmospheric trace gases is given by

$$S_{exp}(\Psi) = A(\Psi)\,V(\Psi) - A(\Psi_{ref})\,V(\Psi_{ref}) \approx [A(\Psi) - A(\Psi_{ref})]\,\hat{V}(\Psi)\;, \tag{8.7}$$

where $A(\Psi)$ and $V(\Psi)$ are the air mass factor and the vertical column at solar zenith angle Ψ, respectively, and $\hat{V}(\Psi)$ is some effective vertical column. For a stationary vertical distribution, $\hat{V}(\Psi) = V(\Psi) = V(\Psi_{ref})$ and the second equality in Eq. (8.7) is exact.

The air mass factors are calculated as follows:

$$A(\Psi) = \frac{1}{\tau(\Psi)}\,\ln\left[\frac{I_-(\Psi)}{I_+(\Psi)}\right]\;, \tag{8.8}$$

where $\tau(\Psi)$ is the local vertical optical depth of NO_2 at solar zenith angle Ψ. All quantities on the right hand side of Eq. (8.8) have to be calculated using an appropriate radiative

transfer model. Thus, the effective vertical column is calculated as follows:

$$\hat{V}(\Psi) = \frac{S_{exp}(\Psi)}{A(\Psi) - A(\Psi_{ref})} \; . \tag{8.9}$$

Figure 8.26 shows true vertical columns and vertical columns obtained applying different approaches to calculate air mass factors. A commonly used approach is to calculate air mass factors according to Eq. (8.8) and then vertical columns as given by Eq. (8.9). In this case, resulting vertical columns have similar dependence on the solar zenith angle as the true local vertical columns but differ by up to 15% from true values (dashed line with squares in Fig. 8.26). Another way is to use the following formula for the air mass factor

$$\tilde{A}(\Psi) = \frac{1}{\tau(\Psi_{ref})} \ln\left[\frac{I_-(\Psi)}{I_+(\Psi)}\right] \tag{8.10}$$

instead of Eq. (8.8). This means that the noon vertical optical depth instead of the local one is used at all solar zenith angles. This approach leads to an almost constant vertical column (dash-dotted line with asterisks in Fig. 8.26) which is approximately equal to the vertical column at noon (i.e., $V(\Psi_{ref})$ in Eq. (8.7)). Thus, the vertical column calculated according to Eqns. (8.8) and (8.9), $\hat{V}(\Psi)$, can be corrected requiring the exact equality in Eq. (8.7) and assuming $V(\Psi_{ref}) \approx \tilde{V}(\Psi)$, i.e.,

$$V(\Psi) = \frac{A(\Psi) - A(\Psi_{ref})}{A(\Psi)} \hat{V}(\Psi) + \frac{A(\Psi_{ref})}{A(\Psi)} \tilde{V}(\Psi) \; , \tag{8.11}$$

where $\tilde{V}(\Psi)$ is calculated using Eq. (8.9) with $\tilde{A}(\Psi)$ instead of $A(\Psi)$. As shown in Fig. 8.26 (dotted line with triangles) using this approach the local vertical distribution can be retrieved with an accuracy of 1-2%.

Conclusions

Solar occultation measurements

A radiative transfer model intended to simulate SCIAMACHY occultation measurements has been developed. The model can be used to simulate solar radiation transmitted through a spherical shell atmosphere. Absorption by all atmospheric trace gases having their absorption features in the spectral region covered by SCIAMACHY (240 - 2380 nm) can be taken into account. The absorption by all atmospheric trace gases in near IR spectral region as well as absorption by H_2O and O_2 in visible spectral region is treated employing "line-by-line" calculations.

The selected approach allows the weighting functions to be derived analytically. Typical dependences of the weighting functions for stratospheric and tropospheric absorbers on wavelength and tangent height are analyzed.

The forward model has been coupled with an retrieval algorithm, which involves either the optimal estimation method or the information operator approach. The occultation measurements performed at various tangent heights in various spectral windows can be interpreted together to prevent loss of the information.

The theoretical precisions of vertical profile retrieval of several atmospheric trace gases were investigated. They were found to be strongly dependent on the selected trace gas abundance, on the strength of its absorption features in the selected spectral region, and on the signal to noise ratio in the measured spectra.

The developed software package enables the retrieval of high-precision ozone vertical profiles in the upper troposphere and the stratosphere, as well as vertical profiles of some other stratospheric species, such as NO_2, BrO, ClO, and OClO, from SCIAMACHY occultation measurements. Due to the high sensitivity of retrieval to the vertical distribution of the atmospheric trace gases in the upper troposphere and the lower stratosphere, additional information on the transport of the tropospheric greenhouse gases (CH_4, H_2O, CO, etc.) to the stratosphere will be obtained from the measurements.

Modeling of the scattered solar radiation

Most important methods to perform radiative transfer calculations were reviewed. Their suitability and their disadvantages for a spherical planetary atmosphere were discussed. Most available radiative transfer models were found to be unsuitable to perform radiative

transfer calculations in a spherical planetary atmosphere. No existing radiative transfer model was found to be computationally efficient and free of disadvantages.

A novel radiative transfer model (CDIPI), suitable to calculate the radiation field in a spherical planetary atmosphere, has been developed. The new approach involves the Picard iterative approximation to solve the radiative transfer equation in its integral form. A radiation field calculated by solving the integro-differential radiative transfer equation in a pseudo-spherical atmosphere is used as an initial guess for the iterative scheme.

The convergence rate of the CDIPI solution was analyzed. Performing only one global iteration was found sufficient to determine the radiation field with an accuracy exact enough for most applications.

The newly developed radiative transfer model was compared with a Monte–Carlo model (Siro) and found to perform radiative transfer calculations accurately enough for viewing geometries which are relevant for the exploration of the Earth's atmosphere by means of satellite and ground-based instruments. The relative difference between the radiance at the top of the atmosphere calculated by CDIPI and Siro is typically less than 1%.

An approximate model (CDI) has been derived from the fully spherical CDIPI model allowing the computation time to be reduced by up to 100 times. The CDI radiative transfer model was compared with a Gauss-Seidel spherical radiative transfer model in an off-nadir viewing geometry. Both models were found to agree within 2%. A suitability of a pseudo-spherical model for the simulation of off-nadir measurements was investigated. The pseudo-spherical model was found to differ from the CDI model up to 10% at large solar zenith and viewing angles.

The accuracy of the CDI approach for limb viewing geometry was estimated and found to be better than 2% for tangent heights up to 30 km for all viewing geometries and atmospheric scenarios considered in this study. The deviation from the spherical solution increases with the tangent height depending on viewing geometry and atmospheric scenario and may be as large as 8% at a tangent height of 60 km. The CDI radiative transfer model can also be used as a forward model in the retrieval algorithm which uses the differential approach to obtain vertical profiles of ozone and NO_2.

The newly developed radiative transfer model was applied to calculate air mass factors for off-axis and zenith-sky measurements. Several scenarios were discussed when a fully spherical radiative transfer model is required to interprete ground-based measurements accurately enough.

Appendix

Appendix A

Coordinate transformations

Let

$$\{\mathbf{f}\} = \{\mathbf{f}_1, \mathbf{f}_2, \mathbf{f}_3\} \tag{A.1}$$

be a basis in a three-dimensional Euclidean space, and let

$$\{\tilde{\mathbf{f}}\} = \{\tilde{\mathbf{f}}_1, \tilde{\mathbf{f}}_2, \tilde{\mathbf{f}}_3\} \tag{A.2}$$

be another basis in the same space. The vectors of the coordinate system $\{\tilde{\mathbf{f}}\}$ are uniquely determined by their expansions in terms of the vectors of the original basis:

$$\tilde{\mathbf{f}}_i = \sum_{j=1}^{3} p_{ij}\, \mathbf{f}_j \ . \tag{A.3}$$

The coefficients p_{ij} are elements of matrix $\mathbf{P}$ called the matrix of the transformation from basis $\{\mathbf{f}\}$ to basis $\{\tilde{\mathbf{f}}\}$. Analogously, the transformation from basis $\{\tilde{\mathbf{f}}\}$ to basis $\{\mathbf{f}\}$ is given by

$$\mathbf{f}_i = \sum_{j=1}^{3} q_{ij}\, \tilde{\mathbf{f}}_j \ , \tag{A.4}$$

where matrix $\mathbf{Q}$ is the inverse of the matrix $\mathbf{P}$.

In order to find the transformation of the components of an arbitrary vector, $\mathbf{e}$, due to the basis transformation, the following relation can be used:

$$\mathbf{e} = \sum_{i=1}^{3} \xi_i\, \mathbf{f}_i = \sum_{i=1}^{3} \tilde{\xi}_i\, \tilde{\mathbf{f}}_i \ , \tag{A.5}$$

where ξ_i are the components of vector $\mathbf{e}$ with respect to basis $\{\mathbf{f}\}$ and $\tilde{\xi}_i$ are its components with respect to basis $\{\tilde{\mathbf{f}}\}$. Substituting Eq. (A.4) in Eq. (A.5) yields:

$$\sum_{i=1}^{3} \tilde{\xi}_i\, \tilde{\mathbf{f}}_i = \sum_{i=1}^{3} \xi_i \sum_{j=1}^{3} q_{ij}\, \tilde{\mathbf{f}}_j = \sum_{j=1}^{3} \tilde{\mathbf{f}}_j \sum_{i=1}^{3} \xi_i\, q_{ij} \ . \tag{A.6}$$

Thus, the following relation for the components of vector $\mathbf{e}$ with respect to basis $\{\tilde{\mathbf{f}}\}$ in terms of its components with respect to basis $\{\mathbf{f}\}$ can be obtained:

$$\begin{bmatrix}\tilde{\xi}_1\\ \tilde{\xi}_2\\ \tilde{\xi}_3\end{bmatrix} = \left(\mathbf{P}^{-1}\right)^T \cdot \begin{bmatrix}\xi_1\\ \xi_2\\ \xi_3\end{bmatrix} , \tag{A.7}$$

i.e., transformation of vector components are defined by a matrix which is the transpose of the inverse of matrix $\mathbf{P}$. Analogously:

$$\begin{bmatrix}\xi_1\\ \xi_2\\ \xi_3\end{bmatrix} = \mathbf{P}^T \cdot \begin{bmatrix}\tilde{\xi}_1\\ \tilde{\xi}_2\\ \tilde{\xi}_3\end{bmatrix} . \tag{A.8}$$

In order to find the relation between the direction cosines of an arbitrary vector in the spatial and the directional coordinate systems, as depicted in Fig. 3.2, the basis transformation due to the rotation of the global coordinate system through an angle Φ about the Z-axis and then through an angle Ψ about the Y-axis has to be found. For the selected coordinate systems, the basis transformation, as given by Eq. (A.3), can be rewritten as follows:

$$\mathbf{x} = x_X\mathbf{X} + x_Y\mathbf{Y} + x_Z\mathbf{Z} , \tag{A.9}$$
$$\mathbf{y} = x_X\mathbf{X} + y_Y\mathbf{Y} + y_Z\mathbf{Z} , \tag{A.10}$$
$$\mathbf{z} = x_X\mathbf{X} + z_Y\mathbf{Y} + z_Z\mathbf{Z} , \tag{A.11}$$

where $\mathbf{x}$, $\mathbf{y}$, and $\mathbf{z}$ are the unit vectors defining the directions of the corresponding axes of the local coordinate system and $\mathbf{X}$, $\mathbf{Y}$, and $\mathbf{Z}$ are the unit vectors defining the directions of the corresponding axes of the global coordinate system. As can be easily derived from Fig. 3.2, the direction cosines of the x-, y-, and z-axes of the local coordinate system with respect to the global coordinate system are given by

$$\begin{bmatrix}x_X\\ x_Y\\ x_Z\end{bmatrix} = \begin{bmatrix}\cos\Psi\cos\Phi\\ \cos\Psi\sin\Phi\\ -\sin\Psi\end{bmatrix} , \quad \begin{bmatrix}y_X\\ y_Y\\ y_Z\end{bmatrix} = \begin{bmatrix}-\sin\Phi\\ \cos\Phi\\ 0\end{bmatrix} , \quad \text{and} \quad \begin{bmatrix}z_X\\ z_Y\\ z_Z\end{bmatrix} = \begin{bmatrix}\sin\Psi\cos\Phi\\ \sin\Psi\sin\Phi\\ \cos\Psi\end{bmatrix} , \tag{A.12}$$

respectively. Combining Eqns. (A.9)–(A.11) and Eq. (A.12), the following relation for the matrix of the transformation is obtained:

$$\mathbf{P} \equiv \begin{bmatrix}x_X & x_Y & x_Z\\ y_X & y_Y & y_Z\\ z_X & z_Y & z_Z\end{bmatrix} = \begin{bmatrix}\cos\Psi\cos\Phi & \cos\Psi\sin\Phi & -\sin\Psi\\ -\sin\Phi & \cos\Phi & 0\\ \sin\Psi\cos\Phi & \sin\Psi\sin\Phi & \cos\Psi\end{bmatrix} . \tag{A.13}$$

The inverse of the transformation matrix is given by

$$\mathbf{P}^{-1} = \begin{bmatrix}\cos\Psi\cos\Phi & -\sin\Phi & \sin\Psi\cos\Phi\\ \cos\Psi\sin\Phi & \cos\Phi & \sin\Psi\sin\Phi\\ -\sin\Psi & 0 & \cos\Psi\end{bmatrix} . \tag{A.14}$$

Thus, substituting Eq. (A.14) into Eq. (A.7) and using the notations of Section 3.3, the following formula for the transformation of the direction cosines can be obtained:

$$\begin{bmatrix} \eta \\ \xi \\ \zeta \end{bmatrix} \equiv \begin{bmatrix} \tilde{\xi}_1 \\ \tilde{\xi}_2 \\ \tilde{\xi}_3 \end{bmatrix} = \begin{bmatrix} \cos\Psi\cos\Phi & \cos\Psi\sin\Phi & -\sin\Psi \\ -\sin\Phi & \cos\Phi & 0 \\ \sin\Psi\cos\Phi & \sin\Psi\sin\Phi & \cos\Psi \end{bmatrix} \cdot \begin{bmatrix} \eta_0 \\ \xi_0 \\ \zeta_0 \end{bmatrix} . \tag{A.15}$$

In the same manner, combining Eqns. (A.13) and (A.8), for the inverse transformation is obtained:

$$\begin{bmatrix} \eta_0 \\ \xi_0 \\ \zeta_0 \end{bmatrix} \equiv \begin{bmatrix} \xi_1 \\ \xi_2 \\ \xi_3 \end{bmatrix} = \begin{bmatrix} \cos\Psi\cos\Phi & -\sin\Phi & \sin\Psi\cos\Phi \\ \cos\Psi\sin\Phi & \cos\Phi & \sin\Psi\sin\Phi \\ -\sin\Psi & 0 & \cos\Psi \end{bmatrix} \cdot \begin{bmatrix} \eta \\ \xi \\ \zeta \end{bmatrix} . \tag{A.16}$$

Appendix B

Calculation of angle variables along the line-of-sight in a spherical atmosphere

Any unit vector $\mathbf{e}_s$ can be represented by its three projections in any given coordinate system. For any point $\mathbf{r}_1$ in the atmosphere one can write

$$\mathbf{e}_s \equiv \begin{bmatrix} \eta_1 \\ \xi_1 \\ \zeta_1 \end{bmatrix} = \begin{bmatrix} \sin\Theta_1 \cos\varphi_1 \\ \sin\Theta_1 \sin\varphi_1 \\ \cos\Theta_1 \end{bmatrix} , \tag{B.1}$$

where η_1, ξ_1, and ζ_1 are the direction cosines of unit vector $\mathbf{e}_s$ in the local coordinate system at point $\mathbf{r}_1$ (see Fig. 7.1). In order to obtain global direction cosines of $\mathbf{e}_s$ the local ones have to be rotated:

$$\begin{bmatrix} \eta_0 \\ \xi_0 \\ \zeta_0 \end{bmatrix} = \mathbf{A}_1 \cdot \begin{bmatrix} \eta_1 \\ \xi_1 \\ \zeta_1 \end{bmatrix} , \tag{B.2}$$

where, according to Appendix A, rotation matrix $\mathbf{A}_1$ is given by

$$\mathbf{A}_1 = \begin{bmatrix} \cos\Psi_1 \cos\Phi_1 & -\sin\Phi_1 & \sin\Psi_1 \cos\Phi_1 \\ \cos\Psi_1 \sin\Phi_1 & \cos\Phi_1 & \sin\Psi_1 \sin\Phi_1 \\ -\sin\Psi_1 & 0 & \cos\Psi_1 \end{bmatrix} . \tag{B.3}$$

Performing the multiplication in the right hand side of Eq. (B.2), the following formulas for global direction cosines can be obtained :

$$\eta_0 = \cos\Psi_1 \cos\Phi_1 \sin\Theta_1 \cos\varphi_1 - \sin\Phi_1 \sin\Theta_1 \sin\varphi_1 + \sin\Psi_1 \cos\Phi_1 \cos\Theta_1 \tag{B.4}$$

$$\xi_0 = \cos\Psi_1 \sin\Phi_1 \sin\Theta_1 \cos\varphi_1 + \cos\Phi_1 \sin\Theta_1 \sin\varphi_1 + \sin\Psi_1 \sin\Phi_1 \cos\Theta_1 \tag{B.5}$$

$$\zeta_0 = -\sin\Psi_1 \sin\Theta_1 \cos\varphi_1 + \cos\Psi_1 \cos\Theta_1 \tag{B.6}$$

Since the global direction cosines remain unchanged along the line-of-sight, the local direction cosines at point $\mathbf{r}_2$ can be found as follows:

$$\begin{bmatrix} \eta_2 \\ \xi_2 \\ \zeta_2 \end{bmatrix} = \mathbf{A}_2^{-1} \cdot \begin{bmatrix} \eta_0 \\ \xi_0 \\ \zeta_0 \end{bmatrix} , \tag{B.7}$$

where $\mathbf{A}_2^{-1}$ is given by

$$\mathbf{A}_2^{-1} = \begin{bmatrix} \cos\Psi_2 \cos\Phi_2 & \cos\Psi_2 \sin\Phi_2 & -\sin\Psi_2 \\ -\sin\Phi_2 & \cos\Phi_2 & 0 \\ \sin\Psi_2 \cos\Phi_2 & \sin\Psi_2 \sin\Phi_2 & \cos\Psi_2 \end{bmatrix} . \tag{B.8}$$

The cosines of the solar zenith and the global azimuth angle (i.e., $\cos\Psi_2$ and $\cos\Phi_2$) at point $\mathbf{r}_2$ can be found solving the following vector equation:

$$\mathbf{r}_2 = \mathbf{r}_1 - s\,\mathbf{e}_s , \tag{B.9}$$

where $\mathbf{s} = s\,\mathbf{e}_s$ is the vector connecting points $\mathbf{r}_2$ and $\mathbf{r}_1$. Since vector $\mathbf{s}$ defines the direction of the radiance, it originates in $\mathbf{r}_2$ and points to $\mathbf{r}_1$. The Z-projection of Eq. (B.9) yields:

$$r_2 \cos\Psi_2 = r_1 \cos\Psi_1 - s\,\zeta_0 , \tag{B.10}$$

and hence:

$$\cos\Psi_2 = \frac{r_1}{r_2} \cos\Psi_1 - \frac{s}{r_2}\,\zeta_0 . \tag{B.11}$$

The X-projection of Eq. (B.9) yields:

$$r_2 \sin\Psi_2 \cos\Phi_2 = r_1 \sin\Psi_1 \cos\Phi_1 - s\,\eta_0 , \tag{B.12}$$

and hence:

$$\cos\Phi_2 = \frac{r_1 \sin\Psi_1}{r_2 \sin\Psi_2} \cos\Phi_1 - \frac{s}{r_2 \sin\Psi_2}\,\eta_0 \tag{B.13}$$

and the Y-projection of Eq. (B.9) yields:

$$r_2 \sin\Psi_2 \sin\Phi_2 = r_1 \sin\Psi_1 \sin\Phi_1 - s\,\xi_0 , \tag{B.14}$$

and hence:

$$\sin\Phi_2 = \frac{r_1 \sin\Psi_1}{r_2 \sin\Psi_2} \sin\Phi_1 - \frac{s}{r_2 \sin\Psi_2}\,\xi_0 . \tag{B.15}$$

Performing the multiplication in the right hand side of Eq. (B.7) and taking into account Eq. (B.1), the following formulas for angle variables Θ_2 and φ_2 at an arbitrary point $\mathbf{r}_2$ on the line-of-sight can be obtained:

$$\cos\Theta_2 = \sin\Psi_2 \cos\Phi_2\,\eta_0 + \sin\Psi_2 \sin\Phi_2\,\xi_0 + \cos\Psi_2\,\zeta_0 , \tag{B.16}$$

$$\cos\varphi_2 = \frac{1}{\sin\Theta_2} \left(\cos\Psi_2 \cos\Phi_2\,\eta_0 + \cos\Psi_2 \sin\Phi_2\,\xi_0 - \sin\Psi_2\,\eta_0\right) . \tag{B.17}$$

Substitution of Eqns. (B.4), (B.5), (B.6), (B.13), and (B.15) in Eqns. (B.16) and (B.17), and rewriting Eqns. (B.11) and (B.13) enables the following formulas for angle variables Ψ_2, Φ_2, Θ_2, and φ_2 at an arbitrary point $\mathbf{r}_2$ on the line-of-sight to be obtained:

$$\cos\Psi_2 = \frac{r_1\,\cos\Psi_1 - s\,\zeta_0}{r_2}\,, \tag{B.18}$$

$$\cos\Phi_2 = \frac{r_1 \sin\Psi_1 \cos\Phi_1 - s\,\eta_0}{r_2 \sin\Psi_2}\,, \tag{B.19}$$

$$\cos\Theta_2 = \frac{r_1 \cos\Theta_1 - s}{r_2}\,, \tag{B.20}$$

$$\cos\varphi_2 = \frac{\cos\tilde{\Psi}_2\,\cos\Theta_2 - \zeta_0}{\sin\Psi_2\,\sin\Theta_2}\,. \tag{B.21}$$

Bibliography

Abreu, V. J., A. Bucholtz, P. B. Hays, D. Ortland, W. R. Skinner, and J. H. Yee, Absorption and emission line shapes in the O_2 atmospheric bands: Theoretical model and limb viewing simulations, Appl. Opt., *28 (11)*, 2128-2137, 1989.

Abulwafa, E. M., and M. T. Attia, Radiative transfer in a spherical medium by the Pomraning-Eddington technique, *J. Quant. Spectrosc. Radiat. Transfer*, *58*, 101-114, 1997.

Anderson, D. E., The troposphere – stratosphere radiation field at twilight: A spherical model, *Planet. Space Sci.*, *31*, 1517-1523, 1983.

Anderson, D. E., Jr., and S. A. Lloyd, Polar twilight UV-Visible radiation field: perturbations due to multiple scattering, ozone depletion, stratospheric clouds, and surface albedo, *J. Geophys. Res.*, *95 (D6)*, 7429-7434, 1990.

Anderson, J., J. M. Russel III, S. Solomon, and L. E. Deaver, Halogen Occultation Experiment confirmation of stratospheric chlorine decreases in accordance with the Montreal Protocol, *J. Geophys. Res.*, *105*, 4483-4490, 2000.

Anderson, G. P., S. A. Clough, F. X. Kneizys, J. H. Chetwynd, and E. P. Shettle, AFGL Atmospheric Constituent Profiles (0–120 km), *Tech. Rep.*, AFGL-TR-86-0110, AD A 175173, 1986.

Arrhenius, S., On the influence of carbonic acid in the air upon the temperature of the ground, *Philosophical magazine and Journal of Science*, *41, 237, 1896.*

Bates, D. R., Rayleigh scattering by air, *Planet. Space Sci.*, *32*, 785-790, 1984.

Bates, D. R., and M. Nicolet, Atmospheric hydrogen, *Publ. Astron. Soc. Pac.*, *62*, 106-110, 1950.

Balluch, M., A new numerical model to compute photolysis rates and solar heating with anisotropic scattering in spherical geometry, *Ann. Geophysicae*, *14*, 80-97, 1996.

Blindauer, C., V. Rozanov, J. P. Burrows, Actinic flux and photolysis frequency comparison computations using the model PHOTOGT, *J. Atm. Chem.*, *24*, 1–21, 1996.

Bovensmann, H., J. P. Burrows, M. Buchwitz, J. Frerick, S. Noël, and V.V. Rozanov, SCIAMACHY: Mission objectives and measurement modes, *J. Atm. Sci.*, *56 (2)*, 127-149, 1999.

Breene, R. G., *The shift and shape of spectral lines*, Pergamon Press, London, 1961.

Brühl, Ch., and P. J. Crutzen, *MPIC Two-dimensional model*, in: The atmospheric effects of stratospheric aircraft, NASA Ref. Publ. 1292, 103-104, 1993.

Bucholtz, A., Rayleigh-scattering calculations for the terrestrial atmosphere, *Appl. Opt.*, *34 (15)*, 2765-2773, 1995.

Burrows, J. P., and K. V. Chance, Scanning imaging absorption spectrometer for atmospheric chartography, *Proc. SPIE*, *1490*, 146-155, 1991.

Burrows, J. P., M. Weber, M. Buchwitz, V. Rozanov, A. Ladstätter-Weißenmayer, A. Richter, R. de Beek, R. Hoogen, K. Bramstedt, K.-U. Eichmann, M. Eisinger, and D. Perner, The Global Ozone Monitoring Experiment (GOME): Mission concept and first scientific results, *J. Atmos. Sci.*, *56*, 151-175, 1999.

Caudill, T. R., D. E. Flittner, B. M. Herman, O. Torres, and R. D. McPeters, Evaluation of the pseudo-spherical approximation for backscattered ultraviolet radiances and ozone retrieval, *J. Geophys. Res.*, *102*, 3881-3890, 1997.

Collins, D. G., W. G. Bittner, M. B. Wells, and H. G. Horak, Backward Monte Carlo calculations of the polarization characteristics of the radiation emerging from spherical-shell atmospheres, *Appl. Opt.*, *11*, 2684-2696, 1972.

Chance, K., and R. J. D. Spurr, Ring effect studies: Rayleigh scattering, including molecular parameters for rotational Raman scattering, and the Fraunhofer spectrum, *Appl. Opt.*, *36*, 5224-5230, 1997.

Chandra, S., C. H. Jackman, E. L. Fleming, and J. M. Russel III, The seasonal and long term changes in mesospheric water vapor, *Geophys. Res. Lett.*, *24*, 639-642, 1997.

Chandrasekhar, S., *Radiative transfer*, Dover Publications Inc., New York, 1960.

Chapman, S., On ozone and atomic oxygen in the upper atmosphere, *Philos. Mag.*, *10*, 369-383, 1930.

Chu, W. P., and M. P. McCormic, Inversion of stratospheric aerosole and gaseous constituents from spacecraft solar extinction data in the 0.38–1.0 μm wavelength region, *Appl. Opt.*, *18*, 1404-1413, 1979.

Crutzen, P. J., The influence of nitrogen oxide the atmospheric ozone content, *Q. J. R. Meteorol. Soc.*, *96*, 320-327, 1970.

Currant, R., and D. Hilbert, *Methods of Mathematical Physics*, Vol. 2, Interscience, New York, 1962.

d'Almeida, G. A., P. Koepke, and E. P. Shettle, *Atmospheric aerosols: global climatology and radiative characteristics*, A. DEEPAK Publishing, Hampton, Virginia, 1991.

Dahlback, A., and K. Stamnes, A new spherical model for computing the radiation field available for photolysis at heating at twilight, *Planet. Space Sci.*, *39*, 671-683, 1991.

Dave, J.V. and C. L. Mateer, A preliminary study on the possibility of estimating total atmospheric ozone from satellite measurements, *J. Atmos. Sci.*, *24*, 414-427, 1967.

Deirmendjian, D., *Electromagnetic scattering on spherical polydispersions*, American Elsevier Pub. Co., New York, 1969.

DeLuisi, J. J., and C. L. Mateer, On the application of the optimum statistical inversion technique to the evaluation of Umkehr observations, *J. Appl. Meteorol.*, *10*, 328-334, 1971.

Dobson, G. M. B., Forty years research on atmospheric ozone at Oxford: A history, *Appl. Opt.*, *129*, 387-405, 1968.

Edlén, B., The dispersion of standard air, *J. Opt. Soc. Am.*, *43*, 339-344, 1953.

Edlén, B., The refractive index of air, *Meteorogia*, *2*, 71-80, 1966.

Elkins, J. W., T. M. Thompson, T. H. Swanson, J. H. Butler, B. D. Hall, S. O. Cummings, D. A. Fisher and A. G. Raffo, Decrease in the growth rates of atmospheric chlorofluorocarbons 11 and 12, *Nature*, *364*, 780-783, 1993.

Evans, K. F., The spherical harmonics discrete ordinate method for three-dimensional atmospheric radiative transfer, *J. Atmos. Sci.*, *55*, 429-446, 1998.

Evans, S. J., R. Toumi, J. E. Harries, M. P. Chipperfield, and J. M. Russel III, Trends in stratospheric humidity and the sensitivity of ozone to these trends, *J. Geophys. Res.*, *103*, 8715-8725, 1998.

Farman, J. C., B. G. Gardiner, and J. D. Shanklin, Large losses of total ozone in Antarctica reveal seasonal ClO_x/NO_x interaction, *Nature*, *315*, 207-210, 1985.

Fay, J. A., *Molecular Thermodynamics*, Addison-Wesley Pub. Co., Reading, MA, 1965.

Fleig, A. J., R. D. McPeters, P. K. Bhartia, B. M. Schlesinger, R. P. Cebula, K. F. Klenk, S. L. Taylor, and D. F. Heath, Nimbus 7 Solar Backscatter Ultraviolet (SBUV) ozone products user's guide, *NASA Ref. Pub.*, *1234*, 1990.

Frerick, J., H. Bovensmann, S. Noël, J. Burrows, and M. Dobber, SCIAMACY on-ground/in-flight calibration, performance verification and monitoring concepts, Proc. SPIE, *3117*, 176-187, 1997.

Fröhlich, C., and G. E. Shaw, New determination of Rayleigh scattering in the terrestrial atmosphere, *Appl. Opt.*, *19*, 1773-1775, 1980.

Gamache, R. R., R. L. Hawkins, and L. S. Rothman, Total internal partition sums in the temperature range 70-3000 K: Atmospheric linear molecules, *J. Molec. Spec.*, *142*, 205-219, 1990.

Germogenova, T. A., L. L. Koprova, and T. A. Sushkevich, A study of the angular, spatial, and spectral structure of the terrestrial brightness field for a representative model of the spherical atmosphere, *Bull. (Izv.) Acad. Sci. USSR*, *Atmos. and Oceanic Phys.*, *5 (12)*, 1266-1277, 1969.

Goede, A.P.H., P. de Groene, R. W. M. Hoogeveen, J. de Vries, J. R. van der A, A. C. Smorenburg, and H. Visser, SCIAMACHY instrument development for POEM-1, *Adv. Space Res.*, *14*, 17-20, 1994.

Goede, A.P.H., SCIAMACHY instrument concept, *Proc. European Symposium on Atmospheric Measurements from Space*, 18-22 January, ESTEC, Noorwijk, The Netherlands, 147-154, 1999.

Goody R.M., *Atmospheric Radiation: 1. Theoretical Basis*, Clarendon Press, Oxford, 1964.

Harrison, A. W., Midsummer stratospheric NO_2 at 45°S, *Can. J. Phys.*, *57*, 1110-1117, 1979.

Heath, D. F., A. J. Krueger, H. A. Roeder, and D. B. Henderson, The Solar Backscatter Ultraviolet and Total Ozone Mapping Spectrometer (SBUV/TOMS) for Nimbus G, *Opt. Eng.*, *14, 323-331, 1975.*

Herman, B. M., A. Ben-David, and K. J. Thome, Numerical technique for solving the radiative transfer equation for a spherical shell atmosphere, *Appl. Opt.*, *3*, 1760-1770, 1994.

Hirsh, M.W. and S. Smale, *Differential Equations, Dynamical Systems, and Linear Algebra*, Academic Press, Orlando, FL, 1974.

Holton, J. R., P. H. Haynes, M. E. McIntyre, A. R. Douglass, R. B. Hood, and L. Pfister, Stratosphere-troposphere exchange, *Rev. Geophys.*, *33*, 403-439, 1995.

Hoogen, R., V. V. Rozanov, and J. P. Burrows, Ozone profiles from GOME satellite data: Algorithm description and first validation, *J. Geophys. Res.*, *104*, 8263-8280, 1999.

Hoyt, D. V., A redetermination of the Rayleigh optical depth and its application to selected solar radiation problems, *J. Appl. Meteorol.*, *16*, 432-436, 1977.

Hui, A. K., B. H. Armstrong, and A. A. Wray, Rapid computation of the Voigt and complex error functions, *J. Quant. Spectrosc. Radiat. Transfer*, *19*, 509, 1978.

Humlicek, J., Optimized computation of the Voigt and complex probability functions, *J. Quant. Spectrosc. Radiat. Transfer*, *27*, 437, 1982.

Johnson, P. V., R. L. McKenzie, J. G. Keys, and W. A. Matthews, Observations of depleted stratospheric NO_2 following the Pinatubo volcanic eruption, Geophys. Res. Lett., *19*, 211-213, 1992.

Jones, P. D., and Y. Bayazitoglu, Coordinate systems for the radiative transfer equation in curvilinear media, *J. Quant. Spectrosc. Radiat. Transfer*, *48*, 427-440, 1992.

Incropera, F. P., *Introduction to molecular structure and thermodynamics*, John Wiley & Sons, New York, 1974.

IPCC, *Climate Change: The IPCC scientific assessment*, Edited by J. T. Houghton, G. J. Jenkins and J. J. Ephraums, Cambridge University Press, 1990.

IPCC, *Climate Change 1995: The Science of Climate Change*, Cambridge University Press, 572 pp., 1996.

Kerker, M., *The scattering of light and other electromagnetic radiation*, Academic Press, San Diego, California, 1969.

King, L. V., On the complex anisotropic molecule in relation to the dispersion and scattering of light, *Proc. Roy. Soc. London*, *A 104*, 333-357, 1923.

Klenk, K. F., P. K. Bhartia, A. J. Fleig, V. G. Kaveeshwar, R. D. McPeters, and P. M. Smith, Total ozone determination from backscattered ultraviolet (BUV) experiment, *J. Appl. Meteorol.*, *21*, 1672-1684, 1982.

Koepke. P., A. Bais, D. Balis, M. Buchwitz, H. De Baker, X. de Cabo, P. Eckert, P. Eriksen, D. Gillotay, A. Heikkilä, T. Koskela, B. Lapeta, Z. Litynska, J. Lorente, B. Mayer, A. Renaud, A. Ruggaber, G. Schauberger, G. Seckmeyer, P. Seifert, A. Schwalwieser, H. Schwander, K. Vanicek, M. Weber, Comparison of models used for UV index calculations, *Photochem. and Photobiol.*, *67 (6)*, 657–662, 1998.

Kondratjev, K., Ia., G. I. Marchuk, A. A. Buznikov, I. N. Minin, G. A. Mikhailov, M. A. Nazaraliev, B.M. Orlov, O.I. Smoktii, *Radiation Field in the Spherical Atmosphere*, Leningrad University press, Leningrad, 1977, in Russian.

Korn, G.A., and Korn T.M., *Mathematical Handbook for Scientists and Engineers*, McGraw-Hill Book Company, New York, 1968.

Kozlov, V. P., Design of Experiments Related to the Inverse Problem of Mathematical Physics, in *Mathematical Theory of Experiment Design*, edited by C. M. Ermakov, pp. 216-246, Nauka, Moscow, 1983, in Russian.

Kneizys, F., L. Abreu, G. Anderson, J. Chetwynd, E. Shettle, A. Berk, L. Bernstein, D. Robertson, P. Acharya, L. Rothman, J. Selby, W. Gallery, and S. Clough, The MODTRAN 2/3 report and LOWTRAN 7 model, *Tech. Rep., contract F19628-91-C-0132 with Ontar Corp.*, Phillips Laboratory, Hanscom AFB, 1996.

Kuo, K.-S., R. C. Weger, and R. M. Welch, The Picard iterative approximation to the solution of the integral equation of radiative transfer – part 1. The plane-parallel case, *J. Quant. Spectrosc. Radiat. Transfer*, *53*, 425-444, 1995.

Kuo, K.-S., R. C. Weger, R. M. Welch, and S. K. Cox, The Picard iterative approximation to the solution of the integral equation of radiative transfer – part 1. Three-dimensional geometry, *J. Quant. Spectrosc. Radiat. Transfer*, *55*, 195-213, 1996.

Lenoble, J., and Z. Sekera, Equation of radiative transfer in a planetary atmosphere, *Proc. Nat. Acad. Sci*, *47*, 372-389, USA, 1961.

Lenoble, J., *Radiative Transfer in Scattering and Absorbing Atmospheres*, pp. 34-82, A. DEEPAK Publishing, Hampton, Virginia, 1985.

Levy, H., II, J. D. Mahlman, and W. F. Moxim, A stratospheric source of reactive nitrogen in the unpolluted troposphere, *Geophys. Res. Lett.*, *7*, 441-444, 1980.

Llewellyn, E. J., D. A. Degenstein, I. C. McDade, R. L. Gattinger, R. King, R. Buckingham, E. H. Richardson, D. P. Murtagh, W. F. J. Evans, B. H. Solheim, K. Strong, and J. C. McConnell, OSIRIS – an application of tomography for absorbed emissions in remote sensing, in Applications of Photonic technology 2, edited by G. A. Lampropoulos and R. A. Lessard, 627-632, Plenum Press, New York, 1997.

Lovelock, J. E., R. J. Maggs, and R. J. Wade, Halogenated hydrocarbons in and over the Atlantic, *Nature*, *241*, 194, 1973.

Madkour, M. A., Radiation transfer in a spherical inhomogeneous medium by the projection method, *J. Quant. Spectrosc. Radiat. Transfer*, *56*, 303-308, 1996.

Mager, R., W. Fricke, J. P. Burrows, J. Frerick, and H. Bovensmann, SCIAMACHY - A new generation of hyperspectral remote sensing instrument, *Spectroscopic Atmospheric Monitoring Techniques*, K. Schaefer Ed., SPIE, 84-94, 1997.

Marchuk, G. I., G. A. Mikhailov, M. A. Nazaraliev, R. A. Darbinjan, B. A. Kargin, and B. S. Elepov, *The Monte Carlo Methods in Atmospheric Optics*, Springer Series in Optical Sciences, Berlin, 1980.

Mateer, C. L., and J. J. DeLuisi, A new Umkehr inversion algorithm, *J. Atmos. Terr. Phys.*, *54*, 537-556, 1992.

Mauldin, L. E., III, N. H. Zaun, M. P. McCormick, Jr., L. H. Guy, and W. R. Vaughn, Stratospheric Aerosol and Gas Experiment II instrument: a functional description, *Opt. Eng.*, *24*, 112-117, 1985.

McCormick, M. P., P. Hamill, T. J. Pepin, W. P. Chu, T. J. Swissler, and L. R. McMaster, Satellite studies of the stratospheric aerosol, *Bull. Am. Meteorol. Soc.*, *9*, 1038-1046, 1979.

McCormick, M. P., T. J. Swissler, E. Hilsenrath, A. J. Krueger, and M. T. Osborn, Satellite and correlative measurements of stratospheric ozone: Comparison of measurements made by SAGE, ECC Balloons, chemiluminescent, and optical rocketsondes, *J. Geophys. Res.*, *89 (D4)*, 5315-5320, 1984.

McElroy, M. B., R. J. Salawitch, S. C. Wofsy, and J. A. Logan, Reduction of Antarctic ozone due to synergistic interactions of chlorine and bromine, *nature*, *321*, 759-762, 1986.

McLinden, C. A., J. C. McConnel, C. T. McElroy, and E. Griffioen, Observations of stratospheric aerosol using CPFM polarized limb radiances, *J. Atm. Sci*, *56*, 233-240, 1999.

McPeters, R. D., P. K. Bhartia, A. J. Krueger, J. R. Herman, B. M. Schlesinger, C. G. Wellemeyer, C. J. Seftor, G. Jaross, S. L. Taylor, T. Swissler, O. Torres, G. Labow, W. Byerly, and R. P. Cebula, Nimbus-7 Total Ozone Mapping Spectrometer (TOMS) data products user's guide, *NASA Ref. Pub.*, *1384*, 1996.

Meier, R.R., D. E. Anderson, Jr., and M. Nicolet, Radiation field in the troposphere and stratosphere: 1. General analysis, *Planet. Space Sci.*, *30*, 923-933, 1982.

Mie, G., Beiträge zur Optik trüber Medien, speziell kolloidaler Metallösungen, *Ann. Phys.*, *25*, 377-445, 1908.

Molina, M. J., and F. S. Rowland, Stratospheric sinn for chlorofluoromethanes: Chlorine atom catalyzed destruction of ozone, *Nature*, *249*, 810-812, 1974.

Montzka, S. A., J. H. Butler, R. C. Myers, T. M. Thompson, T. H. Swanson, A. D. Clarke, L. T. Lock, and J. W. Elkins, Decline in the tropospheric abundance of halogen from halocarbons: Implications for Stratospheric Ozone depletion, *Nature*, *272*, 1318-1322, 1996.

Mount, G. H., D. W. Rusch, J. F. Noxon, J. M. Zawodny, and C. A. Barth, Measurements of stratospheric NO_2 from the Solar Mesosphere Explorer satellite. 1. An overview of the results, *J. Geophys. Res.*, *89 (D1)*, 1327-1340, 1984.

Mount, G. H., R. W. Sanders, A. L. Schmeltekopf, and S. Solomon, Visible spectroscopy at McMurdo station, Antarctica. 1. Overview and daily variations of NO_2, *J. Geophys. Res.*, *92*, 8320-8329, 1987.

Müller, R., P. J. Crutzen, J. U. Grooß, C. Brühl, J. M. Russel III, H. Gernandt, D. S. McKenna, and A. F. Tuck, Severe chemical ozone loss in the Arctic during the winter of 1995-1996, *Nature*, *398*, 709-712, 1997.

Muthama, N. J., U. Scimia, A. M. Siani, and S. Palmieri, Toward optimizing Brewer zenith sky total ozone measurements at the Italian stations of Rome and Ispra, *J. Geophys. Res.*, *100 (D2)*, 3017-3022, 1995.

NASA, *U.S. Standard Atmosphere Supplements*, U.S. Government Printing Office, Washington, D.C., 1976.

Naudet, J. P., and G. E. Thomas, Aerosol optical depth and planetary albedo in the visible from the Solar Mesosphere Explorer, *J. Geophys. Res.*, *92 (D7)*, 8373-8381, 1987.

Nelder, J. A., and R. Mead, A Simplex method for function minimization, *Comput. J.*, *7*, 308-313, 1965.

Newman, P. A., Antarctic total ozone in 1958, *Science*, *264*, 543-546, 1994.

Newman, P. A., J. F. Gleason, R. D. McPeters, and R. S. Stolarski, Anomalously low ozone over the Arctic, *Geophys. res. Lett.*, *24*, 2689-2692, 1997.

Noxon, J. F., Nitrogen dioxide in the stratosphere and troposphere measured by ground based absorption spectroscopy, *Science*, *189*, 547-549, 1975.

O'Brien, D. C., Accelerated quasi Monte Carlo integration of the radiative transfer equation, *J. Quant. Spectrosc. Radiat. Transfer*, *48*, 41-59, 1992.

Oikarinen, L., E. Sihvola, and E. Kyrölä, Multiple scattering radiance in limb-viewing geometry, *J. Geophys. Res.*, *104 (D24)*, 31261-31275, 1999.

Peck, E. R., and K. Reeder, Dispersion of air, *J. Opt. Soc. Am.*, *62*, 958-962, 1972.

Penndorf, R., Tables of refractive index for standard air and the Rayleigh scattering coefficient for the spectral region between 0.2 and 20.0 μm and their application to atmospheric optics, *J. Opt. Soc. Am.*, *47*, 176-182, 1957.

Perliski, L., and S. Solomon, On the evaluation of air mass factors for atmospheric near-ultraviolet and visible absorption spectroscopy, *J. Geophys. Res.*, *98 (D6)*, 10363-10374, 1993.

Popescu, A. F., and T. Paulsen, The Global Ozone Monitoring by Occultation of stars (GOMOS) instrument on ENVISAT: requirements, design and development status, *Proc. European Symposium on Atmospheric Measurements from Space*, 18-22 January, ESTEC, Noorwijk, The Netherlands, 89-99, 1999.

Ramaswamy, V., M. D. Schwarzkopf, and K. P. Shine, Radiative forcing of climate from halocarbon-induced global stratospheric ozone loss, *Nature*, *355*, 810-812, 1992.

Richter, A., M. Eisinger, A. Ladstatter-Weißenmayer, and J. P. Burrows, DOAS zenith sky observations. 2. Seasonal variation of BrO over Bremen (53°N) 1994-1995, *J. Atm. Chem.*, *32*, 83-99, 1999.

Ridley, B. A., S. H. Luu, D. R. Hastie, H. I. Schiff, J. C. McConnell, W. F. J. Evans, C. T. McElroy, J. B. Kerr, H. Fast, and R. S. O'Brien, Stratospheric odd nitrogen: Measurements of HNO_3, NO, NO_2, and O_3 near 54°N in winter, *J. Geophys. Res.*, *89*, 4797-4820, 1984.

Rodgers, C.D., Retrieval of Atmospheric Temperature and Composition From Remote Measurements of Thermal Radiation, *Reviews of Geophysics and Space Physics*, *4*, 609-624, 1976.

Rodgers, C.D., Characterization and error analysis of profiles retrieved from remote sounding measurements, *J. Geophys. Res.*, *95*, 5587-5595, 1990.

Rothman, L. S., C. P. Rinsland, A. Goldman, S. T. Massie, D. P. Edwards, J.-M. Flaud, A. Perrin, C. Camy-Peyret, V. Dana, J.-Y. Mandin, J. Schroeder, A. McCann, R. R. Gamache, R. B. Wattson, K. Yoshino, K. V. Chance, K. W. Jucks, L. R. Brown, V. Nemtchinov, and P. Varanasi, The HITRAN molecular spectroscopic database and HAWKS (HITRAN atmospheric workstation): 1996 edition, *J. Quant. Spectrosc. Radiat. Transfer*, *60 (5))*, 665-710, 1998.

Rozanov, V., D. Diebel, R. J. D. Spurr, and J. P. Burrows, GOMETRAN: A radiative transfer model for the satellite project GOME, the plane-parallel version, *J. Geophys. Res.*, *102*, 16683-16695, 1997.

Rozanov, A., V. Rozanov, M. Buchwitz, and J. P. Burrows, A radiative transfer model for SCIAMACHY limb measurements, *Proc. European Symposium on Atmospheric Measurements from Space*, 18-22 January, ESTEC, Noorwijk, The Netherlands, 89-99, 1999.

Rozanov, A., V. Rozanov, F. Wittrock, and J. P. Burrows, A new radiative transfer model for DOAS interpretation of off-axis measurements, *Proc. Fifth European Workshop on Stratospheric Ozone*, 27 Sep – 1 Oct, St Jean de Luz, France, 1999.

Rozanov, A., V. Rozanov, and J. P. Burrows, Combined differential-integral approach for the radiation field computation in a spherical shell atmosphere: Non-limb geometry, *J. Geophys. Res.*, *105*, 22937-22942, 2000.

Rozanov, V. V., M. Buchwitz, and J. P. Burrows, SCIATRAN - A new radiative transfer model for geophysical applications in the 240-2400 nm spectral region: the pseudo-spherical version, to appear in *Advances in Space Research*, 2000c.

Rozanov, A., V. Rozanov, and J. P. Burrows, A numerical radiative transfer model for a spherical planetary atmosphere: Combined differential–integral approach involving the Picard iterative approximation, *J. Quant. Spectrosc. Radiat. Transfer*, *69*, 491-512, 2001.

Russel, J. M., III, L. L. Gordley, J. H. Park, S. R. Drayson, W. D. Hesketh, R. J. Cicerone, A. F. Tuck, J. E. Frederick, J. E. Harries, and P. J. Crutzen, The Halogen Occultation Experiment, *J. Geophys. Res.*, *98*, 10777-10797, 1993.

Sanders, R. W., S. Solomon, M. A. Caroll, and A. L. Schmeltekopf, Visible and Near-Ultraviolet spectroscopy at McMurdo station, Antarctica. 4. Overview and daily measurements of NO_2, O_3, and OClO during 1987, *J. Geophys. Res.*, *94*, 11381-11391, 1989.

Sen, K. K., S. J. Wilson, *Radiative Transfer in Curved Media*, World Scientific Publishing, 1990.

Shannon, C. E., and W. Weaver, *The mathematical theory of communication*, Univ. of Illinois Press, Urbana, 1949.

Shindell, D. T., D. Rind, and P. Logan, Increased polar stratospheric ozone losses and delayed eventual recovery owing to increasing greenhouse concentrations, *Nature*, *392*, 589-592, 1998.

Slusser, J., K. Hammond, A. Kylling, K. Stamnes, L. Perliski, A. Dahlback, D. Anderson, and R. DeMajistre, Comparison of air mass calculations, *J. Geophys. Res.*, **101**, 9315–9321, 1996.

Sinnhuber, B.-M., R. W. Müller, V. Eyring, U. Klein, J. Langer, J. Trentmann, H. Bovensmann, J.P. Burrows, and K. Künzi, Interpretation of Mid-Arctic Stratospheric Ozone Measurements Using a Photochemical Box Model, *J. Atm. Chem.*, *34 (3)*, 281-290, 1999.

Smokty, O. I., Determining the brightness of an inhomogeneous, spherically symmetrical planetary atmosphere, *Bull. (Izv.) Acad. Sci. USSR, Atmos. and Oceanic Phys.*, *3 (4)*, 383-393, 1967.

Smokty, O. I., *Modeling of Radiation Fields in Problems Space Spectrophotometry*, "Nauka" Publishers, Leningrad, 1986.

Sobel'man, I. I., *Introduction to the theory of atomic spectra*, Pergamon Press, Oxford, 1972.

Sobolev, V. V., Approximate method to solve the light scattering problem in the medium with arbitrary phase function, *Astronomical Journal*, *20*, 14-22, 1943, in Russian.

Sobolev, V. V., I. N. Minin, Light scattering in the spherical atmosphere, in *Artifical Earth's Satellites*, 7-12, Leningrad, 1962, in Russian.

Sobolev, V., *Light Scattering in Planetary Atmospheres*, Pergamon Press, Oxford, 1975.

Solomon, S., A. L. Schmeltekopf, R. W. Sanders, On the interpretation of zenith sky absorption measurements, *J. Geophys. Res.*, *92*, 8311-8319, 1987.

Solovjev, V. P., Solution of the radiative transfer equation by the moment method using polynomials of special form, *J. Quant. Spectrosc. Radiat. Transfer*, *47*, 229-236, 1992.

Stamnes, K., S.-C. Tsay, W. Wiscombe, and K. Jayaweera, Numerically stable algorithm for discrete-ordinate-method radiative transfer in multiple scattering and emitting layered media, *Appl. Opt.*, *27 (12)*, 2502-2509, 1988.

Steinacker, J., E. Thamm, and U. Maier, Efficient integration of intensity functions on the unit sphere, *J. Quant. Spectrosc. Radiat. Transfer*, *56*, 97-107, 1996.

Stolarski, R. S., and R. J. Cicerone, Stratospheric chlorine: A possible sink for ozone, *Can. J. Chem.*, *52*, 1610-1615, 1974.

Stratton, J. A., *Electromagnetic theory*, McGraw-Hill, New York, 1941.

Sushkevich, T. A., S. A. Strelkov, A. A. Ioltuhovskii, *Characteristic method in atmospheric optics*, "Nauka" Publishers, Moscow, pp. 296, 1990, in Russian.

Toumi, R., S. Bekki, and K. S. Law, Indirect influence of ozone depletion on climate forcing by clouds, *Nature*, *372*, 348-351, 1994.

Townes, C. H., and A. L. Schawlow, *Microwave spectroscopy*, Dover Publications Inc., New York, 1975.

Vaillon, R., M. Lallemand, and D. Lemonnier, Radiative heat transfer in orthogonal curvilinear coordinates using the discrete ordinates method, *J. Quant. Spectrosc. Radiat. Transfer*, *55*, 7-17, 1996.

van de Hulst, H. C., *Light scattering by small particles*, Wiley, New York, 1957.

Wilson, S. J., and K. K. Sen, Light scattering by an optically thin inhomogeneous spherically symmetric planetary atmosphere, *Astrophys. and Space Sci.*, *69*, 107-113, 1980a.

Wilson, S. J., and K. K. Sen, Light scattering by an optically thin inhomogeneous spherically symmetric planetary atmosphere: Brightness of the zenith near the terminator, *Astrophys. and Space Sci.*, *71*, 405-410, 1980b.

Wilson, S. J., F. S. Wan, and K. K. Sen, On the moment method for radiative transfer in spherical dust sells with a core, *Astrophys. and Space Sci.*, *67*, 99-103, 1980.

Wittrock, F., H. Altmeyer, M. Bruns, M. Laue, K. Munderloch, A. Richter, S. Schliter, and J. P. Burrows, Observations of O_3, NO_2, BrO, and OClO at different latitudes, *Proc. Fifth European Workshop on Stratospheric Ozone*, 27 Sep – 1 Oct, St Jean de Luz, France, 1999.

Wofsy, S. C., M. B. McElroy, and Y. L. Yung, The chemistry of atmospheric bromine, *Geophys. Res. Lett.*, *2*, 215-218, 1975.

WMO, Global Ozone Research and Monitoring Project, scientific assessment of ozone depletion 1994, *WMO Rep. 37*, 1995.

Yaglom, A. M., and I. M. Yaglom, *Probability and information*, Reidel, Dordrecht, 1983.

Young, A. T., Revised depolarization corrections for atmospheric extinction, *Appl. Opt.*, *19*, 3427-3438, 1980.

Yung, Y. L., J. P. Pinto, R. T. Watson, and S. P. Sander, Atmospheric bromine and ozone perturbations in the lower stratosphere, *J. Atmos. Sci.*, *37*, 339-353, 1980.

Acknowledgments

Now I would like to thank all my colleagues who made the carrying out of my investigation possible and collaborated with me.

- I thank *Prof. Dr. John P. Burrows* for entrusting me with one of the most significant and complicated problems which is not only of great importance for recent scientific projects dealing with global observations of the Earth's atmosphere but is also very interesting for me as a scientist.

- *Dr. Vladimir Rozanov* contributed significantly to the development of the theoretical basis of the method to solve the radiative transfer equation in a spherical planetary atmosphere as well as provided the GOMETRAN radiative transfer model which was employed as a part of the newly developed CDIPI radiative transfer model. Furthermore, I thank Dr. Vladimir Rozanov for helpful comments on this thesis as well as for help in solving the problems which arose during my research work.

- At the beginning of my work in the SCIAMACHY algorithm group, *Michael Buchwitz* acquainted me with the existing software and helped me to begin my own research activity.

- The newly developed radiative transfer model was successfully optimized and validated due to the collaboration of *Johannes Kaiser*, *Liisa Oikarinen* (Finnish Meteorological Institute, Helsinki, Finland), *Dave Flittner* (Institute of Atmospheric Physics, University of Arizona, USA), and *Jürgen Steinacker* (MPG Research Unit "Dust in Star–Forming Regions", Jena, Germany).

- The teamwork together with *Richard Müller* and *Folkard Wittrock* enabled the developed radiative transfer models to be applied to some adjacent scientific problems.

- *Günther Lehnert* helped me very much to optimize and to parallelize the program code.

- I thank also all my colleagues who have read this thesis, commented on its content as well as corrected typing errors.

List of publications

Peer-reviewed papers:

- Grigoriev, I. M., N. N. Filippov, A. V. Rozanov, and M. V. Tonkov, Line Shapes in the Rotational Spectra of HF, and Ar Gas: New Experimental Data and Calculations of Line Interference, *J. Quant. Spectrosc. Radiat. Transfer*, *55(1)*, 61–71, 1996.

- Rozanov, A., V. Rozanov, and J. P. Burrows, Combined differential-integral approach for the radiation field computation in a spherical shell atmosphere: Non-limb geometry, *J. Geophys. Res.*, 2000, *105*, 22937-22943, 2000.

- Rozanov, A., V. Rozanov, and J. P. Burrows, A numerical radiative transfer model for a spherical planetary atmosphere: Combined differential–integral approach involving the Picard iterative approximation, *J. Quant. Spectrosc. Radiat. Transfer*, *69*, 491-512, 2001.

Conference proceedings:

- Grigoriev, I. M., N. N. Filippov, A. V. Rozanov, and M. V. Tonkov, Experimental HF–Ar lineshape parameters in far infrared: broadening, shifts, and line mixing, *Proc. 12th International Conference on Spectral Line Shapes*, 12–17 June, Toronto, Canada, 1994.

- Rozanov, A. V., A. V. Poberovsky, Twilight measurements of stratospheric NO_2 near St. Petersburg, *Proc. Conference on Atmospheric Ozone*, 24–25 April, IFA RAN, Moscow, Russia, 1996.

- Rozanov, A., V. Rozanov, M. Buchwitz, and J. P. Burrows, SCIAMACHY occultation mode: forward model and retrieval algorithm, *Proc. Seventh GOME and SCIAMACHY Data and Algorithm Scientific Working Sessions*, 6-7 Apr, ESRIN, Frascati, Italy, 1998.

- Rozanov, A., V. Rozanov, M. Buchwitz, and J. P. Burrows, A radiative transfer model for SCIAMACHY limb measurements, *Proc. European Symposium on Atmospheric Measurements from Space*, 18-22 January, ESTEC, Noorwijk, The Netherlands, 89-99, 1999.

- Rozanov, A., V. Rozanov, F. Wittrock, and J. P. Burrows, A new radiative transfer model for DOAS interpretation of off-axis measurements, *Proc. Fifth European Workshop on Stratospheric Ozone*, 27 Sep – 1 Oct, St Jean de Luz, France, 1999.

- Rozanov, A., V. Rozanov, J. P. Burrows, Evaluation of the Combined Differential-Integral approach for limb viewing geometry, to appear in *Advances in Space Research*, 2001.

- Müller, R. W., H. Bovensmann, M. Bruns, J. Kaiser, A. Richter, A. Rozanov, F. Wittrock, and J. P. Burrows, Consistent interpretation of ground based and GOME BrO SCD data, to appear in *Advances in Space Research*, 2001.

- Kaiser, J., A. Rozanov, V. Rozanov, and J. P. Burrows, Evaluation of approximative radiative transfer models intended for retrievals from limb measurements, to appear in IRS200: Current Problems in Atmospheric Radiation, edited by W. L. Smith and Y. M. Timofeyev, A. Deepak Publishing, Hampton, Virginia, 2001.

- Postylyakov, O., Yu. E. Belikov, Sh. S. Nikolaishvili, and A. Rozanov, A comparison of radiation transfer algorithms for modeling of the zenith sky radiance observations used for determination of stratospheric trace gases and aerosol, to appear in IRS200: Current Problems in Atmospheric Radiation, edited by W. L. Smith and Y. M. Timofeyev, A. Deepak Publishing, Hampton, Virginia, 2001.

Unpublished conference contributions:

- Rozanov, A., V. Rozanov, R. Müller, and J. P. Burrows, NO_2 air mass factors considering photochemistry, *EGS 2000: 25-th General Assembly*, 26 – 30 April, Nice, France, 2000.

- Rozanov, A., V. Rozanov, J. P. Burrows, A new radiative transfer model for a spherical planetary atmosphere, *International Radiation Symposium*, 24 – 30 July, St. Petersburg, Russia, 2000.

- Rozanov, A., V. Rozanov, and J. P. Burrows, Accuracy of the limb radiance modeling in near-IR spectral range employing a correlated-k distribution scheme, *EGS 2001: 26-th General Assembly*, 25 – 30 March, Nice, France, 2001.

- Emde, C., J. Meyer, A. Rozanov, V. Rozanov, and J. P. Burrows, Influences of horizontal atmospheric inhomogeneities on radiative transfer modeling, *EGS 2001: 26-th General Assembly*, 25 – 30 March, Nice, France, 2001.

- Kostadinov, I., G. Giovanelli, F. Ravegnani, A. Petritoli, D. Bortoli, D. Kylling, V. Rozanov, B. Mayer, A. Rozanov, A. Ulanovsky, V. Yushkov, Aircraft UV/Vis radiation measurements during APE-GAIA campaign in Antarctica, *EGS 2001: 26-th General Assembly*, 25 – 30 March, Nice, France, 2001.